University of Bath

PHD

Low Conductivity Magnetic Induction Tomography for Landmine Detection

Li, Fang

Award date:
2018

Awarding institution:
University of Bath

Link to publication

Alternative formats
If you require this document in an alternative format, please contact:
openaccess@bath.ac.uk

Copyright of this thesis rests with the author. Access is subject to the above licence, if given. If no licence is specified above, original content in this thesis is licensed under the terms of the Creative Commons Attribution-NonCommercial 4.0 International (CC BY-NC-ND 4.0) Licence (https://creativecommons.org/licenses/by-nc-nd/4.0/). Any third-party copyright material present remains the property of its respective owner(s) and is licensed under its existing terms.

Take down policy
If you consider content within Bath's Research Portal to be in breach of UK law, please contact: openaccess@bath.ac.uk with the details. Your claim will be investigated and, where appropriate, the item will be removed from public view as soon as possible.

Download date: 05. May. 2023

Low Conductivity Magnetic Induction Tomography for Landmine Detection

By

Fang Li

BEng, MSc

A dissertation submitted to

Department of Electronic and Electrical Engineering

University of Bath

In fulfilment of the requirements for the degree of

Doctor of Philosophy

COPYRIGHT

Attention is drawn to the fact that copyright of this thesis/portfolio tests with the author and copyright of any previously published material included may rest with third parties. A copy of this thesis has been supplied on condition that anyone who consults it understands that they must not copy it or used material from it except as permitted by law or with the consent of the author or other copyright owners, as applicable.

This thesis may be made available for consultation within the University Library and may be photocopied or lent to other libraries for the purpose of consultation.

Bath, Feb 2018

DECLARATION

I declare that I have read and understood the entry in the Student Handbook for the Department of Electronic and Electrical Engineering on Cheating and Plagiarism and that all material in this thesis is my own work, except where I have indicated with appropriate references. It is being submitted for in fulfillment of the requirements of the degree of Doctor of Philosophy in Electronic and Electrical Engineering. No portion of the work in this document has been submitted before for any degree or examination at any other university.

Signature of Author .....

Date .....

Department of Electronic and Electrical Engineering, University of Bath

ABSTRACT

The main objective of the dissertation is to improve the imaging results for magnetic inductance tomography (MIT) as a non-destructive imaging technique. MIT is generally used to display the imaging contains the conductivity properties of the object under test. The hardware and software are regarded as basic topics of the development of MIT. The hardware of MIT is briefly introduced but analyzing the software problem of MIT is the main purpose of this thesis.

The working flow of this dissertation can be explained as the following sections. Firstly, the forward problem of MIT has been studied theoretically, including eddy current modeling with Biot-Savart theory implemented and the simulation works for the validation of forward problem. Secondly, the algorithms of inverse problem solvers are presented based on the explanation of mathematical equations, including linear/non-linear or iterative/non-iterative inverse problem. Thirdly, improved image quality of reconstructed images obtained by total variation regularization as the inverse problem solver both in circular and planar array sensor MIT system are demonstrated by experimental results. Finally, the potential feasibility of planar MIT system assisting other imaging system such as electrical capacitance tomography for plastic landmine detection is illustrated by simulation works.

Altogether, this thesis presents the author's research interests on improving reconstruction performance of MIT trough analyzing on inverse problem algorithms developments and expand the potential application of planar low conductivity MIT system in plastic Landmine detection.

I DEDICATED THIS THESIS TO MY LOVELY FAMILY

ACKNOWLEDGMENTS

This research study was carried out in the Department of Electronic and Electrical Engineering at the University of Bath, United Kingdom, from 2014-2017. My sincere thanks to all the people who give me their support, as this dissertation would not have been possible without their contributions.

Firstly, I would first like to express my deep grateful to my supervisor, Prof. Manuchehr Soleimani, for his guidance and support in many ways throughout the research. As a professional and respected scientist in electrical tomography communities, he provided many valuable suggestions and ideas with his knowledge during my research and also guided me into the right direction with his experience. Also, he is an amature, considerable and patient person who contributed a significant amount of time to support me whenever I needed. I consider myself very fortunate to have an academic journey with an amazing researcher and encouraging supervisor like him.

Secondly, I owe many thanks to Find a Better Way and University of Bath, who provided financial support for my research. Also, I would like to thank the University for offering me this opportunity to study in the United Kingdom.

I also wish to express my thanks to my fellow colleagues who spent their time with me using their professional knowledge and valuable experiences when I encountered problems. It was a great fortunate to be part of this Tomography Laboratory Team.

Finally, I am sincerely grateful to my lovely parents: Yingxi Li, Maiping Fang and my dear brother Tengfei Li, sister Qing Guo, for their spiritual encouragements and support during this period. Also, I express deep gratitude towards my lovely friend, Nan Lan, who provided infinite encouragements during my whole PhD study.

LIST OF PUBLICATIONS

Journal Papers

- Li, F., Abascal, J., M, D. and Soleimani, M., 2017. Total variation regularization with Split Bregman based method in magnetic induction tomography using experimental data. *IEEE Sensor Journal*, 17(4), 976-985.

- Planar array magnetic induction tomography further improvement. *Sensor Review* (Accepted)
- MIT for landmine detection: simulation study. Submitted

Conference or Workshop Items

- Li, F. and Soleimani, M., 2016. Comparison of TV and Tikhonov regularization in MIT for low and high conductivity imaging. *In: World congress in industrial process tomography (WCIPT8),* 2016-09-26, Brazil

TABLE OF CONTENTS

LIST OF FIGURES

LIST OF TABLES

LIST OF SYMBOLS

A — Magnetic potential ($V \cdot S \cdot m^{-1}$)

B — Magnetic flux density (T)

E — Electric field (Vm^{-1})

H — Magnetic field intensity (Am^{-1})

V— Electrical potential (V)

μ — Magnetic permeability (Hm^{-1})

ε — Electrical permittivity (Fm^{-1})

σ — Electrical conductivity (Sm^{-1})

ω — Angular frequency (rad/s)

NOMENCLATURE

MIT — Magnetic inductance tomography

ECT — Electrical capacitance tomography

EIT — Electrical impedance tomography

NDT — Non-destructive test

LBP — Linear back-projection

SVD— Singular value decomposition

TSVD — Truncated singular value decomposition

MAP — Maximum A-Posterior estimate

ROI — Region of Interest

UI — Ultrasonic Inspection Data Acquisition

TV — Total variation

SD — Shape deformation

RES — Resolution

AR — Amplitude ration

CHAPTER 1 INTRODUCTION

Tomography, which can be divided into 'hard field tomography' and 'soft field tomography' [1], is a technique that can display an image of the physical properties of an object. The 'hard field tomography' is widely used in medical field such as $X-ray$ and $\gamma-ray$ tomography. The 'soft field tomography', mainly including magnetic inductance tomography (MIT), electrical capacitance tomography (ECT) and electrical impedance tomography (EIT), is a much more complex technique than that in hard field but normally used in industrial imaging and medical imaging [2]. In addition, these three techniques are generally named electrical tomography, which are introduced as following.

1.1 Electromagnetic Tomography

Electrical tomography, including magnetic inductance tomography, electrical capacitance tomography and electrical impedance tomography, is normally used to display the images contains the passive electromagnetic properties (PEP) of the object [3].

ECT is another non-invasive technology [1], which produces tomograms of permittivity distributions by using capacitance measurements. The information about the distribution of the contents of closed pipes or vessels can be obtained by measuring capacitance between pairs of electrodes at the boundary around the samples. The reconstruction domain is normally a disc with the peripheral electrodes, besides that, some domains have also been discussed such as cubes, cylinders and squares. Since ECT aims at visualizing the unknown permittivity of electrodes at the boundary around the samples with the distribution of dielectric materials, it is widely used to image dielectric permittivity of insulating objects.

EIT, the oldest electrical imaging technique, is very similar to ECT, since it also applies an

electric field to the material as well as uses an array of electrodes. The only difference of those two techniques is in measurement methods. In ECT, capacitance is computed between different pairs of electrodes instead of measuring the trans impedance including four electrodes at the same time. While in EIT, the injected current and electric potential, which can be computed by the electrodes, produce a set of four-electrode trans impedance and the permittivity and electrical conductivity can be measured from a cross section of that four-electrode [4, 5].

MIT and ECT are both non-invasive techniques, which means they will be widely used in biomedical and industrial [6]. At the meantime, they also have their own characteristics and functions. MIT is not sensitive to permittivity but sensitive to electrical conductivity σ and used to image electrical conductivity of the target been test. ECT is sensitive to permittivity ε so that it is commonly used to visualize the dielectric distribution of objects. Moreover, although MIT and EIT are both sensitive to conductivity σ, MIT is different from EIT since MIT doesn't require galvanic coupling between the device and the object.

Initially, metallic based MIT was developed for molten metal flow monitoring [7]. In the past few years, low conductivity MIT has been primarily developed for medical imaging applications such as imaging brain function or stroke detection [8], and has lately being proposed as potential multi-phase flow imaging technique. High conductivity MIT has also been widely used in industrial applications such as non-destructive testing (NDT) for material characterization [9], [70]. In recent years, MIT was developed for both medical and industrial applications such as stroke detection [8], molten metal flow monitoring [10], and as a potential detection tool for National Nuclear Security[11].

1.2 Landmine detection

Landmines, designed for protecting the countries and people, turns out to be the most terrifying marks left behind the world wars. There is a huge number of landmines buried under ground around the world, which can trigger 15,000 to 20,000 casualties every year and most of the

damage is unrecoverable[12]. Therefore, locating and clearing away the landmines are tricky problems we are facing nowadays. Even plenty of contributions on landmines detection have been conducted by the world effort, all the existing technologies have its limitations on types of landmines and soils. And there is no one technique that can work efficiently alone for all the cases. Planar low conductivity MIT assists ECT for plastic landmine detection is introduced in this thesis by simulation works.

1.3 Aims and objectives

The main overall objective of this PhD research is focusing on improving reconstruction performance of MIT by analyzing on algorithm developments. MIT has been regarded as a non-destructive technique for visualizing the conductive distribution of the target. As such it has been considered as a potential method for the inspection of conductive material both in medical and industrial tomography area, however, MIT remains challenging in real-life applications because of its low-resolution nature. To overcome this limit, efforts should be made into both forward model and inverse algorithm developments. Besides, enhanced software should be adopted into a variety of MIT sensors geometries for intended specific applications to analyze the flexibility of MIT system. Moreover, although MIT is a newer technique, several potential applications for MIT are suggested. Specific focus of application of MIT will be on planar array low MIT system as a potential candidate for plastic landmine detection. In general, the aims and objectives of this thesis can be categorized in four aspects:

- Clarifying the working principles and procedure of low conductivity & high conductivity MIT system
- Establishing and modifying the forward models to improve the resolution
- Analyzing the inverse problem algorithms to improve the resolution
- Adopting the enhanced algorithms to different MIT sensors geometries to obtain better

quality reconstruction images

- Investigating and evaluating the feasibility and capability of planar array sensor low conductivity MIT for plastic landmine detection

1.4 Structure of the dissertation

The chapters of this thesis are organized as below.

Chapter2 briefly introduces the MIT system through principles, applications and demonstrates the existing MIT systems. The basic principles of MIT are explained by the mutual inductance and eddy current theories. The applications of MIT introduced are industry and biomedical applications. The MIT hardware discussed are low conductivity MIT system (Mk-III) and high conductivity MIT system (Mk-II).

Chapter3 clarifies the all the basic theories that are required to solve the forward problem in MIT. Maxwell's equation is presented at first and then edge finite element method is introduced following. The most key content is Biot-Savart theory, which is treated as a potential method for solving the eddy current problem of MIT, is presented in detail. Besides, the simulation model used both in circular sensor array and planar sensor array are also been presented. Moreover, the validation works on forward problem model are also demonstrated.

Chapter4 analyzes several algorithms that can be used to solve the inverse problem in MIT. The algorithms are divided into linear and non-linear inverse problem. Linear inverse problem, which includes Non-iterative method (Tikhonov regularization) and iterative method (Total Variation regularization). Total variation regularization method, the main topic of this chapter, has been introduced through isotropic total variation and anisotropic total variation.

Chapter5 investigates the total variation regularization method adopted to circular sensor array MIT with the aid of experimental data and quantitative analysis. This chapter presents for the

first time split Bregman total variation (TV) regularization to solve the MIT inverse problem. Comparative evaluations are presented between proposed TV algorithm and more commonly used Tikhonov regularization method. Experimental results are quantified by a number of image quality measurements, which show the superiority of the proposed TV method both on low conductivity and high conductivity MIT data. Significant improvement in MIT imaging results makes the proposed TV method a great candidate for both types of MIT imaging.

Chapter6 investigates the total variation regularization method for planar sensor array MIT with the aid of experimental data and quantitative analysis. By compared with the Tikhonov regularization results, it shows that Tikhonov method failed or underestimated the object position and depth. Total variation led to accurate recovery of depth and position. Therefore, there are numerous potential applications for planar array MIT where access to the materials under testing is restrict. Sparse regularization methods are a promising approach to improving depth detection for limited MIT data.

Chapter7 evaluates the feasibility and capability of planar sensor array low conductivity MIT system for plastic Landmine detection through simulation study of MIT system only. MIT itself is incapable of detecting the plastic landmines because of the low conductivity contrast while ECT can work efficiently for detecting the plastic landmines buried in non-conductive or negligibly low conductivity ground. But in the case of the plastic landmines were planted in ground whose conductivity is non-negligible, ECT requires the assistance provided by planar MIT. All the simulation results presented in this chapter indicates the feasibility of MIT system for landmine detection. Demonstrating classification experimental study could further validate this research observation.

Chapter8 summarizes the conclusion based on the novel findings obtained in this dissertation. The limitations and challenges associated to this current works are also discussed. Finally, the potential and prospective future works are suggested in this chapter.

CHAPTER 2 MIT HARDWARE AND SENSOR DESIGN

2.1 Magnetic Induction Tomography

MIT, which has been variously named electromagnetic tomography (EMT) and mutual inductance tomography (MIT) [4], is the least developed technique that has been improved for the process industry and medical imaging. The MIT coils can be divided into excitation coils and receiver coils [13]. When injecting an alternating current to the excitation coil, a primary magnetic field can be generated, which induces an eddy current in the target object. Then the measuring coils can detect the secondary magnetic field. Additionally, MIT is actually focus on conductivity, although it is sensitive to all three electromagnetic properties that are permeability (μ), permittivity (ε) and conductivity (σ) [5]. Since that, MIT is aiming at visualizing the conductive distribution of the object under test.

2.2 Basic Principles of MIT

Magnetic induction tomography, used to image the passive electromagnetic properties (PEP) [14] of an object, can be explained by the mutual inductance and eddy current theories . The coils used in MIT can be divided into excitation coils and measuring coils. The fundamental principles can be seen from Figure 2.1, when injecting an alternating current to the excitation coil, a primary magnetic field can be generated, which will induce electrical field that can be detected by the measuring coils. In the case of having a conductive object placed between excitation and measuring coils, an eddy current will be induced and that will generate a secondary magnetic field, which can also be detected by the measuring coil. Since the voltage measurements on the detected coils is the sum of the primary and secondary field, the difference of these two measurements can be used to analyze the properties of the object [3].

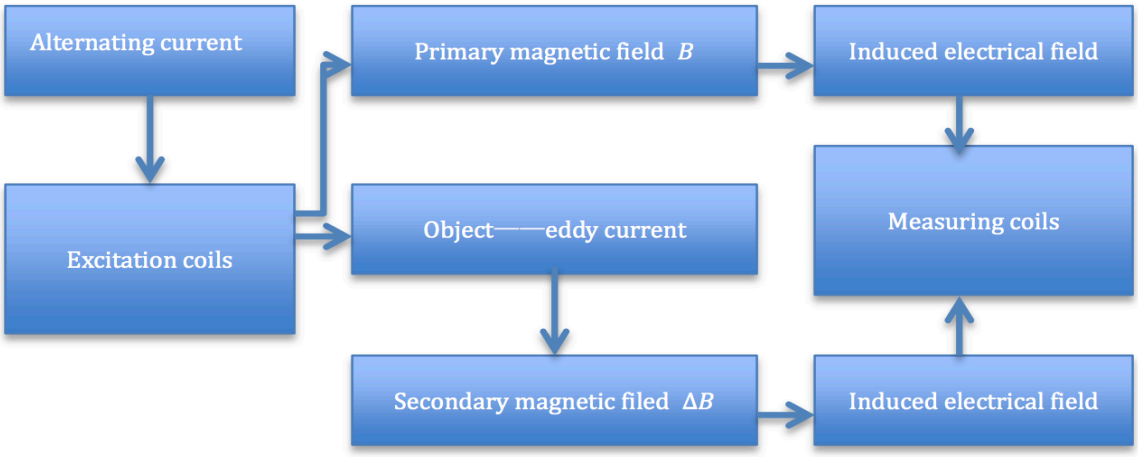

Figure 2.1 Fundamental principles of MIT

Through the study of mutual inductance theory and eddy current theory and driving the equation between the induced voltage and the primary voltage, it can be proved that one can obtain the properties of object by analyzing the differences of two measuring voltage.

The equivalent circuit diagram, shown in Figure 2.2, can be used to simplify the mutual inductance theory and eddy current theory [14]. The excitation coil can be treated to an AC current source applied to an inductor and the measuring coil is an inductor as well with the measurement voltage (V_2), the value of the inductances is L_1 and L_2. A basic R-C circuit can be used to simplify the properties of object and it will work like a voltage source (V_3) with an inductance (L_3). M_{12}, M_{13} and M_{23} are the mutual inductance between three inductors.

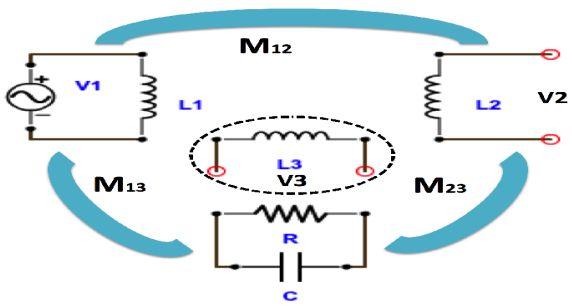

Figure 2.2 Equivalent circuit of mutual inductance theory [9]

From the magnetic flux equations, it can be obtained as following. $\widehat{I_3}$ is the eddy current due to the alternating current injected to excitation coils and $\widehat{U_3}$ is the induced voltage induced by eddy current.

$$\widehat{U_2} = -M_{12}\widehat{I_1} - M_{23}\widehat{I_3} \tag{2.1}$$

$$\widehat{U_3} = -M_{13}\widehat{I_1} \tag{2.2}$$

$$\widehat{I_3} = \widehat{U_3}/Z_3 \tag{2.3}$$

$$Z_3 = R \parallel \frac{1}{j\omega C} = R/(1 + j\omega RC) \tag{2.4}$$

Where Z_3 is the impedance of the specimen in $ohms$, R is the resistance of the specimen in $ohms$, C is the capacitance of the specimen in $farads$ and $\omega = 2\pi f$, f is the frequency in hz and ω is the angular frequency in rad/s.

Then put equation 2.2-2.4 to equation 2.1, it can be obtained:

$$\widehat{U_2} = [-M_{12} + M_{13}M_{23}\left(\frac{1}{R} + j\omega C\right)]\widehat{I_1} \tag{2.5}$$

$$\widehat{I_1} = \widehat{U_1}/j\omega L_1 \tag{2.6}$$

Then it can be obtained that since the value of M_{12}, M_{13}, M_{23}, $\widehat{U_1}$ and L_1 is constant:

$$\widehat{U_2} \propto \frac{1}{R} + j\omega C \tag{2.7}$$

As it is well known that resistance and capacitance can be defined as following:

$$R = l/A\,\sigma,\ C = \mathcal{E}_0\mathcal{E}_r\,A/d \tag{2.8}$$

Where σ is the conductivity of the object, $\mathcal{E}_0\mathcal{E}_r$ are the permittivity of the object, l is the length of the material, A is the cross-sectional area and d is the distance between the plates. For a given specimen, l/A and A/d can be considered constant, therefore, equation 2.9 can be obtained:

$$\widehat{U_2} \propto \sigma + j\omega\mathcal{E}_0\mathcal{E}_r \tag{2.9}$$

The following conclusions can be obtained obviously from equation 2.9:

- The properties of the object can be obtained by analyzing the induced voltage on measuring coils
- For the highly conductive samples, mainly for in industry applications, the imaginary part of induced voltage can be neglected, and the induced voltage can be considered proportional to the amplitude of the conductivity of samples
- For the lower conductivity samples, mainly for biomedical applications, the induced voltage is the combination of both amplitudes and the phase shift.

When we consider this equivalent circuit to a simplified two-channel system, the following equations can be obtained.

Assuming that the alternating current is induced by a sinusoidal voltage $v_1(t) = \cos(\omega t) = \frac{e^{-j\omega t}+e^{j\omega t}}{2}$. Then the alternating current is:

$$i_1 = v_1/j\omega L_1 = \frac{e^{-j\omega t}+e^{j\omega t}}{j\omega L_1} \tag{2.10}$$

In the case of no object in the measuring space, the primary induced voltage at the receiving coil is:

$$v_2 = -M_{12}\frac{\partial i_1}{\partial t} = -M_{12}\frac{e^{j\omega t}-e^{-j\omega t}}{L_1} \tag{2.11}$$

Then assuming an object has the impedance of Z been placed between excitation and receiving coils, the induced voltage produced by the alternating current and the eddy current can be obtained:

$$v_{eddy} = -M_{13}\frac{\partial i_1}{\partial t} = -M_{13}\frac{e^{j\omega t}-e^{-j\omega t}}{2L_1} \tag{2.12}$$

$$i_{eddy} = \frac{v_{eddy}}{Z} \tag{2.13}$$

$$Z = R + jX \tag{2.14}$$

Where R is the resistance of the specimen, X is the reactance of the specimen, i.e., for a capacitor, the capacitor reactance $X_C = \frac{1}{\omega C}$, Z is the impedance of the specimen in complex form.

Finally, the new total voltage detected in the receiving coils is:

$$v_2 = -M_{12}\frac{\partial i_1}{\partial t} - M_{23}\frac{\partial i_{eddy}}{\partial t} = -M_{12}\frac{v_1}{L_1} + jM_{13}M_{23}\frac{\omega v_1}{L_1(R+jX)} \tag{2.15}$$

The following conclusions can be obtained obviously from equation 2.15:

- The voltage detected by the receiving coil consist of the primary induced voltage (real part) $M_{12}\frac{v_1}{L_1}$ and the perturbation signal (imaginary part) $M_{13}M_{23}\frac{\omega v_1}{L_1(R+jX)}$.
- For the highly conductive samples ($R \ll X$), mainly for in industry application, equation 2.15 can be simplified to: $v_2 = -M_{12}\frac{v_1}{L_1} + M_{13}M_{23}\frac{\omega v_1}{L_1 X}$, which means there is no imaginary part and amplitude change is the main measurement.
- For the lower conductivity samples ($R \gg X$), mainly for biomedical applications, equation 2.15 can be simplified to: $v_2 = -M_{12}\frac{v_1}{L_1} + jM_{13}M_{23}\frac{\omega v_1}{L_1 R}$, which means the induced voltage is the combination of both amplitudes and the phase shift.

Some conclusions can be obtained from the above discussion as following. The basic principle of magnetic induction tomography can be explained based on mutual inductance and eddy current problem. The equations 2.9 and equation 2.15, which are obtained from the equivalent mutual inductance and eddy current problem circuit, proved that the properties of the object can be obtained by analyzing the induced voltage on measuring coils. Moreover, the amplitude change is the main measurement for highly conductive samples while both amplitudes and the

phase shift can be detected for low conductivity samples. Since that the already developed high conductivity MIT system (mainly used in industry area) and the low conductivity MIT system (designed for biomedical applications) are also presented in this chapter

2.3 MIT Hardware Overview

The typical structure of MIT system is shown in Figure 2.3 [15], which indicates a general MIT system normally consist of the measuring part, conditioning electronics part, data acquainting & processing part as well as the computer that used to produce the images. Though there are some different types of MIT system, the characteristics of their components are nearly the same in some degree.

The measuring part includes an array of coils placed around the measuring space [16]. And the different size, number and position of the coils can form variable types of MIT while the conditioning electronics are normally consisting of amplification circuit, precision rectifier and low pass filtering.

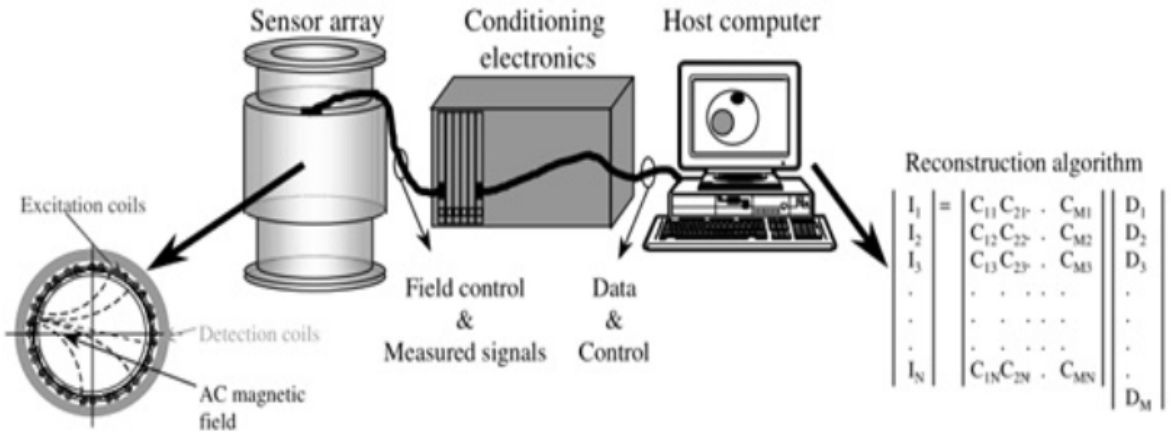

Figure 2.3 Block diagram of a MIT system [17]

During the experiment process, two sets of measurement should be acquired, which are background data (B) and the measuring data ($B + \Delta B$). Background data, considered as a

reference data, is usually obtained in the case of no object in the measuring space. And then the measuring data is usually taken with the target is placed within the measuring space. After recording these two sets of data, the difference between them then can produce the information of the perturbation signal (ΔB).

In this chapter, two types of MIT system are introduced as following.

2.3.1 High conductivity MIT system

High conductivity MIT system can be divided into circular sensor array and planar sensor array MIT system[18, 19], shown in in Figure 2.4 and Figure 2.5 respectively. The system designed for high conductivity sample imaging discussed in this section consists of [20]: (i) Signal generator; (ii) A National Instrument based data acquisition system (NI USB-6259); (iii) Chanel switching board; (iv) The sensor array contains several inductive coils (excitation coils and receiver coils), which are equally arranged around the periphery of the measurement space. The design of the coil array is decided by the intended applications; (v)A host computer.

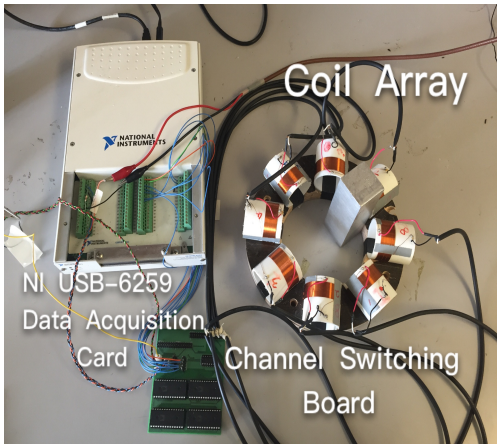

Figure 2.4 Circular sensor array MIT

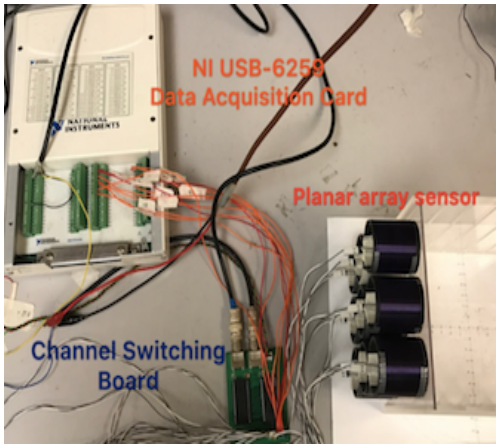

Figure 2.5 Planar sensor array MIT

For a MIT system with n number of coils, the unique coil pairs are: 1-2,1-3,1-n…2-3,2-$(n-1)$…$(n-1)$-n. The data collection pattern can be described as [14]: exciting coil 1 as the excitation coils forms the first cycle, the voltage measurement will be obtained from the other receiver coils (2 to $n-1$); exciting coil 2 as the second cycle, and then the

voltage measurement can be read from coil 3 to coil $n-1$…etc, therefore, it can provide $m = n\,(n-1)/2$ independent measurements, which can be imported to the image reconstruction system to perform the reconstruction images. In the case of 8-channel system, there is $\frac{8\times7}{2} = 28$ measurements.

2.3.2 Low conductivity MIT system

The MIT system, which is designed for low conductivity sample imaging, discussed in this section is the Bath MK-III system, consists of [1, 20]: (i) Signal generator; (ii) A National Instrument based data acquisition system (NI PXle-1073); (iii) The sensor array contains 16 air-core inductive coils are equally spaced around the measurement space. A grounded aluminum cylinder is used to prevent the outer perturbation. The 16 coils, which are shown in Figure 2.7, consist eight transmitter coils (ch8-15) and the other eight receiver coils (ch0-7); (iv) A host computer; as shown in Figure 2.6

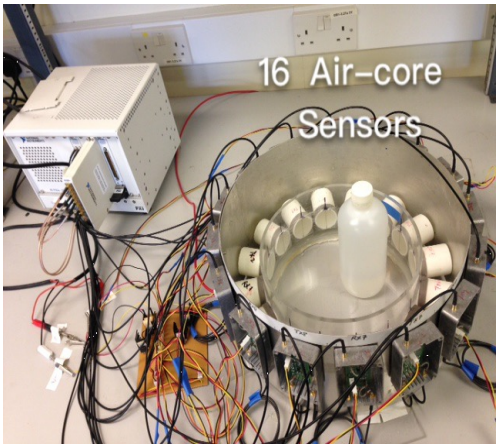

Figure 2.6 Bath MK-III magnetic induction tomography system

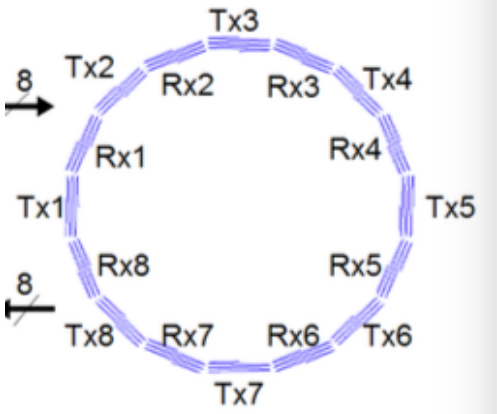

Figure 2.7 The structure of 16-air-core-coils [1]

The working frequency of this system is selected to be 13MHz and the LabView program is used in this system to control the signal generator and achieve the data acquisition/ channel switching tasks [21]. The data collection pattern of this system is as following: Tx1-Rx2, Tx1-Rx3, …Tx1-Rx7, Tx2-Rx3, Tx2-Rx4, …Tx2-Rx8, …and Tx8-Rx6, which can provide $8 \times (8-2) = 48$ measurements. And then the image reconstruction system extracts those independent measurements to LabView and Matlab program to display the updated reconstruction images.

2.4 Application of MIT

The applications of MIT can be divided into two application areas as following:

- Industry applications: two-phase flow process imaging in pipelines; Non-destructive testing (NDT) for material characterization; tracking ferrite labeled powder in the separation processes [8]; as a potential detection tool for National Nuclear Security[11].
- Biomedical applications: lung imaging; brain images for stroke detection [22] [9].

CHAPTER 3 FORWARD PROBLEM

Magnetic induction tomography, aiming at visualizing the conductive distribution of the object under test, is the least developed technique that has been improved for the process industry and medical imaging. The forward problem of MIT is solving the estimated measurement values on detected coils with a set of given passive electromagnetic properties distributions as well as excitation current [23]. It can be explained by solving the eddy current problem, which is actually using Maxwell's equations. Besides, the main method used in MIT forward problems nowadays is analyzing eddy current problem with the aid of the finite element method (FEM). Solving this problem requires modelling a system that is based on the actual system parameters, which means the meshing the coil structures into the model is necessary. But the mesh structure has to be changed every time when the sensor array is changed. Biot-Savart theory are introduced to overcome this inflexibility of MIT. By adopting this method, coils structures not required to be meshed into the model. In this section, Biot-Savart theory, Maxwell's equations, finite element method, edge FEM and are introduced step by step.

3.1 Biot-Savart theory

3.1.1 Definition

In theory, the Biot-savart law [24] indicates that the magnetic field $\overrightarrow{dB}$ at any point due to $\overrightarrow{dl}$ is:

$$\overrightarrow{dB} = \frac{\mu_0 I}{4\pi|r|^3}\overrightarrow{dl} \times \vec{r} \tag{3.1}$$

Where r is the distance between the current segment dl and the fixed point, μ_0 represents the free space permeability.

The first step of applying Biot-Savart law into this model is generating the mesh model by NetGen program [14] and treat every coil consists of several small current segments.

And then the magnetic flux density of any fixed point in the mesh model due to one source current segment can be calculated as following [25].

Assuming point A (x_1, y_1, z_1) and B (x_2, y_2, z_2) forms a current segment. Then the current segment vector can be calculated:

$$\overrightarrow{dl} = (x_2 - x_1)\vec{i} + (y_2 - y_1)\vec{j} + (z_2 - z_1)\vec{k} \tag{3.2}$$

Assuming the fixed point is P (x_3, y_3, z_3), the distance value and distance vector can be obtained after calculating the midpoint of current segment O $(\frac{x_1+x_2}{2}, \frac{y_1+y_2}{2}, \frac{z_1+z_2}{2})$:

$$\vec{r} = \left(x_3 - \tfrac{x_1+x_2}{2}\right)\vec{i} + \left(y_3 - \tfrac{y_1+y_2}{2}\right)\vec{j} + \left(z_3 - \tfrac{z_1+z_2}{2}\right)\vec{k} \tag{3.3}$$

$$|r| = \sqrt{\left((x_3 - \tfrac{x_1+x_2}{2})^2\right) + \left((y_3 - \tfrac{y_1+y_2}{2})^2\right) + ((z_3 - \tfrac{z_1+z_2}{2})^2)} \tag{3.4}$$

The cross product of $\overrightarrow{dl}$ and $\vec{r}$ is:

$$\begin{aligned}\overrightarrow{dl} \times \vec{r} = &((y_2 - y_1)\left(z_3 - \frac{z_1 + z_2}{2}\right) - (z_2 - z_1)\left(y_3 - \frac{y_1 + y_2}{2}\right))\vec{i} \\ &+ \left((z_2 - z_1)\left(x_3 - \tfrac{x_1+x_2}{2}\right) - (x_2 - x_1)\left(z_3 - \tfrac{z_1+z_2}{2}\right)\right)\vec{j} \\ &+ \left((x_2 - x_1)\left(y_3 - \tfrac{y_1+y_2}{2}\right) - (y_2 - y_1)\left(x_3 - \tfrac{x_1+x_2}{2}\right)\right)\vec{k}\end{aligned} \tag{3.5}$$

Then the magnetic flux density $\overrightarrow{dB}$ of a fixed point in the mesh model due to any source current segment can be obtained by putting equation 3.3-3.5 into equation 3.1.

After that, the magnetic flux density of a fixed-point due to one coil can be obtained by superposition all the small current segments. And the magnetic flux density due to another coil

can be simply calculated by rotation that fixed coil with a rotation angle, for example: the rotation angle of 8-coils system is $\frac{2\pi}{8}$.

Finally, the total magnetic flux density B_s of a fixed-point due to the whole MIT system can be obtained by adding them up and then:

$$B_s = \int \frac{\mu_0 I}{4\pi |r|^3} \overrightarrow{dl} \times \vec{r} \tag{3.6}$$

And then the two-potentials method (primary magnetic vector potential and reduced magnetic vector potential) using the Biot-Savart Theory will be introduced later on in Chapter 3.2

The following section will introduce the simulation model of Biot-Savart law used in eddy current problem to calculate B field both in circular and planar MIT system. Figure 3.1 shows the simulation process. Then the Biot-Savart simulation model for circular and planar MIT system is discussed in detail separately. It has been mentioned that the difference between those two models is whether rotating coils or shifting coils, which is introduced in Chapter 3.1.2 and Chapter 3.1.3.

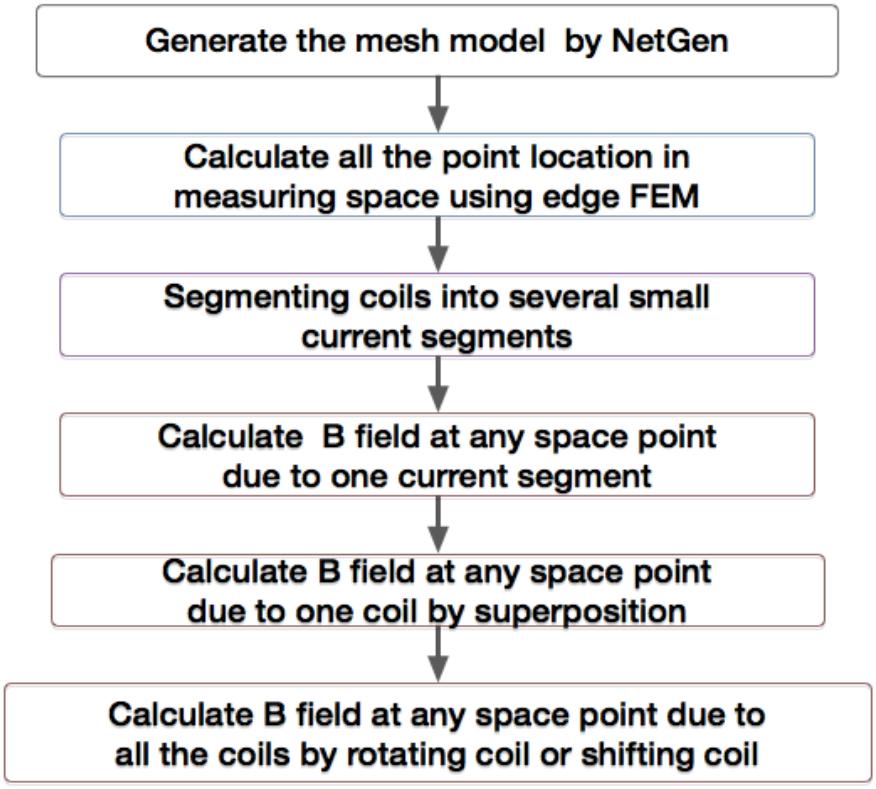

Figure 3.1 The process of using Biot-Savart law to calculate B field

3.1.2 Simulation model (Software) of circular MIT system

The circular system discussed in this thesis is an already developed 8-coils MIT system. Figure 3.2 indicates the top view of the 8-circular coil array.

Figure 3.2 The top view of the circular 8-coils array

The simulation model in Matlab of this 8-coils circular MIT system includes:

Step1 System Dimension: number of turns; coil's length along the cylinder; radius of the cylinder former; number of the segments and the current in coil.

Step2 Generate meshing model and using edge FEM to calculate all the locations of points within the measuring space.

Step3 Initial all A field array (A field data for all 8 coils)

Step4 The following step is the most important part of this simulation and it concludes three loops that are shown in Figure 3.3. It can be seen from Figure 3.2 that the shift angle between two neighbor coils is $\pi/4$, since that the rotation angle of 8-coils array can be obtained.

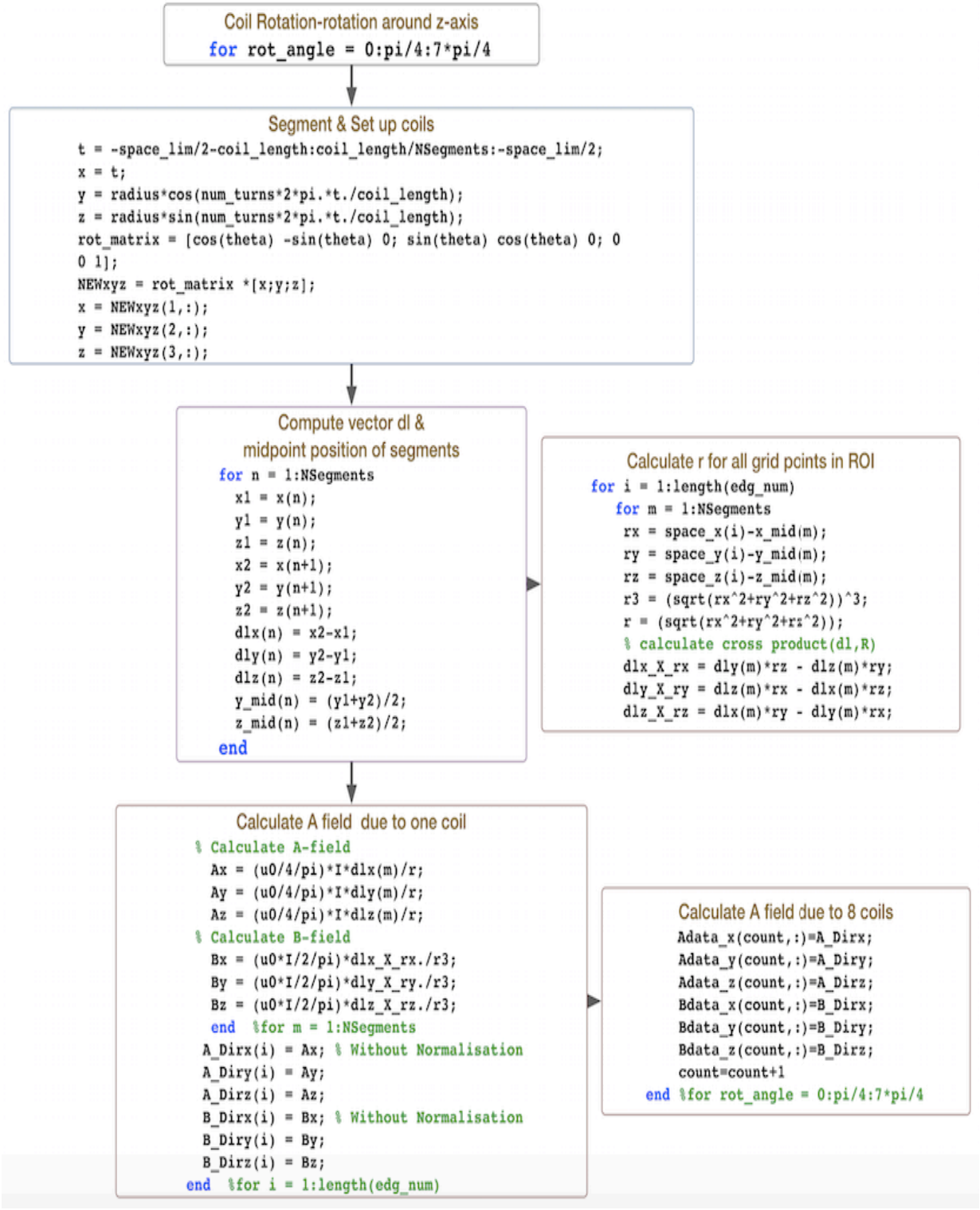

Figure 3.3 The loops used in this simulation

3.1.3 Simulation model (Software) of planar MIT system

The planar system presented in this theis is 9-coils planar MIT system. Figure 3.4 indicates the top view of an already developed 3×3 planar coil array. The sequence and the dimension of the new set up 9-coils planar coil array are shown in Figure 3.5. The radius of the coil is set to be 0.02cm and the distance between two coils is 0.05cm ($> 2 \times radius$). Assuming the position of coil 5 is $(0,0,0)$, according to the way of coils shifting, the positions of coil 1, coil3 and coil 9 are $(0,0.42,0.45)$, $(0,-0.42,0.45)$ and (0, -0.42, -0.45)

Figure 3.4 The top view of the 3×3 planar coil array [39]

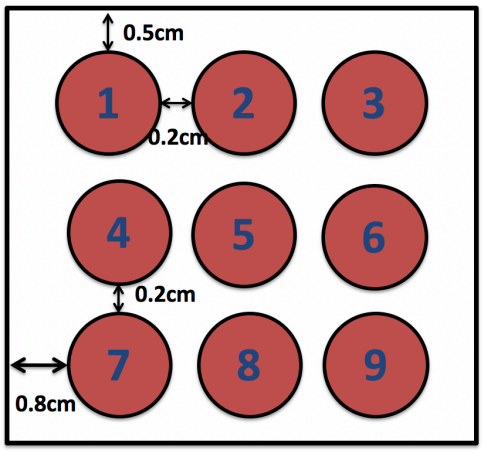

Figure 3.5 The dimension and sequence of the 9-planar coil array

The differences of the simulation model between circuit and planar sensor array are the system dimensions, the coil set up and the coil shifting.

The simulation process of 9-coils planar array can be explained as following:

Step1 Set the system dimension

Step2 Generate meshing model and using edge FEM to calculate all the locations of points within the measuring space, then initial all A field array (A field data for all 9 coils)

Step3 Segmenting coils and set up the coils: For the planar coil array, the B field in space point due to one single coil can be calculated in the same way as the circular coil array. Then the B field due to the other coils can be easily obtained by changing the coordinates of coil1 to coil

2,3…etc.

Step4 After breaking coils into small pieces, the current segments vector dl and the position of the midpoint of a segment can be calculated. The midpoint coordinates should be calculated to obtain the distance between segment and the space point.

Step5 Loop over all grid points and calculate the A field and B field at all the grid points in RIO due to one single coil.

Step6 The final step of this simulation is adding up all the A or B field due to one single coil to obtain the A field due to the whole planar coil array.

After all, the B field at any point within the region of interest due to the 9-coils planar array can be obtained.

3.2 Edge FEM on A_r, $A_r - \nabla V$ formulation

The forward problem in MIT can be explained by solving the eddy current problem, which are actually using Maxwell's equations [26]. To solving this problem, MIT domain is defined into three regions: the current source region (excitation coils region) Ω_s, receiving coils region Ω_r and the eddy current region Ω_e, (Figure 3.6), where $\Omega_c = \Omega_s + \Omega_e + \Omega_r$.

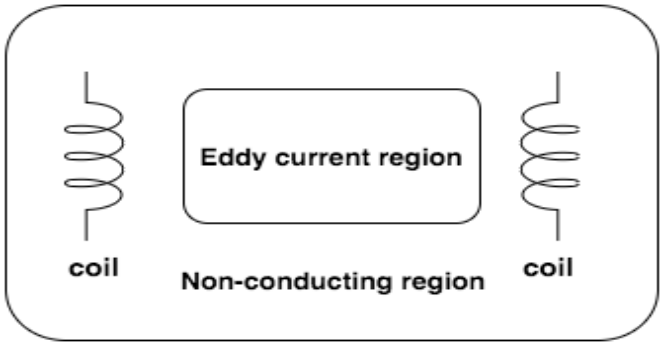

Figure 3.6 Three domains in MIT field system

It can be obtained from Figure 3.6, the eddy current region, which is significantly smaller than free space region [27], is enclosed within the non-conducting region

In order to solve the problem, the eddy current assumptions or approximation should be mentioned that the displacement current is neglected; there is no eddy current in excitation and measuring coils [28].

In this section, the edge finite element method is introduced by focusing on the eddy current formulation of A_r, $A_r - \nabla V$ [29].

- **In eddy current region Ω_e**

It should be mentioned that the electric filed in eddy current region is the sum of the primary magnetic vector potential [30] , the reduced vector potential [26] and the scalar field, which is shown in equation 3.7.

$$E_{total} = -j\omega A_s - j\omega A_r - j\omega \nabla V \tag{3.7}$$

Where E_{total} is the total electric field density, $\omega = 2\pi f$, f is the frequency in hz and ω is the angular frequency of alternating current in rad/s, A_s is the impressed magnetic vector potential (primary magnetic vector potential), A_r represents the reduced vector potential[31], ∇V is electrical scalar potential applied on the eddy current region only [32]:

$$B_{total} = \mu_0 H_s + \nabla \times A_r \tag{3.8}$$

$$B_{total} = \mu H_{total} \tag{3.9}$$

$$\nabla \times H_{total} = \sigma E_{total} \tag{3.10}$$

Where B_{total} is the total magnetic flux density, μ_0 represents the free space permeability, H_s is the magnetic field in current source region (free space), μ represents the magnetic permeability, H_{total} is the total magnetic field, σ represents the electric conductivity.

Based on the equation 3.7-3.10 and the eddy current approximation [33] [34], the Maxwell's equation in terms of magnetic vector potential can be written as [35] [36] [37]:

$$\nabla \times \frac{1}{\mu}(\nabla \times A_r) + j\omega\sigma A_r + j\omega\sigma\nabla V = -\nabla \times \frac{1}{\mu}(\mu_0 H_s) - j\omega\sigma A_s \quad in\ \Omega_e \tag{3.11}$$

- **In current source (excitation coils) region Ω_s**

$$B_s = \mu_0 H_s + \nabla \times A_r \tag{3.12}$$

$$B_s = \mu H_s \tag{3.13}$$

$$J_s = \nabla \times H_s \tag{3.14}$$

Where J_s is the source current density, B_s is the magnetic flux density in excitation coils region. Then it can be obtained through equation 3.12-3.14:

$$\nabla \times \frac{1}{\mu}\nabla \times A_r = \nabla \times H_s - \nabla \times \frac{1}{\mu}(\mu_0 H_s) \quad in\ \Omega_s \tag{3.15}$$

- **In receiving coils region Ω_r**

$$B_r = \mu_0 H_s + \nabla \times A_r \tag{3.16}$$

$$B_r = \mu H_r \tag{3.17}$$

$$J_r = \nabla \times H_r = 0 \tag{3.18}$$

Where H_r is the magnetic field in receiving coils, J_r is the current density in receiving coils, B_r is the magnetic flux density in receiving coils. Then it can be obtained through equation 3.16-3.18:

$$\nabla \times \frac{1}{\mu}\nabla \times A_r = -\nabla \times \frac{1}{\mu}(\mu_0 H_s) \quad in\ \Omega_r \tag{3.19}$$

In the case of $\mu_0 = \mu$, the A_r, $A_r - V$ formulations can be simplified as following:

$$\nabla \times \frac{1}{\mu_0}(\nabla \times A_r) + j\omega\sigma A_r + j\omega\sigma\nabla V = -\nabla \times H_s - j\omega\sigma A_s \quad in\ \Omega_e \tag{3.20}$$

$$\nabla \times \frac{1}{\mu_0}\nabla \times A_r = 0 \quad in\ \Omega_s \tag{3.21}$$

$$\nabla \times \frac{1}{\mu_0}\nabla \times A_r = -\nabla \times H_s \quad in\ \Omega_r \tag{3.22}$$

And the Dirichlet boundary conditions on the reduce vector potential is as following:

$$A_r \times n = 0\ and\ \left(\frac{1}{\mu}\nabla \times A_r\right) \times n = 0\ on\ boundary\ \Gamma_r \tag{3.23}$$

The Dirichlet boundary conditions on the vector and scalar potential are [38]:

$$A_r \times n = -A_s \times n\ \ on\ boundary\ \Gamma_s \tag{3.24}$$

$$n \cdot (jw\sigma A_r + jw\sigma\nabla V) = n \cdot (-jw\sigma A_s)\ on\ boundary\ \Gamma_s \tag{3.25}$$

3.3 Finite element Galerkin techinques

The reduced vector potential is approximately by edge basis functions [39] as

$$A_r \approx {A_r}^n = \sum_{k=1}^{n_e} a_k N_k \tag{3.26}$$

Where a_k is the line integrals of A_r along the edges and the electric scalar potential is approximately by node basis functions as

$$V \approx V^n = \sum_{k=1}^{n_n} V_k N_k \tag{3.27}$$

Where V_k is the nodal values of V^n.

Then using the basic functions N_i as weighting functions [26], the corresponding Galerkin equations in all three domains [37] [35]can be obtained from equation 3.20-22:

$$\frac{1}{\mu_0}\int_{\Omega_c}(\nabla \times N_i \cdot \nabla \times {A_r}^n)d\,\Omega + \int_{\Omega_e} j\omega\sigma N_i \cdot ({A_r}^n + \nabla \mathrm{V})\,d\,\Omega =$$

$$-\int_{\Omega_r+\Omega_e}(\nabla \times N_i \cdot \nabla \times H_s)d\,\Omega - \int_{\Omega_e}(j\omega\sigma N_i \cdot A_s)d\,\Omega \tag{3.28}$$

Obviously, the right-hand side of equation 3.28 can easily been calculated by Biot-Savart theory, which is introduce in Chapter 3.1. Then the induced voltage in measuring coil can be calculated by using the volume integration equation.

The induced voltage in the $m\,th$ coil produced by the source current in the $n\,th$ coil can be calculated as following:

$$V_{mn} = -\frac{j\omega}{S^m}\int_{\Omega_{s(m)}}(A^{(n)} \cdot {J_0}^{(m)})\,d\Omega \tag{3.29}$$

$$A^{(n)} = {A_r}^{(n)} + {A_s}^{(n)} \tag{3.30}$$

$${J_0}^{(m)} = \frac{{J_0}^{(m)}}{|{J_0}^{(m)}|} \tag{3.31}$$

$${J_0}^{(m)} = \frac{{J_0}^{(m)}}{|{J_0}^{(m)}|} \tag{3.32}$$

Where S^m is the cross-section area and J_0 is the unit current density passing through coil. Due to the relationship between induced voltage in the sensing coil and conductivity, the element of the Jacobian matrix can be expressed by

$$J_{mn} = \frac{\partial V_{mn}}{\partial \sigma_x} = -\omega^2\frac{\int_{\Omega_x} A_m \cdot A_n dv}{I} \tag{3.33}$$

where A_m is the forward solver of excitation coil m excited by I, A_n is the forward solver of sensor coil excited by unit current, σ_x is the conductivity of pixel x and Ω_x is the volume of the perturbation. And finally, Jacobian matrix will be transferred to solve the inverse problem.

3.4 Validation of forward problem

The accuracy of the MIT model can be explored by comparing simulation signals and the experimental results. This validation works is conducted both on circular and planar system through analytical analysis and fully eddy current problem analysis.

3.4.1 Validation of forward problem for circular MIT system

The proposed MIT system here is 8-coils planar sensor array MIT system introduced in Chapter 2.3.1 (Figure 2.4). And as mentioned before, the validation work can be divided to analytical analysis and fully eddy current problem analysis. All the parameters used in circular validation part are shown in Table 3.1.

Table 3.1 Parameters used in circular validation part

Number of coils	8
Number of turns	50
Coil length (cm)	1.4
Outer diameter (cm)	4.1
Inner diameter (cm)	3.9
Excitation current (A)	100
Size of aluminum sample (cm^3)	$4 \times 4 \times 5$
Electrical conductivity of aluminum sample (S/m)	3.5×10^7
Mesh generated	Nodes: 14446×3 *double* Surface: 8164×4 *double* Volume: 83796×5 *double*

❖ Analytical analysis

The way used to do the analytical analysis is same to the one used in planar system.

Step1: Simulating 8 cuboids including all the coils respectively, shown in Figure 3.7

Step2: Calculating induced voltages in every cuboid produced by sensor coils

Step3: Excluding the outside part of the cylinder, seen from Figure 3.8

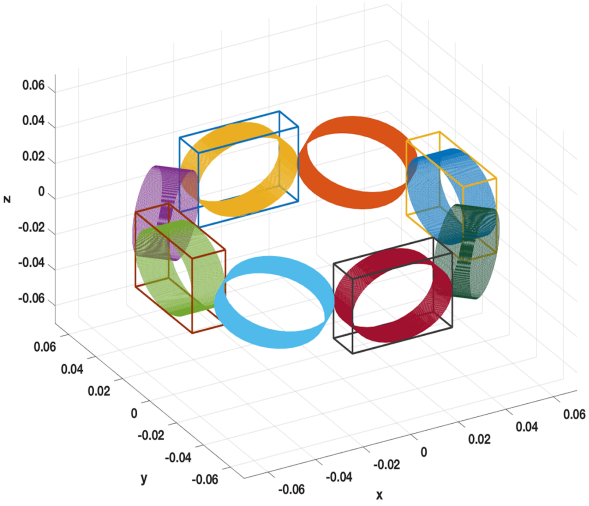

Figure 3.7 Simulating model of analytical analysis for circular MIT system

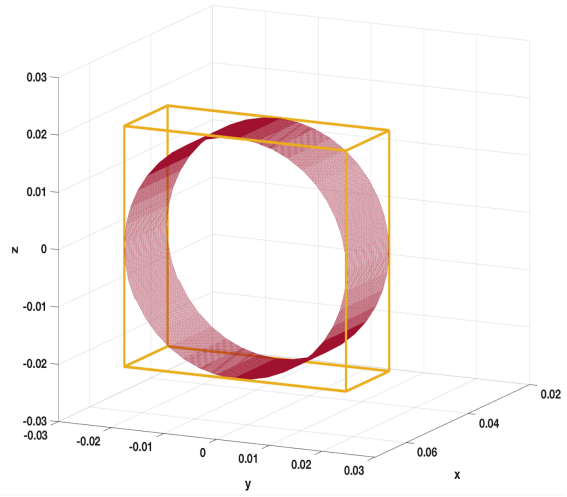

Figure 3.8 Simulating model of one cuboid box of Circular MIT system

The free space theoretical and experimental induced voltages are indicated in Figure 3.9. Each set has 28 measurements. The measurement protocol shown in below are in consistent with the data collection pattern mentioned in Chapter 2.3.1 as following: measurement index 1 means induced voltage obtained when coil1 is excitation coils and coil2 is receiving coil; index 28 means induced voltage measured at coil8 when coil7 is the excitation coil. The plots show an almost perfect match between simulation (theoretical) and experimental measurements.

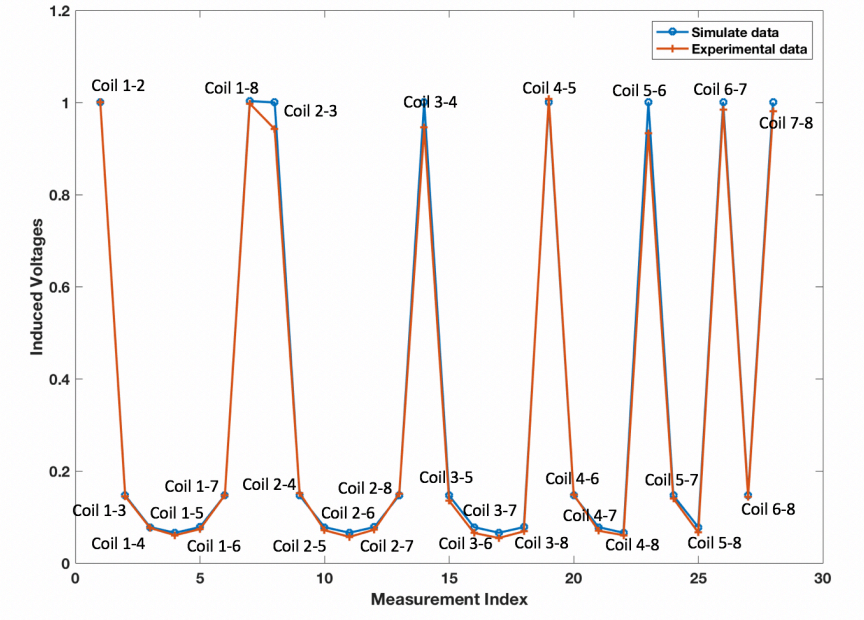

Figure 3.9 Comparison of theoretical and experimental results in circular sensor coils

❖ Fully eddy current problem analysis

✓ Background (free space) analysis

The information of mesh generated in this simulation is shown in Table 3.1. The plots of free space simulation and experimental induced voltage measurements, shown in Figure 3.11, indicates that although some degrees of errors are displayed, the theoretical and experimental results are matched.

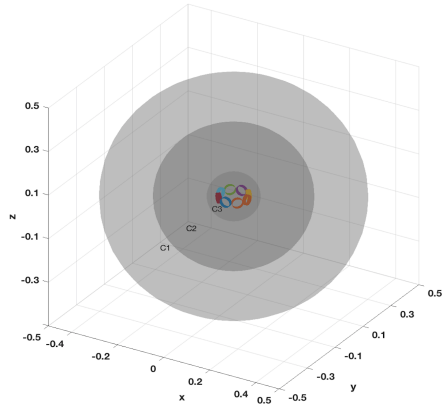

Figure 3.10 Mesh model of circular MIT system

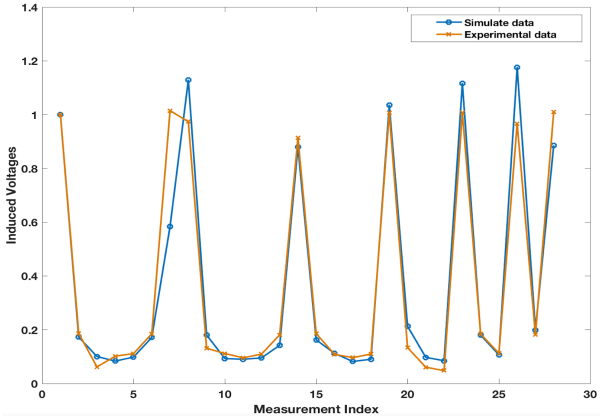

Figure 3.11 Comparison of free space induced voltage

✓ Experimental measurements due to the rod sample

The target sample conducted here is an aluminum cuboid. The results of placing the sample in four different positions are displayed in Figure 3.12. These four plots shown in above indicate that although some mismatches are existing, there is a good agreement between theoretical and experimental results, which means this proposed circular sensor array MIT system is stable.

Experiments	Comparison of induced voltage
Aluminum cuboid near coil1	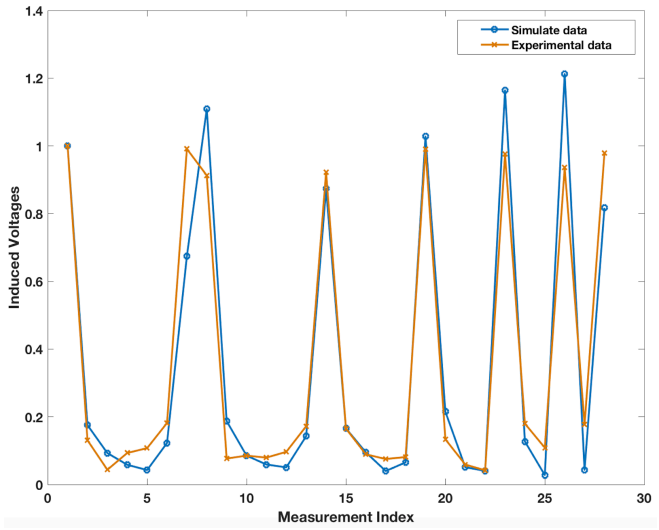
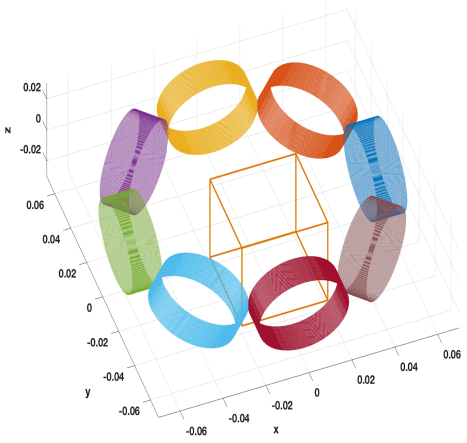	
Aluminum cuboid near coil7	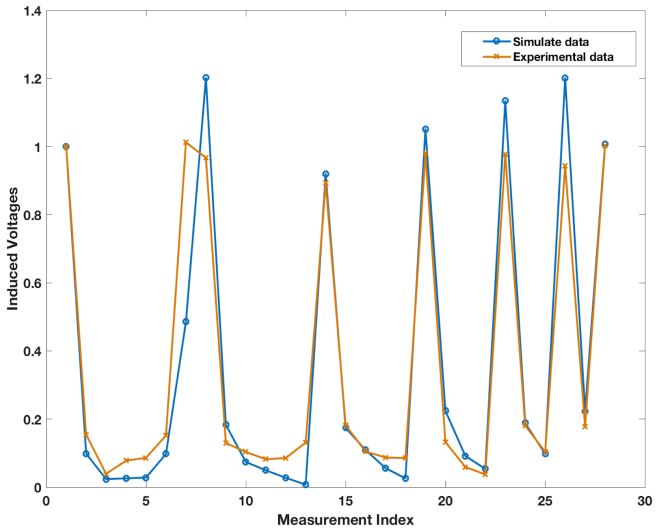
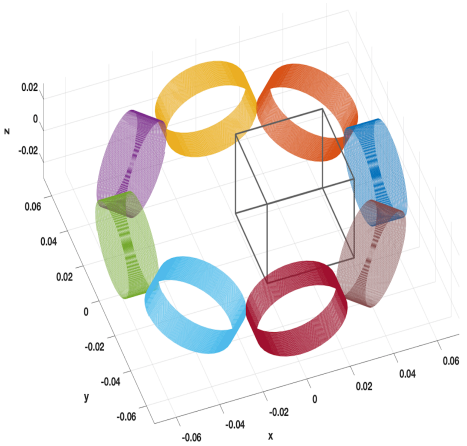	

Aluminum cuboid near coil5

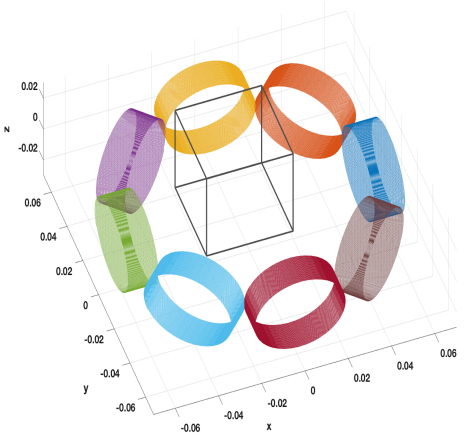

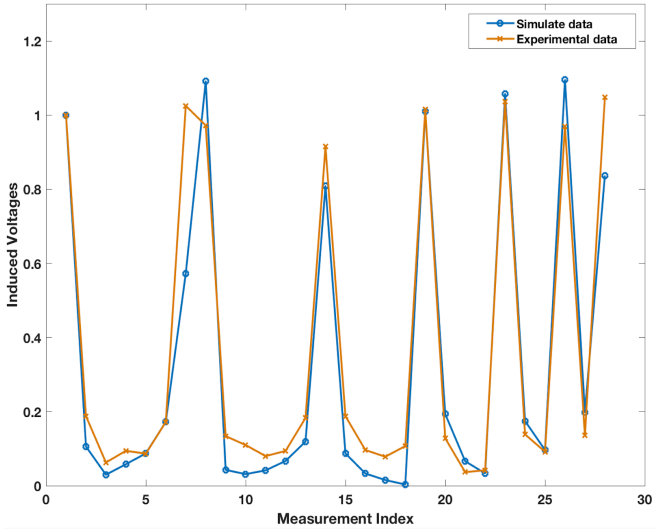

Aluminum cuboid near coil6

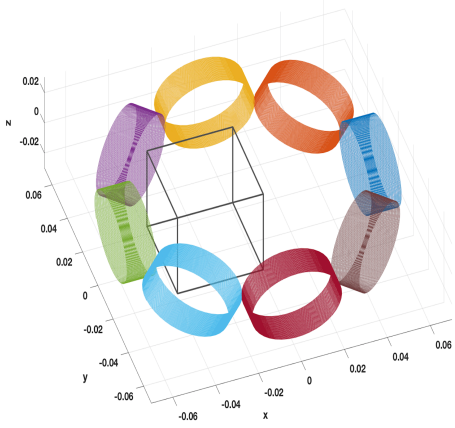

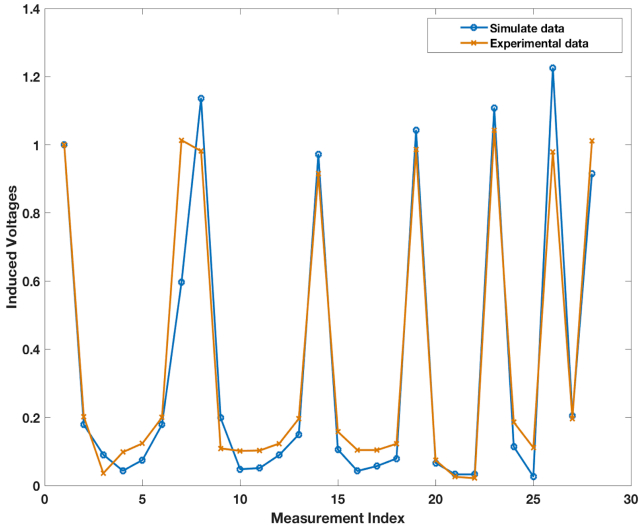

Figure 3.12 Validation results for circular MIT system

3.4.2 Validation of forward problem for planar MIT system

The proposed MIT system here is 9-coils planar sensor array MIT system introduced in Chapter 2.3.1 (Figure 2.5). The validation work includes analytical analysis and fully eddy current problem analysis. All the parameters used in circular validation part are shown in Table 3.2.

Table 3.2 Parameters used in planar validation part

Number of coils	9
Number of turns	100
Coil length (cm)	3.4
Outer diameter (cm)	4.1
Inner diameter (cm)	3.9
Excitation current (A)	100
Size of aluminum sample (cm^3)	$5 \times 4 \times 4$
Electrical conductivity of aluminum sample (S/m)	3.5×10^7
Mesh generated	Nodes: 14446×3 *double* Surface: 8164×4 *double* Volume: 83796×5 *double*

The sensitivity plot region of this proposed planar sensor array MIT system is shown in Figure 3.13, which illustrates that this planar sensor has a similar hemisphere-shaped sensitive region and achieved depth penetration up to 6cm.

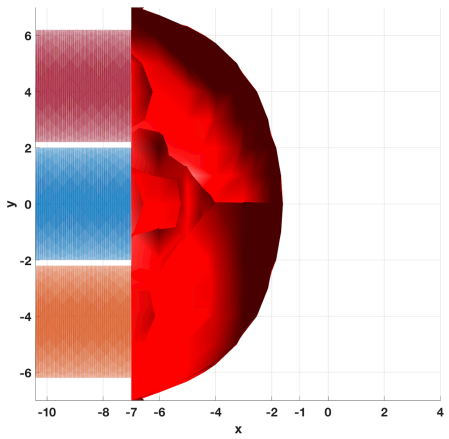

Figure 3.13 The sensitivity plot of this proposed planar sensor

❖ Analytical analysis

Step1: Simulating 9 cuboids including all the coils respectively, shown in Figure 3.14

Step2: Calculating induced voltages in every cuboid produced by sensor coils

Step3: Excluding the outside part of the cylinder, seen from Figure 3.15

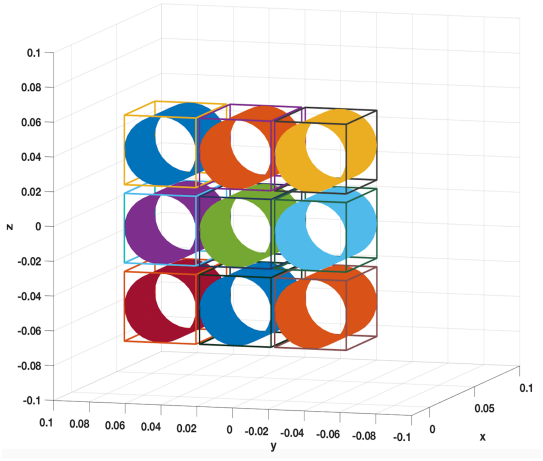

Figure 3.14 Simulating model of analytical analysis for planar MIT system

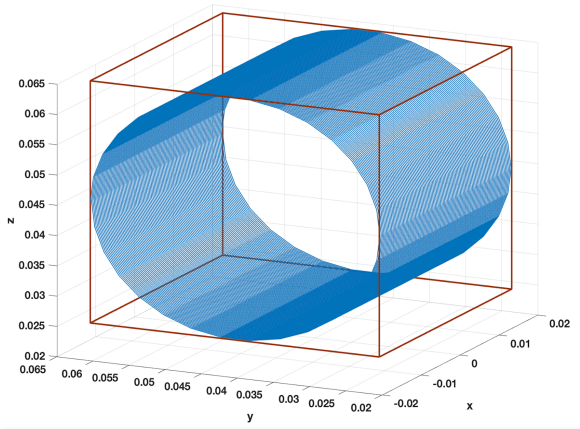

Figure 3.15 Simulating model of one cuboid box of Planar MIT system

The free space theoretical and experimental induced voltages are indicated in Figure 3.16. Each set has 36 measurements. The measurement protocol shown in below are in consistent with the data collection pattern mentioned in Chapter 2.3.1 as following: measurement index 1 means induced voltage obtained when coil1 is excitation coils and coil2 is receiving coil; index 5 means induced voltage measured at coil6 when coil1 is the excitation coil. The plots show a reasonable good match between simulation (theoretical) and experimental measurements despite some degrees expected errors.

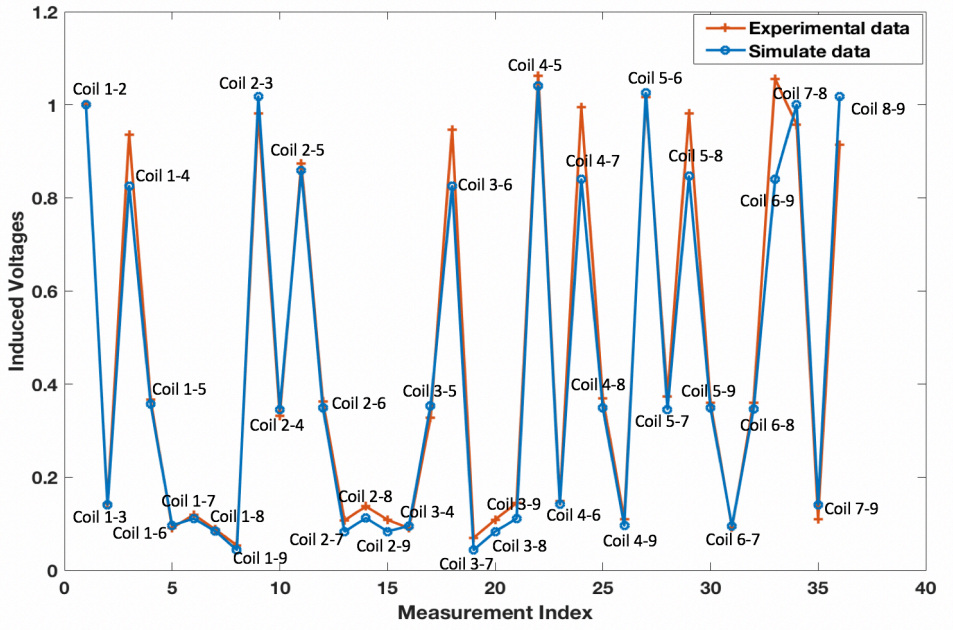

Figure 3.16 Comparison of free space induced voltage in planar sensor coils

❖ Fully eddy current problem analysis

✓ Background (free space) analysis

The information of mesh generated in this simulation is shown in Table 3.2. The plots of free space simulation and experimental induced voltage measurements, shown in Figure 3.18, indicates that the theoretical and experimental results are approximately matched.

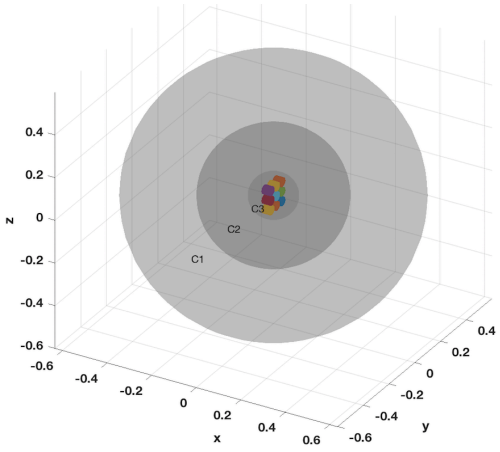

Figure 3.17 Mesh model of planar MIT system

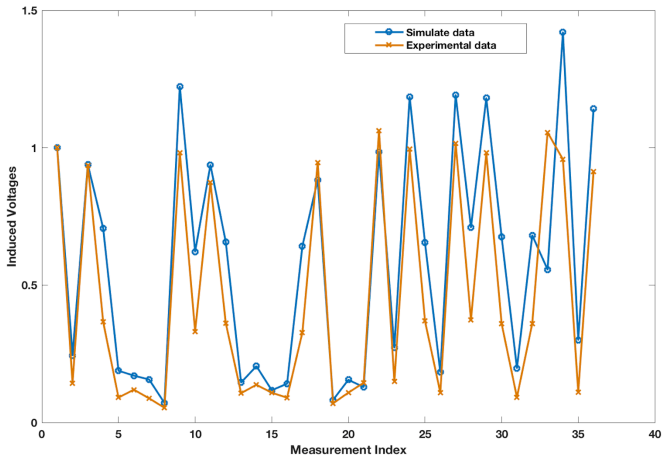

Figure 3.18 Comparison of free space induced voltage

✓ Experimental measurements due to the rod sample

The test sample conducted here is the same as the one used in circular validation. The results of placing the sample in seven different positions are displayed in Figure 3.19. These seven plots shown in below illustrate that although some mismatches are appeared, there is an approximately good agreement between theoretical and experimental results, which proves the stability and accuracy of this proposed planar sensor array MIT.

Experiments	Comparison of induced voltage
Aluminum cuboid near coil11 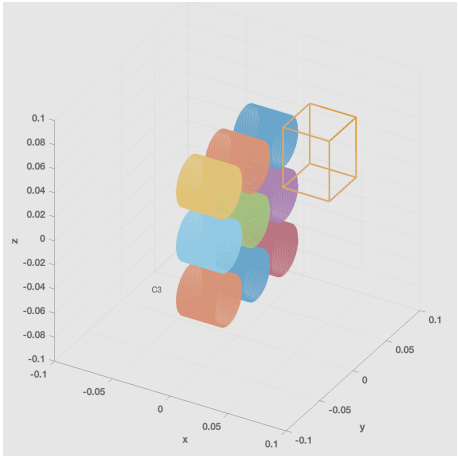	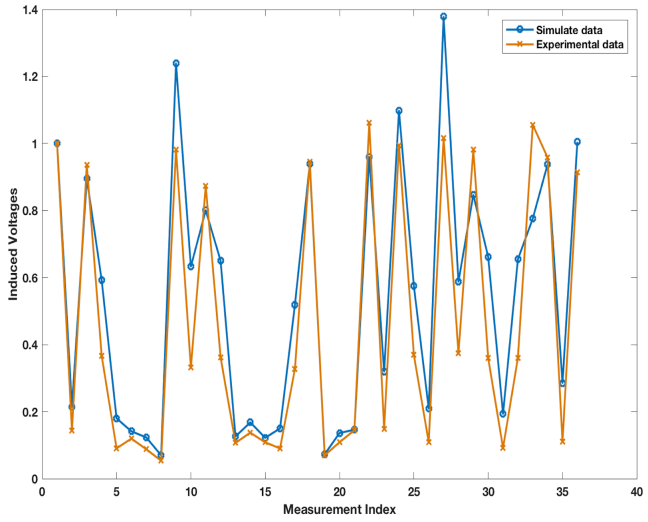
Aluminum cuboid near coil9 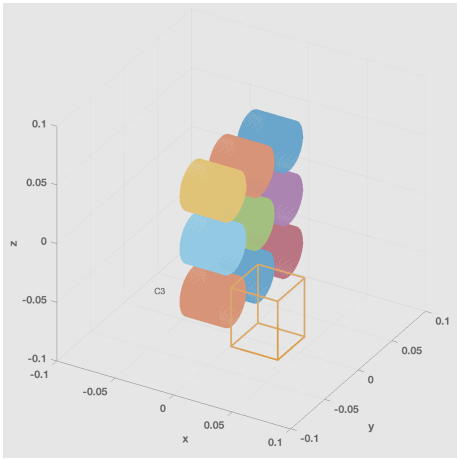	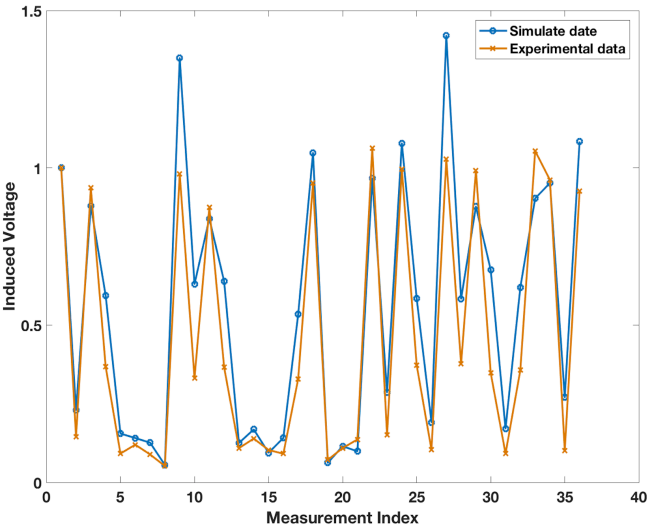

Cuboid $1cm$ away from the coil5

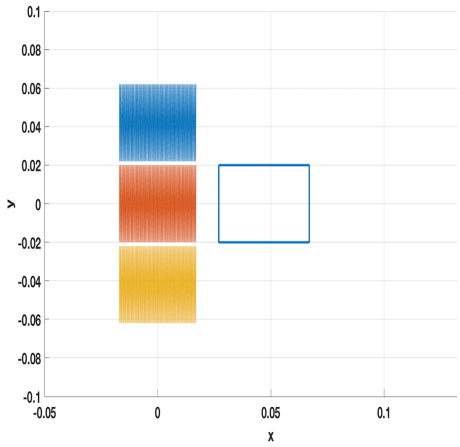

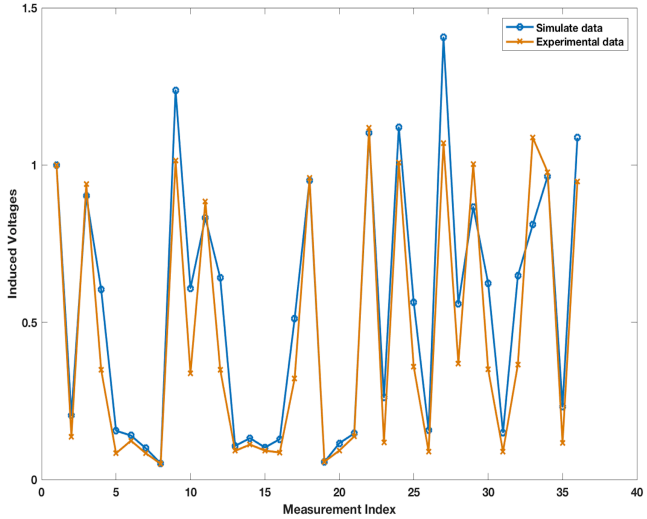

Cuboid $2cm$ away from the coil5

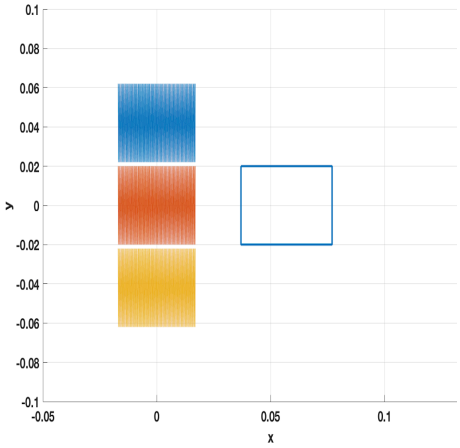

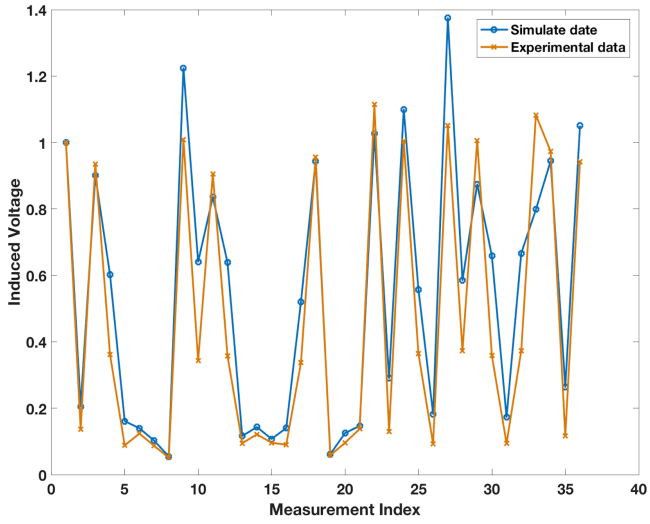

Cuboid $3cm$ away from the coil5

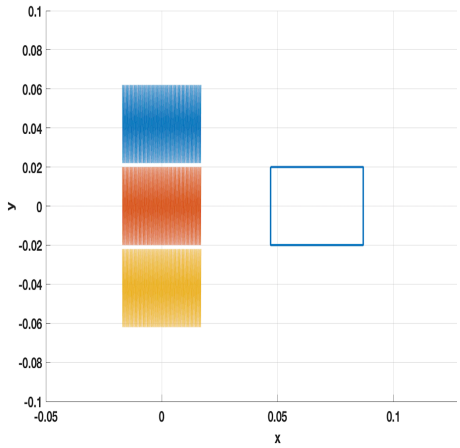

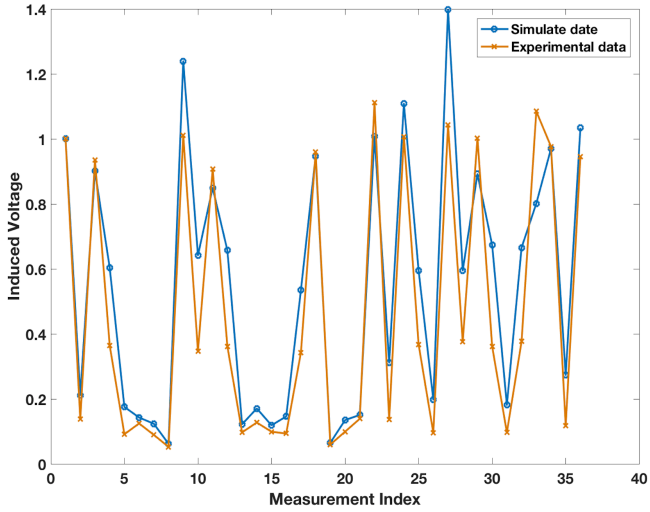

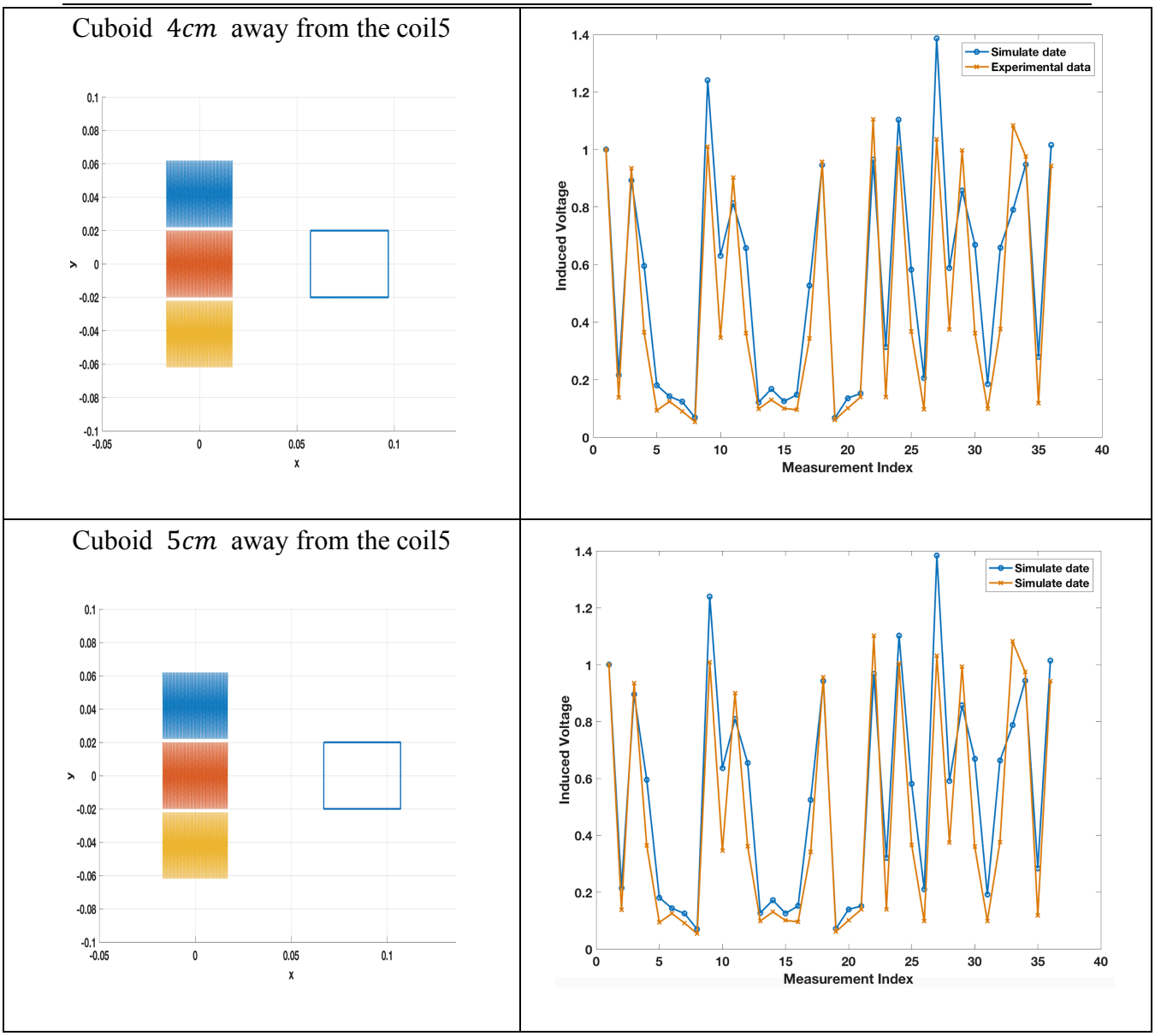

Figure 3.19 Validation results for planar MIT system

3.5 Conclusions

Some definitions and basic theories in forward problem of MIT have been discussed in the first part of this chapter. It has been proved that the forward problem can be explained by the eddy current problem using Maxwell's equations. And edge FEM method is introduced to simplify the whole meshing model. The main part of this chapter is the simulation model of Biot-Savart Law in circular coil array as well as planar coil array, it clearly shows that Biot-Savart law can be treated a reasonable method used in eddy current model to calculate B field to increase the flexibility of both circular sensor array and planar sensor array MIT system.

CHAPTER 4 INVERSE PROBLEM

The inverse problem of MIT is solving the conductivity distribution of reconstruction image with a set of given boundary measurements of mutual inductances between pairs of coils [40] [41].

Generally, the MIT problem is really difficulty since the non-local nature of conductivity imaging [42], which means in order to find the conductivity image one must solve a scheme of equations linking every pixel or voxel to every measurement. Worse than that is the severely ill posed and ill conditioned property of inverse problem. According to Hadamard [43] a mathematical model of physical problem is well posed if

- For all acceptable data, a solution exists
- For all acceptable data, the solution is unique
- The solution's behavior changes continuously with the initial conditions

Actually, we try to solve the conductivity of the object since we believe the body has a conductivity, which means existence of a solution is not really a problem. The matter is more that the data are sufficiently accurate or not. The third criterion makes the most trouble to solve the problem. It means that there are an enormous number of imperceptible changes in the conductivity distribution with the given measurement precision. In order to violate the instability of the solution, enough information those can be used to constrain the problem should be obtained in advance.

4.1 Regularizing linear ill-posed problem

Firstly, we consider this problem as a linear ill posed problem, and in a linearized MIT inverse model [44],

$$J\Delta\sigma = \Delta v \tag{4.1}$$

Where J is the Jacobian or sensitivity matrix ($J \in R^{m\times n}$), $\Delta\sigma$ and Δv are complex vectors, $\Delta\sigma$ is the conductivity change distribution ($\Delta\sigma \in R^n$) and Δv is the time difference measurement of induced voltage ($\Delta v \in R^m$).

If the inverse of A exists, equation 4.1 could be solved directly by

$$\Delta\sigma = J^{-1}\Delta v \tag{4.2}$$

However, the inverse of J doesn't exist in most case, since in most cases J is not a square matrix (the number of unknown variables or the number of pixels is usually much larger than the number of measurements). So, we need to use the Moore-Penrose generalized inverse shown as below.

$$\Delta\sigma = J^{+}\Delta v \tag{4.3}$$

Where $J^{+} = (J^T J)^{-1}J^T$ for the over determined case ($m \geq n$) and $J^{+} = J^T(JJ^T)^{-1}$ for the under determined case ($m \leq n$) [45].

Besides, the other method should be considered. A number of algorithms have been developed to address the ill-posed and ill-conditioned problems. Generally, they can be divided into two categories, iterative algorithms and non-iterative (or single step) algorithms. Tikhonov regularization and TV regularization are the main focus of this chapter. Other general regularization applied to solve the inverse problem of MIT are introduced in Appendix A.

4.2 Non-iterative algorithms: Tikhonov regularization

When the measurement errors are considered

$$J\Delta\sigma = \Delta v + e \tag{4.4}$$

Where e is the measurement error vector.

A reasonably good method to obtain the solution of equation 4.4 is to find an $\Delta\sigma_x$ that fits the data be the best, which is to minimize $\|J\Delta\sigma - \Delta v\|^2$ and also called the least square solution [46].

$$\Delta\sigma_x = argmin_\sigma \|J\Delta\sigma - \Delta v\|^2 \tag{4.5}$$

Equation 4.5 can be solved as following:

$$\Delta\sigma_x = (J\Delta\sigma - \Delta v)^T(J\Delta\sigma - \Delta v) = \Delta\sigma^T J^T J\Delta\sigma - 2(J\Delta\sigma)^T\Delta v + \Delta v^T\Delta v \tag{4.6}$$

To find the minimum cost function, the first derivative of the cost function equal to zero.

For a symmetric matrix C, $\frac{\partial}{\partial x}(x^T Cx) = 2e_k Cx$

$$\frac{\partial\Delta\sigma_x}{\partial\Delta\sigma} = 2e_k J^T J\Delta\sigma - 2e_k J^T\Delta v = 0 \tag{4.7}$$

Giving

$$J^T J\Delta\sigma = J^T\Delta v \tag{4.8}$$

If the inverse of $J^T J$ existed, the solution of equation 4.5 is

$$\Delta\sigma = (J^T J)^{-1} J^T\Delta v \tag{4.9}$$

However, the inverse of $J^T J$ does not exist in most cases because the matrix is ill posed.

In order to make its inverse exist, matrix $J^T J$ must be modified into $J^T J + \alpha^2 I$, where I is an identity matrix and α is called regularization parameter. Then the solution of equation 4.5 is

as following

$$\Delta\sigma = (J^T J + \alpha^2 I)^{-1} J^T \Delta v \tag{4.10}$$

This is so called Tikhonov regularization method, which was introduced by Hoerl for finite dimensional problems and to solve integral equations by Phillips and Tikhonov [47].

Besides, there is a more general form of Tikhonov regularization that is shown as following.

When we go back to equation 4.5, a big change in $\Delta\sigma$ makes a small change on the measurement, which means the optimization is not that correct. Since the inverse problem is ill posed, a Tikhonov regularization penalty term $G_{TK}(\Delta\sigma)$ can be added to the optimization problem to overcome the ill-posedness[47] [48].

$$\Delta\sigma_x = argmin_{\Delta\sigma}(\|J\Delta\sigma - \Delta v\|^2 + G_{TK}(\Delta\sigma)) \tag{4.11}$$

$$G_{TK}(\Delta\sigma) = \alpha^2 \|R(\Delta\sigma - \Delta\sigma_0)\|^2 \tag{4.12}$$

$$\Delta\sigma_x = argmin_{\Delta\sigma}\|J\Delta\sigma - \Delta v\|^2 + \alpha^2 \|R(\Delta\sigma - \Delta\sigma_0)\|^2 \tag{4.13}$$

Where R is a regularization matrix and α is the regularization parameter.

Minimizing this function means that the least square of the difference between measured voltage and the estimated voltage is minimized while the solution is kept reasonably close to the estimated image $\Delta\sigma_0$. Notice that when $\alpha \to 0$, $\Delta\sigma_x$ tends to be a generalized solution $J^+\Delta v$, shown in equation 4.3.

The equation 4.13 to be minimized can be expanded as follows.

$$\Delta\sigma_x = argmin_{\Delta\sigma}\{M(\Delta\sigma)\} \tag{4.14}$$

$$M(\Delta\sigma) = \Delta\sigma^T J^T J\Delta\sigma - 2(\Delta v)^T J\Delta\sigma + \Delta v^T \Delta v$$

$$+\alpha^2[R(\Delta\sigma - \Delta\sigma_0)]^T[R(\Delta\sigma - \Delta\sigma_0)] \tag{4.15}$$

where equation 4.15 is the cost function. The minimum of cost function can be obtained by setting its first derivative equal to zero.

We can apply the following rule into upper equation:

$$\frac{\partial}{\partial x}[F(x)^T F(x)] = 2F(x)^T \frac{\partial}{\partial x} F(x) \tag{4.16}$$

Then we can get

$$\begin{aligned} &2(\Delta\sigma)^T J^T J \frac{\partial}{\partial \Delta\sigma}(\Delta\sigma) - 2\Delta v^T \frac{\partial}{\partial \Delta\sigma}(J\Delta\sigma) \\ &+ \alpha^2 [R\,(\Delta\sigma - \Delta\sigma_0)]^T \frac{\partial}{\partial \Delta\sigma}[R\,(\Delta\sigma - \Delta\sigma_0)] \\ &= 2(\Delta\sigma)^T J^T J - 2\Delta v^T J + 2\alpha^2 [R\,(\Delta\sigma - \Delta\sigma_0)]^T R = 0 \end{aligned} \tag{4.17}$$

By transposing both sides of the equation 4.17 and simplified, we get

$$J^T \Delta v - J^T J \Delta\sigma - \alpha^2 R^T R \Delta\sigma + \alpha^2 R^T R \Delta\sigma_0 = 0$$

$$(J^T J + \alpha^2 R^T R)\Delta\sigma = J^T \Delta v + \alpha^2 R^T R \Delta\sigma_0 \tag{4.18}$$

The standard Tikhonov method is obtained by replacing R by I, the identity matrix, R=I, and assuming $\Delta\sigma_0 = 0$, then we can find an explicit formula for the minimum

$$\Delta\sigma = (J^T J + \alpha^2 I)^{-1} J^T \Delta v \tag{4.19}$$

Now the singular values from J are all increased by a number α^2 and in this case, more singular values will satisfy the Picard criterion [49] and more information can be extracted for image reconstruction.

The condition number of the matrix $(J^T J + \alpha^2 I)^{-1}$ is $\frac{\lambda_1 + \alpha^2}{\lambda_n + \alpha^2}$, and λ_i are the eigenvalues of $J^T J$ and in decreasing order. The condition number is close to $\frac{\lambda_1}{\alpha^2} + 1$ with λ_n is small and so for a big α the matrix is well conditioned. Besides, the quality of Tikhonov regularization depends on the crucial choose of the regularization parameter [50]. In general, a large value of

α dampen the data errors but increase the approximation error while a small value of α gives a good approximation to the original problem but increase the data error. Generally, the value of regularization parameter is chosen empirically in most cases at present.

Although standard Tikhonov is widely used for many applications, recently a hybrid Tikhonov regularization was shown to produce better imaging results [51] . To provide a fair comparison with the proposed TV algorithm we chose the most advanced hybrid Tikhonov method based on combining Laplacian and Tikhonov based regularization terms [51]

$$\Delta\sigma = (J^T J + \gamma^2 R_1 + \lambda^2 R_2)^{-1} J^T \Delta v \tag{4.20}$$

where R_1 is a Laplacian regularization term, R_2 is an identity matrix, and γ and λ are the regularization factors for R_1 and R_2, respectively. The hybrid Tikhonov method has good quality in challenging low conductivity MIT data. Here we empirically selected the regularization parameters for low conductivity and high conductivity reconstruction and used the same parameters in all experimental studies.

4.3 Iterative algorithms: Total variation regularization

The total variation problem is defined by adding a penalty term to equation 4.5, the $l_1 - norm$ of the gradient of the image, or the so called, total variation regularization term $G_{TV}\ (\Delta\sigma)$

$$G_{TV}\ (\Delta\sigma) = \alpha R(\Delta\sigma) = \alpha \|\nabla\ \Delta\sigma\|_1 \tag{4.21}$$

where α is the regularization parameter, ∇ is the gradient and $\|\cdot\|_1$ is the $l_1 - norm$.

The total variation method aims to solve the following constrained optimization problem

$$\Delta\sigma = argmin_{\Delta\sigma} \|\nabla\Delta\sigma\|_1 \ such\ that$$

$$\|J\Delta\sigma - \Delta v\|^2 \leq \rho \tag{4.22}$$

where ρ accounts for noisy data and $\|\nabla \Delta\sigma\|_1$ is the total variation functional, ∇ the spatial gradient and $\|\cdot\|_1$ the $l_1 - norm$.

4.3.1 Isotropic and anisotropic total variation methods

The isotropic version of the discrete TV functional as proposed in [52] is usually adopted:

$$\|\nabla \Delta\sigma\|_1 = \sum_{i=1}^{n} \sqrt{(\nabla_x \Delta\sigma)_i^2 + \left(\nabla_y \Delta\sigma\right)_i^2 + (\nabla_z \Delta\sigma)_i^2} \tag{4.23}$$

where *n* is the number of pixels in the image.

The anisotropic form of TV allows to separate and to weight the contributions along the different directions:

$$\|\nabla \Delta\sigma\|_1 = \alpha_x \|\nabla_x \Delta\sigma\|_1 + \alpha_y \left\|\nabla_y \Delta\sigma\right\|_1 + \quad \alpha_z \|\nabla_z \Delta\sigma\|_1 \tag{4.24}$$

4.3.2 Resolution with the Split Bregman method

The constrained problem equation 4.22 can be solved using standard optimization approaches, but these can be computationally expensive and difficult to implement. A simpler and efficient approach is to build a regularization scheme based on the use of the Bregman distance, which leads to a sequence of unconstrained problems whose solution converge to the solution of the constrained problem equation 4.22 [53].

TV regularization was applied to metallic MIT in [38] [54], so further evaluation was needed for low conductivity MIT.

For a given convex function $C\,(x)$, the Bregman distance between x and y can be defined as

$$D_C\,(x, y) = C\,(x) - C\,(y) - < s, x - y > \tag{4.25}$$

where s is the subgradient of C at y, and $<,>$ denotes the scalar product. In this case, let $C(x) = TV(x)$ be the total variation function, and $\Delta\sigma$ and $\Delta\sigma^k$ the optimal and iterative solution, respectively. Then the Bregman iterative algorithm can be expressed as the following iterative procedure:

$$\Delta\sigma^{k+1} = argmin_{\Delta\sigma} D_C(\Delta\sigma, \Delta\sigma^k) + \frac{\mu}{2}\|J\Delta\sigma - \Delta v\|^2 \quad (4.26)$$

$$s^{k+1} = s^k - \mu J^T(J\Delta\sigma^{k+1} - \Delta v) \quad (4.27)$$

where s^{k+1} is the sub gradient of the total variation function at the $(k+1)\,th$-iteration.

Equation 4.26 and equation 4.37 constitute the iterative scheme based on the Bregman distance associated to TV functional, which for linear operators, *J*, can be simplified to [55]

$$\Delta\sigma^{k+1} = argmin_{\Delta\sigma}\{\|\nabla\Delta\sigma\|_1 + \frac{\mu}{2}\|J\Delta\sigma - (\Delta v)^k\|^2\} \quad (4.28)$$

$$\Delta v^{k+1} = \Delta v^k + \Delta v - J\Delta\sigma^{k+1} \quad (4.29)$$

Equation 4.28 can be solved now at every iteration with conventional unconstrained optimization algorithms. However, it is still difficult to solve because of the non-differentiability of the TV functional.

The split Bregman method can extend the utility of the Bregman iteration to minimize the TV functional in an efficient manner [52]. Auxiliary variables can be used to convert equation 4.28 to a constrained optimization problem in which L2- and L1-problems are decoupled and so easier to solve. We develop the solution only for isotropic TV and then give the solution for anisotropic TV.

For isotropic TV, equation 4.28 becomes

$$(\Delta\sigma^{k+1}, d_i^{k+1}) = argmin_{\Delta\sigma,d}\frac{\mu}{2}\|J\Delta\sigma - \Delta v^k\|^2 + \left\|(d_x, d_y, d_z)\right\|_1$$

$$such\ that\ \ d_i = \nabla_i\,\Delta\sigma \quad (4.30)$$

where *i*=*x*,*y*,*z*.

To solve this constrained problem, after applying the Bregman iteration as above, the equation 4.30 can be written as

$$(\Delta\sigma^{k+1}, d_i^{k+1}) = argmin_{\Delta\sigma,d_i} \frac{\mu}{2}\|J\Delta\sigma - \Delta v^k\|^2 + \left\|(d_x, d_y, d_z)\right\|_1$$

$$+ \sum_i \frac{\lambda}{2}\left\|d_i - \nabla_i\Delta\sigma - b_i^k\right\|^2 \tag{4.31}$$

$$b_i^{k+1} = b_i^k + \nabla_i\Delta\sigma^{k+1} - d_i^{k+1} \tag{4.32}$$

Then minimizing equation 4.31 can be achieved by minimizing $\Delta\sigma$ and d_i separately as following [55]:

$$\Delta\sigma^{k+1} = argmin_{\Delta\sigma}\frac{\mu}{2}\|J\Delta\sigma - \Delta v^k\|^2 + \sum_i \frac{\lambda}{2}\left\|d_i^k - \nabla_i\Delta\sigma - b_i^k\right\|^2 \tag{4.33}$$

$$d_i^{k+1} = argmin_{d_i}\left\|(d_x, d_y, d_z)\right\|_1 + \sum_i \frac{\lambda}{2}\left\|d_i - \nabla_i\Delta\sigma^{k+1} - b_i^k\right\|^2 \tag{4.34}$$

Solutions to $\Delta\sigma^{k+1}$ and d_i^{k+1} are given by analytic expressions that can be efficiently computed. $\Delta\sigma^{k+1}$ is given in terms of a linear system and d_i^{k+1} by a shrinkage formula for isotropic formulation [52] .The solution for the isotropic TV problem is given as follows:

$$(\mu J^T J + \lambda\sum_i \nabla_i^T\nabla_i)\Delta\sigma^{k+1} = \mu J^T\Delta v^k + \lambda\sum_i \nabla_i^T\left(b_i^k - d_i^k\right) \tag{4.35}$$

$$d_i^{k+1} = \max\left(p^k - \frac{1}{\lambda}, 0\right)\frac{\nabla_i\Delta\sigma^{k+1} + b_i^k}{p^k} \tag{4.36}$$

$$p^k = \sqrt{\sum_i\left|\nabla_i\Delta\sigma^{k+1} + b_i^k\right|^2} \tag{4.37}$$

$$b_i^{k+1} = b_i^k + \nabla_i\Delta\sigma^{k+1} - d_i^{k+1} \tag{4.38}$$

$$\Delta v^{k+1} = \Delta v^k + \Delta v - J\Delta\sigma^{k+1} \tag{4.39}$$

For anisotropic TV, equation 4.31 becomes

$$\left((\Delta\sigma^{k+1}, d_i^{k+1}\right) = argmin_{\Delta\sigma, d_i} \frac{\mu}{2} \|J\Delta\sigma - \Delta v^k\|^2 + \sum_i \alpha_i \|\nabla_i \Delta\sigma\|_1$$

$$such\ that\ \ d_i = \nabla_i \Delta\sigma \tag{4.40}$$

where *i*=*x*,*y*,*z*. Proceeding as above, the final solution for the anisotropic TV problem gives the same solution for $\Delta\sigma^{k+1}$ but auxiliary variables d_i are now given by a different shrinkage formula:

$$d_i^{k+1} = \max\left(\left|\nabla_i \Delta\sigma^{k+1} + b_i^k\right| - \frac{\alpha_i}{\lambda}, 0\right) \frac{\nabla_i \Delta\sigma^{k+1} + b_i^k}{\left|\nabla_i \Delta\sigma^{k+1} + b_i^k\right|} \tag{4.41}$$

The only difference between isotropic and anisotropic formulations are the shrinkage or thresholding operations that impose TV iteratively.

Hence, the split Bregman method provides a sequence of solutions $(\Delta\sigma^{k+1}, {d_i}^{k+1})$ that converges to the solution of the constrained optimization problem equation 4.22. One of the benefits of the split Bregman formulation is that it does not require explicit calculation of the derivatives of the TV functional, which must be otherwise approximated because of the no differentiability of the TV functional. These approximations used by more standard approaches are generally non-optimal and lead to slow convergence.

4.4 Regularizing non-linear ill-posed problem

Newton-Raphson and iterative Tikhonov method [56]is the main method to solve the non-linear ill-posed inverse problem.

Newton-Raphason method is an iterative method, which was developed to find the root of a non-linear function. Suppose f is the transform function from conductivity x to measurement v. Assuming there is no measurement error, the relationship can be described as

$$v = f(x) \tag{4.42}$$

The reconstruction process is to find the best candidate value of x that minimize the square error e

$$e = \frac{1}{2}[f(x) - v]^T[f(x) - v] \tag{4.43}$$

Differentiate e with respect to x to find an extreme value of x to minimize e

$$e' = \frac{\partial e}{\partial x} = [f'(x)]^T[f(x) - v] = 0 \tag{4.44}$$

Using a Taylor series expansion of e' around a point $x = x_k$ and omit the high order terms.

$$e' = e'(x_k) + e''(x_k)\Delta x_k \tag{4.45}$$

$$\Delta x_k = x - x_k \tag{4.46}$$

e'' is called Hessian Matrix [57] and

$$e'' \approx [f'(x)]^T f'(x) \tag{4.47}$$

Then we put equation 4.45-47 together, we can get

$$e'(x) = [f'(x_k)]^T[f(x_k) - v] + [f'(x_k)]^T f'(x_k)\Delta x_k \tag{4.48}$$

Let equation 4.48 equals to zero, we can get

$$\Delta x_k = -\{[f'(x_k)]^T f'(x_k)\}^{-1}[f'(x_k)]^T[f(x_k) - v] \tag{4.49}$$

In principle, $f'(x_k)$ and $f(x_k)$ should be updated at every iteration and this is so called Newton-Raphson method. Equation 4.49 can be simplified as following

$$\Delta x_k = -({S_k}^T S_k)^{-1}{S_k}^T[v_k - v] \tag{4.50}$$

Then we can obtain

$$x_{k+1} = x_k - ({S_k}^T S_k)^{-1}{S_k}^T[v_k - v] \tag{4.51}$$

However, the inverse of ${S_k}^T S_k$ does not exist in most cases, so a term $\alpha^2 I$ should be added to ${S_k}^T S_k$ to make its inverse exist, which is the same as Tikhonov regularization. The modified Newton-Raphson iterative algorithm is as following [58].

$$x_{k+1} = x_k - (S^T S + \alpha^2 I)^{-1} S^T [S x_k - v] \tag{4.52}$$

4.5 Best practice (do and not do)

The following is some guidelines that can help one to avoid the common pitfalls and to obtain the best practice.

- Simulating noise(errors)

  When simulating experimental data, the noise in experimental measurements should also be considered that means the errors must also be simulated [3]. There are many sources of error especially in the data collection system, such as gain errors, stray capacitance, wrong electrode position and incorrect predicted boundary shape.

- Not tweaking

  There are a number of alterable parameters in reconstruction program such as the number of Landweber iterations and Tikhonov regulation parameters. Besides, there are variable methods to choose the acceptable values. During the reconstruction process, one should avoid changing the reconstruction parameters all the time until obtain an image which one is close to the forecast [9], which means one shouldn't tweaking the parameters but show all the results no matter the parameters perform poorly or well.

CHAPTER 5 TV REGULARIZATION ON CIRCULAR MIT

MIT is an imaging modality with a wide range of potential applications due to its non-contact nature. MIT is a member of the electrical tomography family that faces the most difficult imaging challenges, due to its demanding measurement accuracy requirements and its difficult forward and inverse problems. This chapter presents for the first time split Bregman total variation (TV) regularization to solve the MIT inverse problem. Comparative evaluations are presented between proposed TV algorithm and more commonly used Tikhonov regularization method. Tikhonov regularization which is based on the $l_2 - norm$ is solved linearly while TV is solved using the Split Bregman formulation, which has been shown to be optimal for $l_1 - norm$ regularization. Experimental results are quantified by a number of image quality measurements, which show the superiority of the proposed TV method both on low conductivity and high conductivity MIT data. Significant improvement in MIT imaging results will make the proposed TV method a great candidate for both types of MIT imaging.

5.1 Introduction

Although MIT is capable of imaging all PEP, it usually aims at visualizing the conductivity distribution of the object under test, which can be achieved by modeling eddy currents in the forward model [23] and then identifying the conductivity distribution inverse problem. The inverse problem in MIT is severely ill posed, so regularization is needed. Tikhonov regularization method, based on solving the least square solution, is widely used to solve the inverse MIT problem [30]. However, this leads to suboptimal results, with over smoothed reconstructed images that show blurred edges and boundaries between materials. A better option is to use an $l_1 - norm$ regularization, such as total variation (TV) functional, which has been shown to improve image quality in MIT and other applications, and has received

considerable attention in the past few years [38, 54, 59]. However, the TV functional has few drawbacks. TV is non-differentiable, which is commonly avoided by using an approximation. Smooth approximations of TV can have an effect in image quality, blurring sharp edge [60]. This effect can be reduced by tuning the parameter that controls the approximation of TV, which can lead to slow down in convergence. In addition, TV method suffers from low contrast recovery [60, 61].

Iterative methods based on the Bregman iteration have been proposed as a possible solution to these problems. The use of Bregman iterations for TV minimization introduced in [53] fixed the low contrast recovery problem of standard TV, by providing a sequence of solutions that allows to recover the contrast lost by the TV functional and to lead to lower error [60]. Furthermore, the split Bregman formulation presented in [52] further exploited Bregman iterations to provide an efficient method to minimize convex non-differentiable functional, like TV. This avoids the need of using smooth approximations of TV. In addition, the split Bregman method solves a constrained optimization problem, which has been shown to outperform the unconstrained TV problem and avoids choosing the regularization parameter with the L-curve or similar method [55, 62]. However, the feasibility of split Bregman TV for improving image quality has not been assessed for MIT.

In this section, we compare Tikhonov and TV regularization methods and evaluate them on experimental MIT data. The TV problem is efficiently solved using the Split Bregman formulation. Methods are quantitatively evaluated on experimental phantoms in both low and high conductivity MIT settings.

Moreover, it has to be mentioned that the TV method presented in this chapter is isotropic TV, which has been introduced in Chapter 4.3.1.

5.2 Experimental setup & Data sets

Experimental data were acquired from two different MIT systems. MIT system comprises the measuring subsystem, conditioning electronics part, data acquisition & processing subsystem, and the computer used to reconstruct and process the images. Though there are some different types of MIT systems, the characteristics of their components are nearly the same to some degree. The measuring subsystem includes an array of coils placed around the measuring space. The size, number and position of the coils vary in different MIT systems. The conditioning electronics consist of amplification circuit, precision rectifier and low pass filtering. During the experimental process, two sets of measurement are acquired, background data (B) and the measuring data ($B + \Delta B$). Background data, considered as reference data, are obtained without any object in the measuring space, while measuring data are captured with the target in the measuring space. After recording these two datasets, the difference between them produces the information of the perturbation signal (ΔB). In this experimental study, two types of MIT system have been used: High and Low conductivity MIT system shown in Chapter 2.3.1(Figure 2.4) and Chapter 2.3.2 (Figure 2.6) respectively.

Seven experimental datasets were acquired with low conductivity and high conductivity MIT systems. Four sets of experimental tests were carried out for low conductivity MIT system in Figure 2.6 at a frequency of $13MHz$. The other three sets of experimental tests were carried out for high conductivity MIT system in Figure 2.4 by setting amplitude to $15V_{p-p}$ and frequency to $100kHz$. Free space measurements data were selected to be the background data.

All datasets were reconstructed using both Tikhonov and total variation regularization methods.

5.3 Results

A large number of experimental data was used to evaluate these two algorithms.

5.3.1 Low conductivity MIT

Low conductivity MIT experiments involves 28 experiments (we call them L1-L28), which includes various positioning of sample (s). And the parameters used to solve the inverse problem of this section are shown in Table 5.1.

Table 5.1 Parameters used to solve inverse problem in low conductivity MIT

Parameter	L1-L16		L17-L19		L20-L22		L23-L25		L26-L28	
	Tikh	TV	Tikh	TV	Tikh	TV	Tikh	TV	Tikh	TV
beta	$0e3$		$0e3$		$0e3$		$0e3$		$1e1$	
alpha	$1e1$		$1e2$		$1e2$		$1e2$		$1e2$	
gamma	$1e10$		$1e11$		$1e11$		$1e11$		$1e11$	
mu		$1e0$		$5e-1$		$5e-1$		$8e-1$		$1e1$
lambda		$1e1$		$1e1$		$1e1$		$1e1$		$1e1$
gamma		$1e-1$		$1e-1$		$1e-1$		$1e-1$		$1e-1$
nBreg		50		80		100		200		100

- Test 1 in low conductivity MIT

The experimental setup can be seen in Figure 5.1. The conductivity of background is 1.58 S/m and the samples tested were four insulating inclusion bottles, with diameters of 2, 6.5, 9.5 and 13 cm.

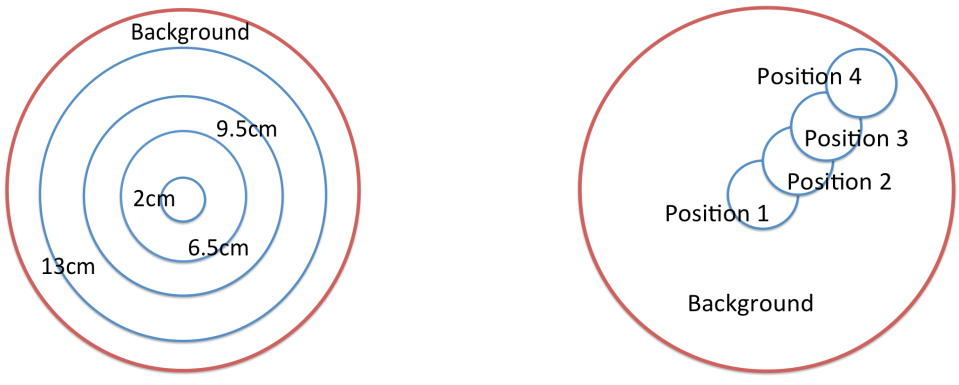

(a) Four different sizes of inclusion (b) Displacement of inclusion

Figure 5.1 The real experimental setup of Test 1

Table 5.2 show the images reconstructed by Tikhonov regularization and Total variation regularization algorithms. Reconstructed images are shown for bottles with 2, 6.5, 9.5 and 13 cm diameter (in row) and for different positions of the bottle (in column).

Table 5.2 Reconstructed images of different sizes samples in position 1,2,3,4

Diameter	Algorithm	Position 1 (L1-L4)	Position 2 (L5-L8)	Position 3 (L9-L12)	Position 4 (L13-L16)
2 cm	Tikh.	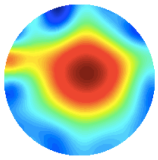	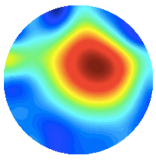	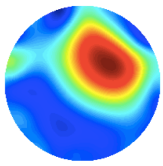	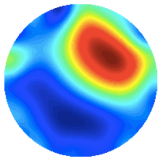
					
	TV	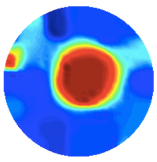	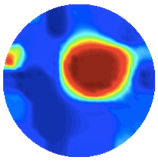	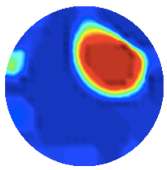	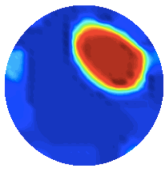
					
6.5 cm	Tikh.	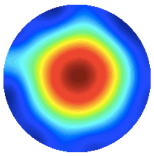	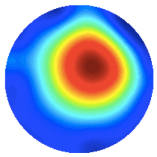	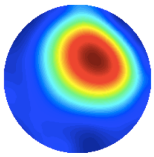	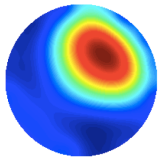
					
	TV	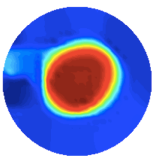	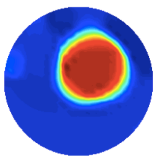	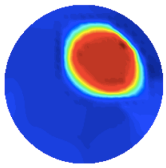	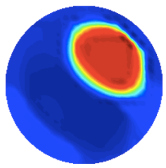
					

9.5 cm	Tikh.	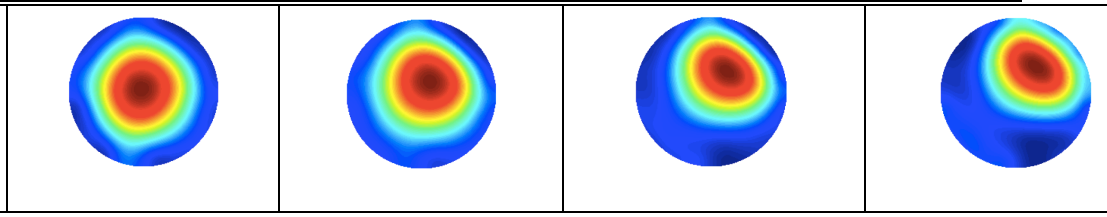			
					
	TV	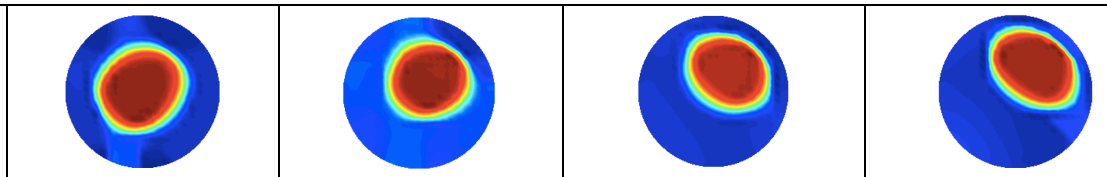			
					
13 cm	Tikh.	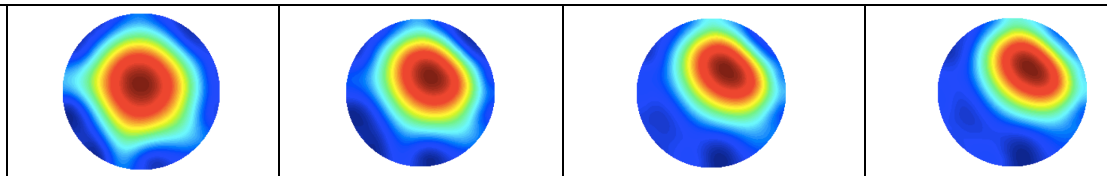			
					
	TV	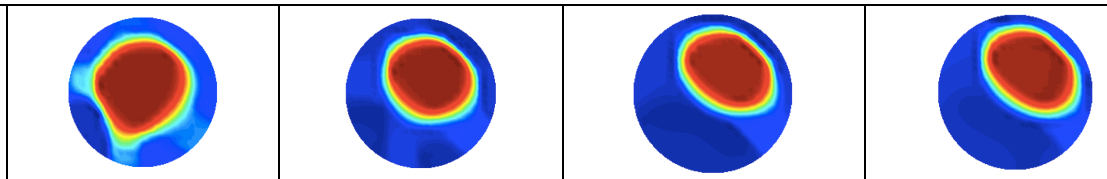			
					

- Test 2 in low conductivity MIT

The experimental setup can be seen in Figure 5.5. The samples tested were two bottles of 0.9% saline water in two different positions, while the background was free space or tap water. The conductivity of 0.9% saline water samples is 1.58 S/m and the conductivity of this tap water background is 0.06 S/m.

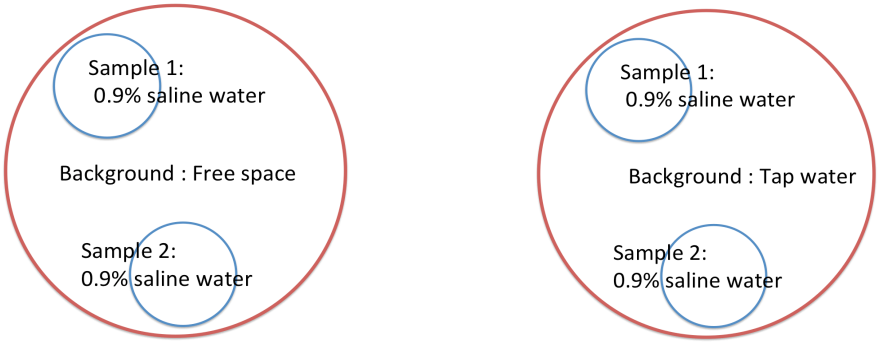

(a) Background-free space (b) Background- tap water

Figure 5.2 The real experimental setup of Test 2

Table 5.3 and 5.4 show separately the reconstructed images obtained when the background is free space and tap water. The images show reconstructions by Tikhonov regularization and Total variation regularization method for first inclusion, second inclusion and both inclusions together.

Table 5.3 Reconstructed images of two bottles saline water in free space background

	Sample 1 (L17)	Sample 2 (L18)	Sample 1+2 (L19)
Tikhonov	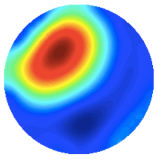	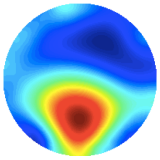	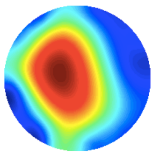
			
TV	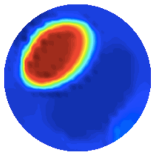	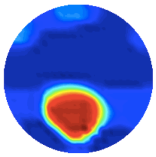	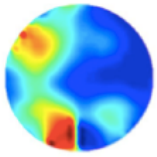
			

Table 5.4 Reconstructed images of two bottles saline water in tap water background

	Sample 1 (L20)	Sample 2 (L21)	Sample 1+2 (L22)
Tikhonov	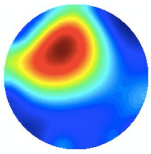	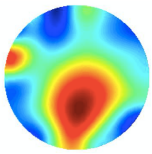	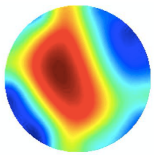
			
TV	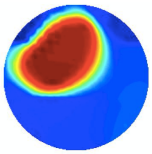	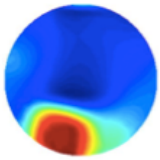	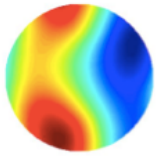
			

- Test 3 in low conductivity MIT

The experimental setup can be seen in Figure 5.3. The background was 3% saline water and the samples were three bottles of different sizes with inclusion of 0.9% saline water.

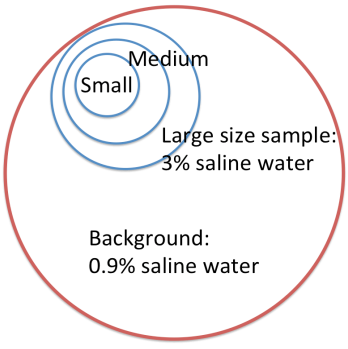

Figure 5.3 Experimental setup of Test 3

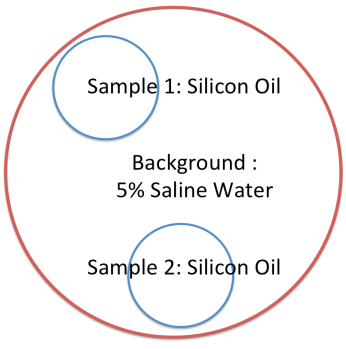

Figure 5.4 Experimental setup of Test 4

Table 5.5 shows the reconstruction images for Tikhonov regularization and Total variation regularization method for small, medium and large size of inclusion.

Table 5.5 Reconstructed images of three different sizes samples in 0.9% saline water background

	Small size (L23)	Medium size (L24)	Large size (L25)
Tikhonov	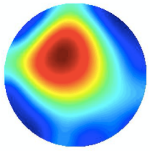	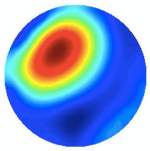	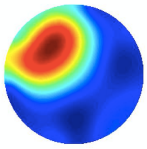
			
TV	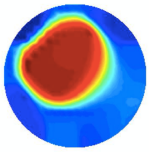	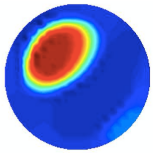	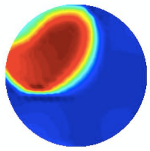
			

- Test 4 in low conductivity MIT

The experimental setup can be seen in Figure 5.4. The samples tested were two bottles of silicon oil working as non-conductive inclusions and 5% saline water considered as conductive background.

Table 5.6 shows the reconstruction images obtained by Tikhonov regularization and Total variation regularization methods, where columns correspond to one silicon oil inclusions, silicon oil inclusion at a different position and two silicon oils inclusions together.

Table 5.6 Reconstructed images of two bottles of silicon oil in 5% saline water

	Sample 1 (L26)	Sample 2 (L27)	Sample 1+2 (L28)
Tikhonov	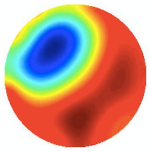	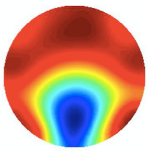	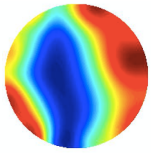
			
TV	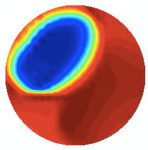	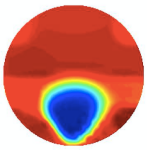	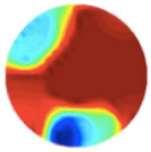
			

- Low conductivity MIT results analysis and discussions

It can be seen from imaging results of low conductivity that TV can produce higher quality images. To further demonstrate this, the image quality measures are used to quantitatively show comparison between TV and Tikhonov based algorithms. In this case shape deformation (SD), resolution (RES) and amplitude ration (AR) was selected from GREIT image quality parameters [63]. SD shows part of reconstructed images (after some theresholding) that does not fit in a circular shape. For higher quality reconstruction SD should be low and uniform for the same sample size and shape. Resolution (RES) measures the size of reconstructed inclusion as a fraction of size of entire imaging region; this is equivalent to a measure of point spread function (PSF) size. RES should be uniform and small, in order to more accurately represent shape of the inclusion based on their conductivity values. AR measures the ratio of image pixel amplitudes in the inclusion area to that in the reconstructed image. A uniform and smaller AR is a measure of higher quality image. GREIT parameters are widely used for image

quantification and quality measures, we refer to [63] for more detailed descriptions.

Figure 5.5 show SD, RES, and AR, for low conductivity experiments from L1-L28. Apart from very few points in SD, the TV are universally outperforming the Tikhonov algorithm in terms of all image quality measures. The fact that the neighboring measurements were excluded in low conductivity MIT system, this sometimes create some deformation in shape of inclusions as this act as missing data MIT, this is perhaps responsible for larger numbers for SD, and size dependent SD in both algorithms.

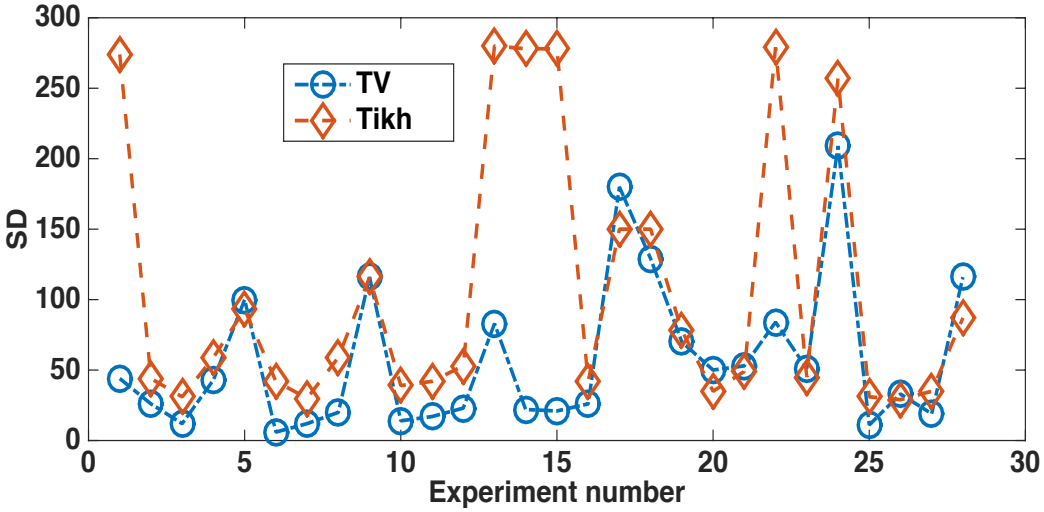

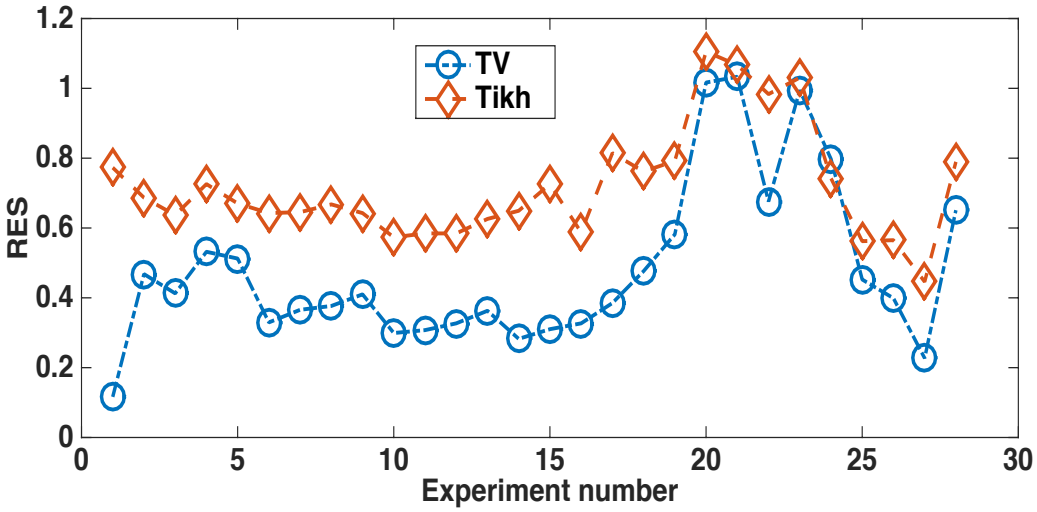

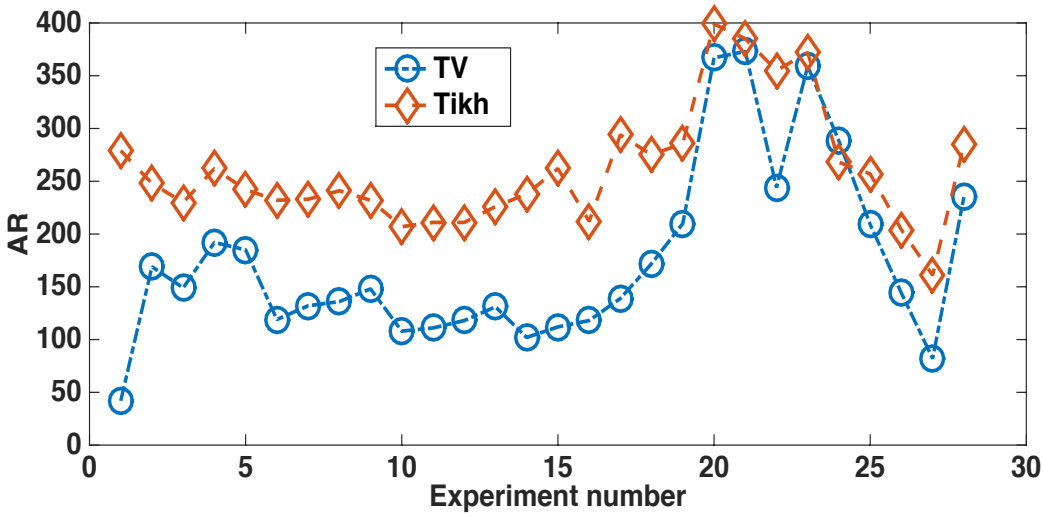

Figure 5.5 Figures of merit for experiments L1-L28

5.3.2 High conductivity MIT

High conductivity MIT experiments involves 9 experiments (we call them H1-H9), which includes various positioning of metallic sample (s). And the parameters used to solve the inverse problem of this section are shown in Table 5.7.

Table 5.7 Parameters used to solve inverse problem in high conductivity MIT

Parameter	H1-H2		H3-H6		H7-H9	
	Tikh	TV	Tikh	TV	Tikh	TV
a1	$1e-8$		$1e-7$		$1e-7$	
a2	$1e3$		$1e3$		$1e3$	
mu		$1e0$		$2e-1$		$2e-1$
lambda		$1e0$		$1e-2$		$1e-2$
gamma		$1e-2$		$1e-1$		$1e-1$
nBreg		200		200		200

- Test 5 in high conductivity MIT

The sample tested in Test 5 was a rectangular aluminum object, and the experimental setup is shown in Figure 5.6.

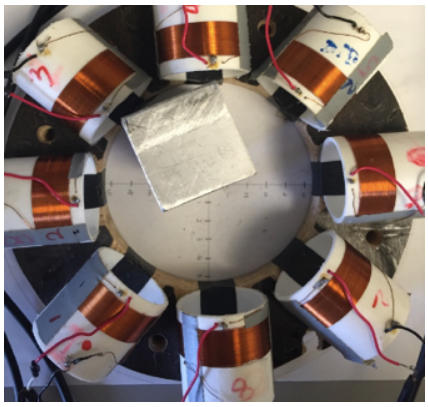

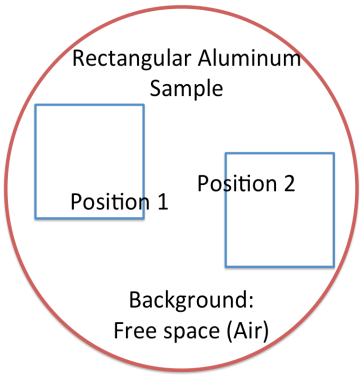

(a) Real conductive distribution in position 1 (b) Rectangular aluminium sample in position 1 or 2

Figure 5.6 Experimental setup of Test 5

Table 5.8 shows the images reconstructed using Tikhonov and Total variation regularization methods for two positions of the steel sample.

Table 5.8 Reconstructed images of a rectangular aluminum sample in position 1 and 2

	Position 1 (H1)	Position 2 (H2)
Tikhonov	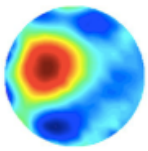	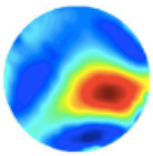
		
TV	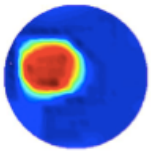	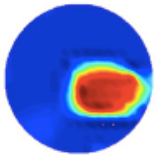
		

- Test 6 in high conductivity MIT

Test 6 is a circular aluminum sample placed in four different positions and the experimental setup is shown in Figure 5.7.

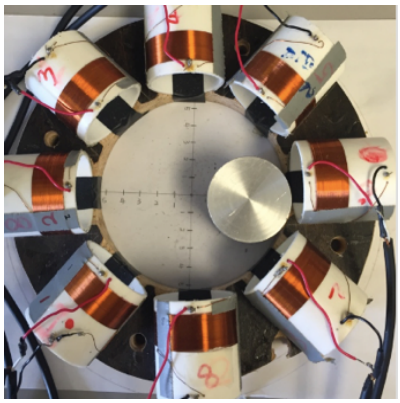

(a) Real conductive distribution in position 1

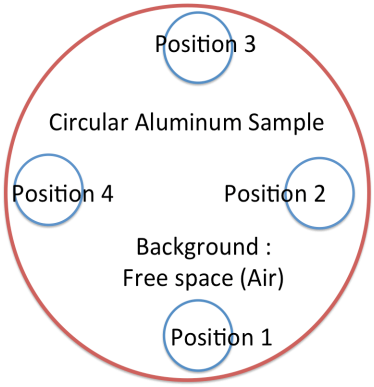

(b) Circular aluminum sample in position 1,2,3,4

Figure 5.7 Experimental setup of Test 6

Table 5.9 shows the reconstruction images obtained by this test. The images correspond to reconstructions by Tikhonov and Total variation regularization algorithm for four different positions of the sample.

Table 5.9 The images of a circular aluminum sample in four different positions

	Position 1 (H3)	Position 2 (H4)	Position 3 (H5)	Position 4 (H6)
Tikhonov	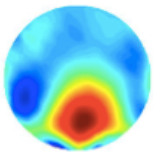	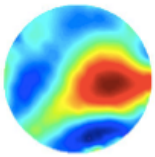	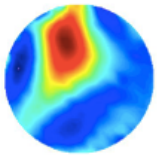	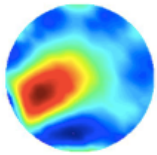
				
TV	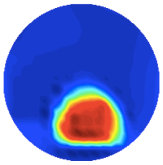	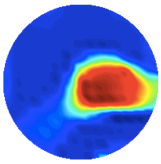	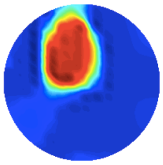	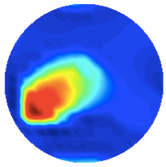
				

- Test 7 in high conductivity MIT

Test 7 used two circular aluminum samples placed in different positions separately (shown in Figure 5.8).

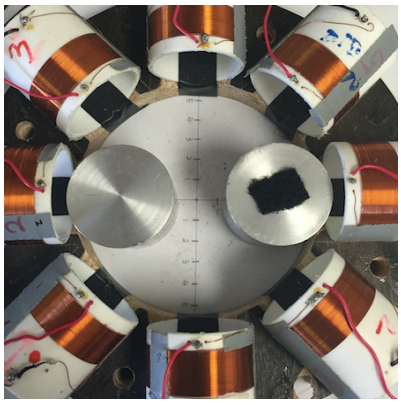

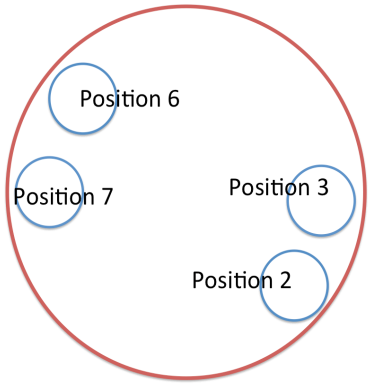

(a) Real conductive distribution of two samples (b) Two samples in different positions separately

Figure 5.8 Experimental setup of Test 7

Table 5.10 shows the reconstructed images obtained after this test by Tikhonov and Total variation algorithms, for two circular aluminum samples in different positions separately.

Table 5.10 Reconstructed images of two circular aluminum samples in different positions

	Position 3& 7 (H7)	Position 2 & 7 (H8)	Position 2 & 6 (H9)
Tikhonov	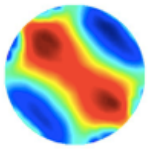	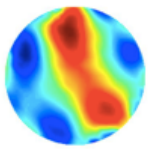	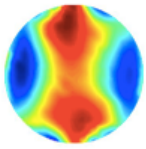
			
TV	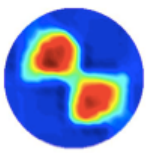	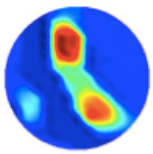	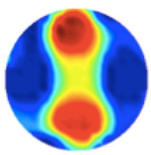
			

- High conductivity MIT results analysis and discussions

It can be seen from imaging results of high conductivity samples that TV can produce higher quality images. To further demonstrate this, the image quality measures, as it has been mentioned in low conductivity MIT results subsection, are used to quantitatively show comparison between TV and Tikhonov based algorithms. Figure 5.9 show SD, RES and AR for 8 experiments in high conductivity objects. Apart from SD for experiment H9, in all other examples the TV shows better performance compared to standard Tikhonov method.

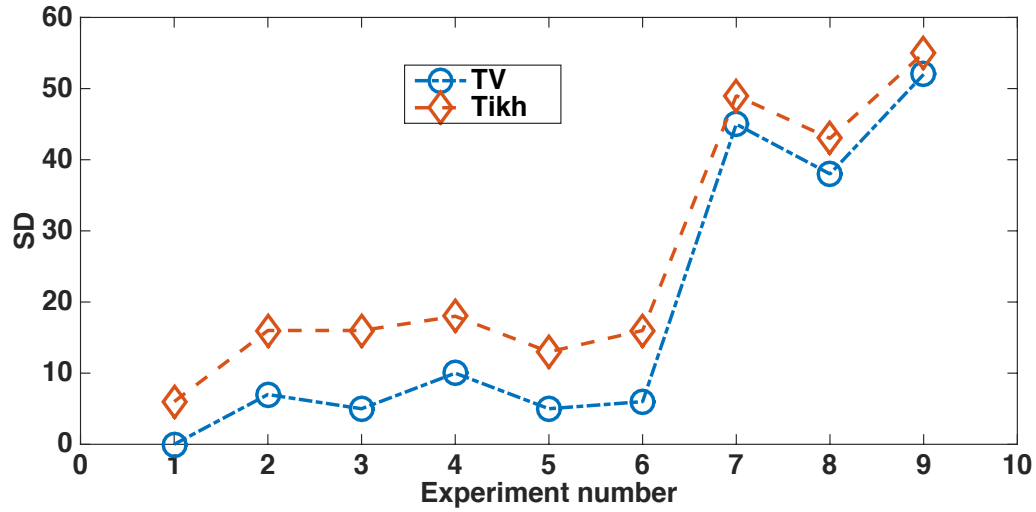

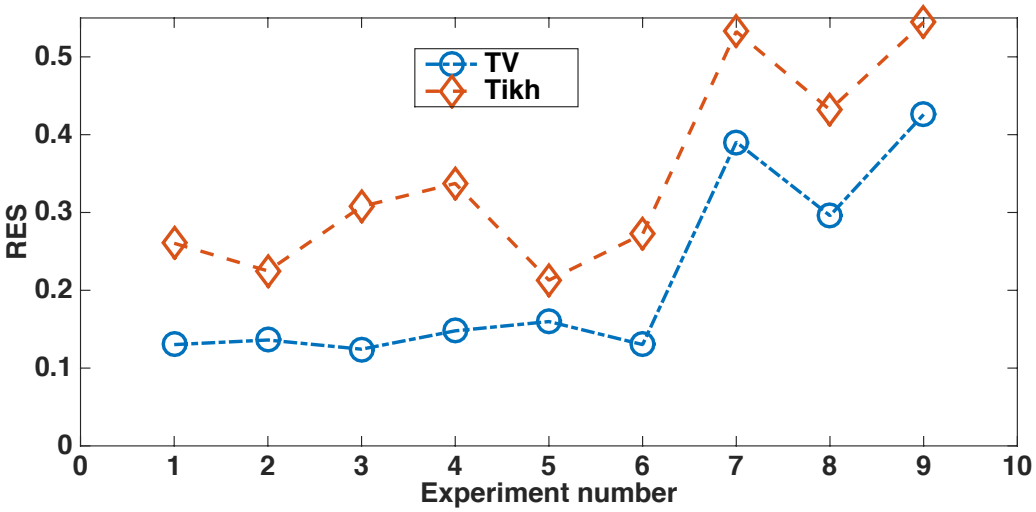

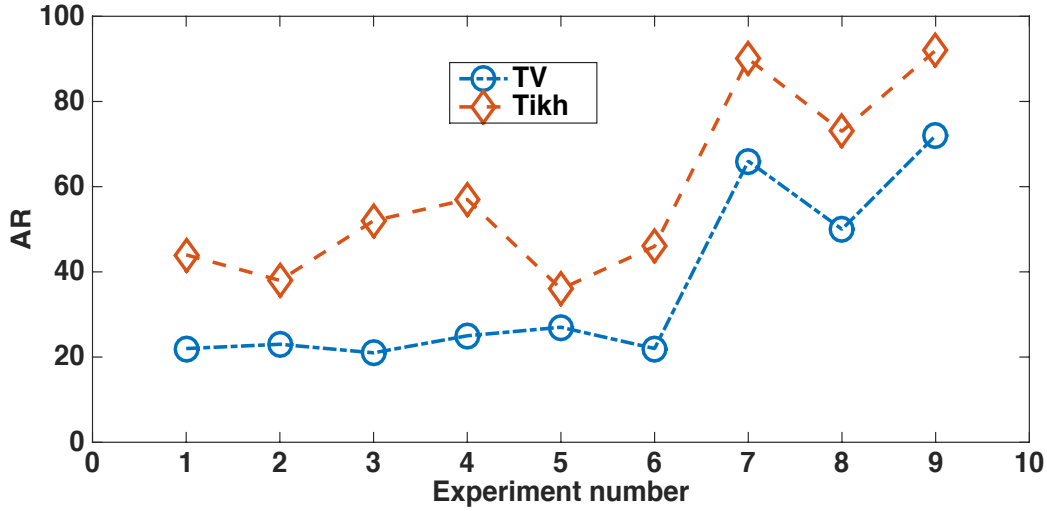

Figure 5.9 Figures of merit for experiments H1-H9

5.4 Conclusions

The total variation method produced reconstructed images with improved quality for both low conductivity and high conductivity MIT systems. As it can be seen from the results, the differences in the dimension and position of the objects cannot be distinguished from the reconstructed images obtained by Tikhonov regularization method but total variation lead to improved recovery of the size and shape of the target and in particular sharper boundaries between different conductivity regions.

Previous work for MIT has used Tikhonov method for conductivity flow imaging [51], which evaluated several saline solutions with different dimensions/conductivity values in a low conductivity MIT system. The results presented in [51] showed that the reconstructed images are smooth enough but in the case of testing two or more objects simultaneously, the reconstruction could not reliably recover conductivity contrasts and imaging resolution. However, according to our experimental results, total variation method improved conductivity contrast in all these images. Moreover, in this work, we have proposed and validate the use of the split Bregman method for minimizing the TV problem in MIT and have compared it to

Tikhonov method. Previous studies have shown that Bregman iteration methods for TV correct some of the deficiencies of standard TV and lead to improve results [52, 55, 60]. A comparison between standard TV and Bregman-based TV methods in MIT will be considered in further work.

It is common practice in MIT to use linear for experimental difference data, which is more robust and less sensitive to the effect of modeling error and noise in measured data. The proposed been validated using experimental data covering a wide range of scenarios, with different size and location of inclusions. However, the validation has focused on 2D, so further studies need to be done to address the 3D inverse problem. Besides, due to the nature of eddy currents, the MIT forward problem is a large-scale problem, which will increase the demand of computational resources. Extension to nonlinear with experimental data and absolute imaging is still remaining a challenging, partly due to lack of good experimental data and matching with the forward models.

Overall, image quality parameters show consistency good performances in both low and high conductivity case, but as expected metallic MIT tests shows more robust imaging results. Some experiments in low conductivity case present more challenges dues to low conductivity contrasts between background and inclusions. In these cases, TV performed well enough to recover images that not recovered well by Tikhonov algorithm.

A TV method based on the Split Bregman formulation, is presented and validated experimental MIT data. Quantitative image quality analysis shows significant improvement of image qualities by using proposed TV algorithm. In experimental work presented here the total variation algorithm produced high quality images, making it a suitable candidate for image reconstruction in both metallic imaging and low conductivity MIT imaging. It is anticipated that the high-quality images that can be obtained using TV algorithm, can help stimulate new applications for MIT in near surface depth detection or in plastic Landmine detection.

CHAPTER 6 TV REGULARIZATION ON PLANAR MIT

MIT is a tomographic imaging technique with a wide range of potential industrial applications. Planar array MIT is a convenient set-up but remains very challenging given the limited data. This study assesses the use of sparse regularization methods for accurate position and depth detection in planar array MIT. The most difficult challenges in MIT are to solve the inverse and forward problems. The inversion of planar MIT is severely ill-posed due to limited access data. Thus, this chapter posed a total variation problem and solved it efficiently with the Split Bregman formulation to overcome this difficulty. Both isotropic and anisotropic total variation formulations are compared to Tikhonov regularization with experimental MIT data. Results show that Tikhonov method failed or underestimated the object position and depth. Total variation led to accurate recovery of depth and position. There are numerous potential applications for planar array MIT where access to the materials under testing is restrict. Sparse regularization methods are a promising approach to improving depth detection for limited MIT data.

6.1 Introduction

MIT is aiming at visualizing the conductivity distribution of the test sample, which can be achieved by solving the forward and inverse problem. The forward problem can be easily elucidated by eddy current model while regularization is required to solve the inverse problem due to its ill-posed nature. Tikhonov regularization is the tradition and most widely used regularization method in MIT system but leads to suboptimal results. A better choice is to use total variation (TV) functional that can improve the reconstructed image quality over Tikhonov regularization. Total variation allows to regularize the inverse problem by removing noise while preserving edges in the reconstructed images. However, TV functional is non-

differentiable, so it is usually approximated. These approximations may be non-optimal or lead to slow convergence. In addition, TV may lead to a loss of contrast. The use of the Bregman distance has been proposed to solve these issues [64]. In particular, the split Bregman method solves efficiently L1-regularized problems such as the total variation and has been widely applied to different applications [52, 53, 55, 62, 65]. A recent study [66] proposed the use of TV functional to improve the reconstructed image quality over Tikhonov regularization on MIT experimental data.

The TV problem first proposed in [67] for noise removal was based on the isotropic formulation of TV. Anisotropic TV has been suggested in different applications [68-70]. Anisotropic diffusion regularization was investigated in [71] for fluorescence diffuse optical tomography. For efficient noise removal, isotropic and anisotropic TV can outperform each other depending on the application. Isotropic TV prefers images with smooth boundaries while anisotropic TV preserves and recovers the image edges [72, 73]. In this paper, Isotropic TV and Anisotropic TV are implemented in planar sensor array MIT for position detection and depth detection.

MIT can be divided into different types of systems based on its spatial arrangements of coils, i.e., traditional circular array MIT and planar array MIT. The measured region of traditional circular array MIT system can access freely around the entire periphery. As such, many previous researches indicate the capability of circular array MIT system where the object space has circular geometry and free access. However, there are plenty of situations where the access is restricted that non-destructive measurements cannot be collected from the complete periphery but only one surface [22]. The test space of the system proposed in this paper is perpendicular to the sensors in order to overcome these difficulties and the resulting application of this technique has increased considerably. Since that, a series of studies based on planar system have been recently implemented. The feasibility of planar type coil used for evaluating near-surface material properties was investigated in [74]. In [75] authors investigated the possibility of inspection of electroplated materials using planar meander and mesh type magnetic sensor. The planar MIT system for the detection of faults on thin metallic plates was

presented in [76], which shows 2D imaging results underneath the sensor array. The work in [77] explored the feasibility of planar MIT system for 3D near subsurface imaging through simulation results and experimental evaluations. From the previous observations, planar array MIT system shows significant challenge in terms of depth detection over traditional circular array system. The development and set up of the proposed planar array MIT system are presented in this paper, followed by the experimental results of position and depth detection.

In this work, the capabilities of proposed planar array MIT system with TV regularization methods for position and depth detection are evaluated by experimental data. Results in this study support that the planar MIT system with the aid of TV regularization would receive considerable attention in subsurface imaging area.

6.2 Experimental Results

The system used in this chapter is 9-coils planar sensor array MIT system introduced in Chapter 2.3.1.

6.2.1 Planar array MIT System description

The picture of planar MIT system described in this paper is shown in Figure 2.5. It consists of the following components, includes: a host computer, a digital function generator (Topward 8112), a National Instrument based data acquisition system (NI USB-6259), a channel switching board (ADG406 multiplexers), and a sensor array containing 9 equally spaced inductive coils.

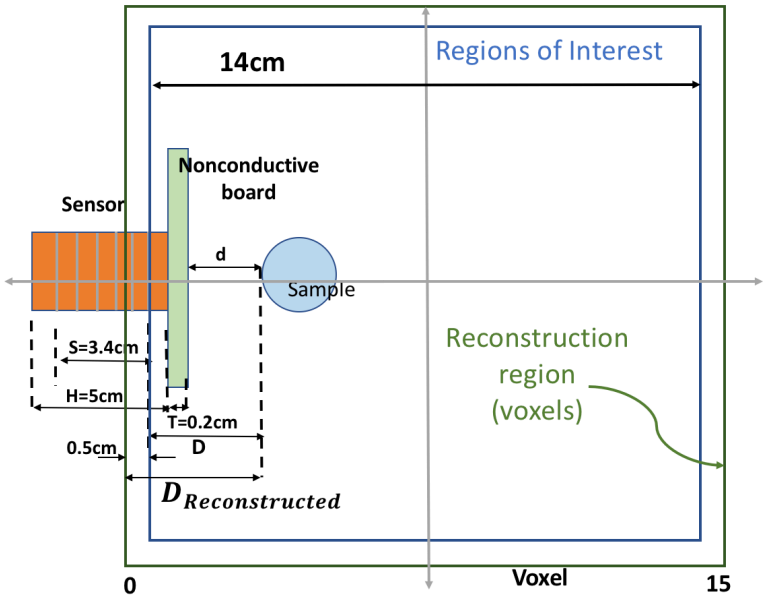

Figure 6.1 Simplified top view of the system

The digital function generator supplies an 80kHz, 15V peak-peak sinusoidal signal to each of the 9 inductive coils individually. The ADG406 multiplexers can accomplish the channel switching process while a NI USB-6259 is connected between a host PC and the multiplexer to do the image reconstruction. All the measurements are averaged three times before displayed. The planar sensor array consists of 9 cylindrical coils, which is arranged in a 3×3 matrix form and located on a non-conductive square board. The parameters of the sensor model are showed in Table 6.1. Figure 3.6 indicates the sequence and the dimensions of the coils. The data collection pattern of this system can be described as the following sequence: 1-2,1-3…1-9, 2-3…2-8… 8-9, providing $9 \times 8/2 = 36$ independent measurements that are imported into image reconstruction system.

As it mentioned before, finite element method (FEM) has been applied in this dissertation. The information of the mesh been used, and the implementation process of the proposed experiments are shown in Figure 6.2. Moreover, the average total variation reconstruction time is 20 seconds, which is a bit longer than Tikhonov method (2 seconds).

Table 6.1 Parameters of the sensors model

Number of coils	9
Number of turns	100
Self-inductance (μH)	380
Coil height (cm) (H)	5
Coil side length (cm) (S)	3.4
Outer diameter (cm)	4.1
Inner diameter (cm)	3.9
Surface area of the board (cm^2)	14×14
Thickness of the board (cm) (T)	0.2

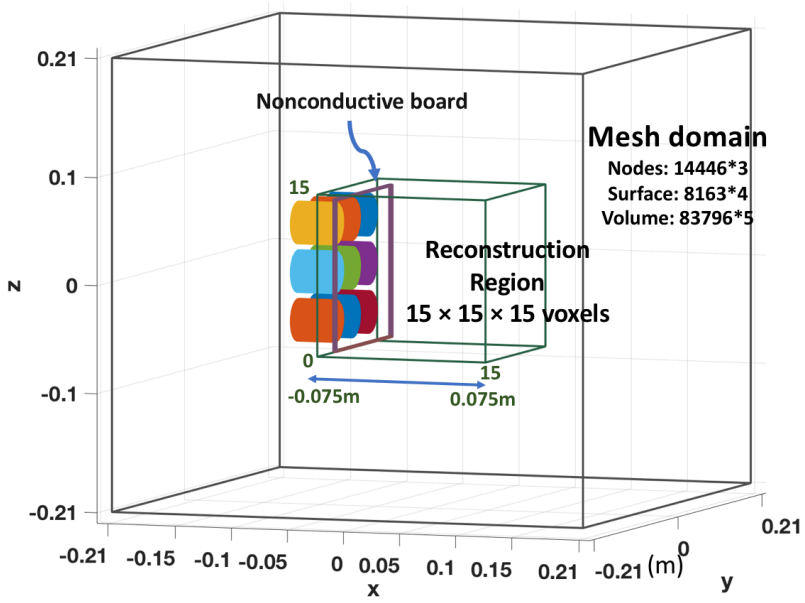

Figure 6.2 Implementation process of all proposed experiments

All the parameter values were used to solve the inverse problem of the following research are shown in Table 6.2.

Table 6.2 Parameter values used to solve the inverse problem

Parameter	Position detection		Depth detection		
	Tikh	Iso	Tikh	Iso	Ani
a1	$1e-10$		$1e-10$		
a2	$1e3$		$1e3$		
mu		$2e-1$		$2e-1$	$5e-1$
lambda		$1e-2$		$1e-2$	$1e-3$
gamma		$1e-1$		$1e-1$	$1e-2$
thresholding	0.5	0.5	0.5	0.5	0.5

6.2.2 Position detection using Isotropic TV

In this section, we investigate the capability of planar array MIT system for position detection in terms of a set of experiments. Aluminum rods are used as tested samples and Table 6.3 shows the parameters of these rods. The aluminum rods are placed in different positions but with the same distance to the sensors, which can be calculated from Figure 6.1 as $D = T + (H - S)/2 + d = 1\ cm$.

Table 6.3 Parameters of testing rods

Radius of the rods (cm)	2
Height of the rods (cm)	5
Relative permeability	1
Electrical conductivity (S/m)	3.5×10^7
Distance to the sensor (cm)	1

Two sets of experiments are implemented in this section: single and multiple samples. Moreover, the isotropic TV and Tikhonov regularization method are both used to be the inverse solver for producing reconstructing images respectively. One of the experimental setups is

shown in Figure 6.3 as one simulated image of inclusion indicated in Figure 6.4.

Figure 6.3 Experimental setup: sample close to coil1

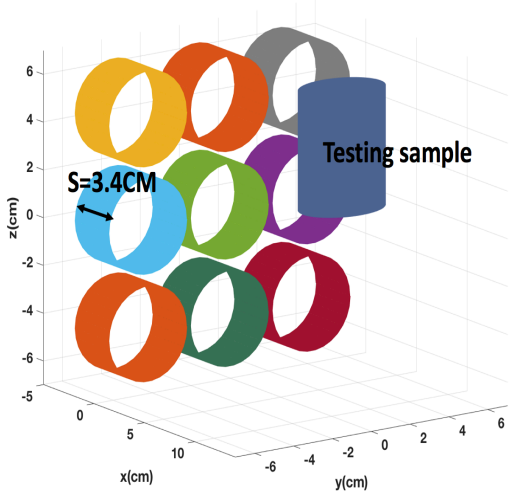

Figure 6.4 Simulated image of inclusion: sample close to coil1

Figure 6.5 indicates the slice images obtained when a single rod is placed in different positions. The images above the sliced images are simulated images of inclusions. The sliced images obtained by Isotropic TV, indicate the exact positions of test sample that can be acquired from the simulated images of inclusions, which verify the position detectability of planar sensor array MIT system. Figure 6.6 shows the image results when the tested samples are two aluminum rods. As shown on the sliced images, planar MIT system can also detect multiple samples with much clearer results from Isotropic TV method.

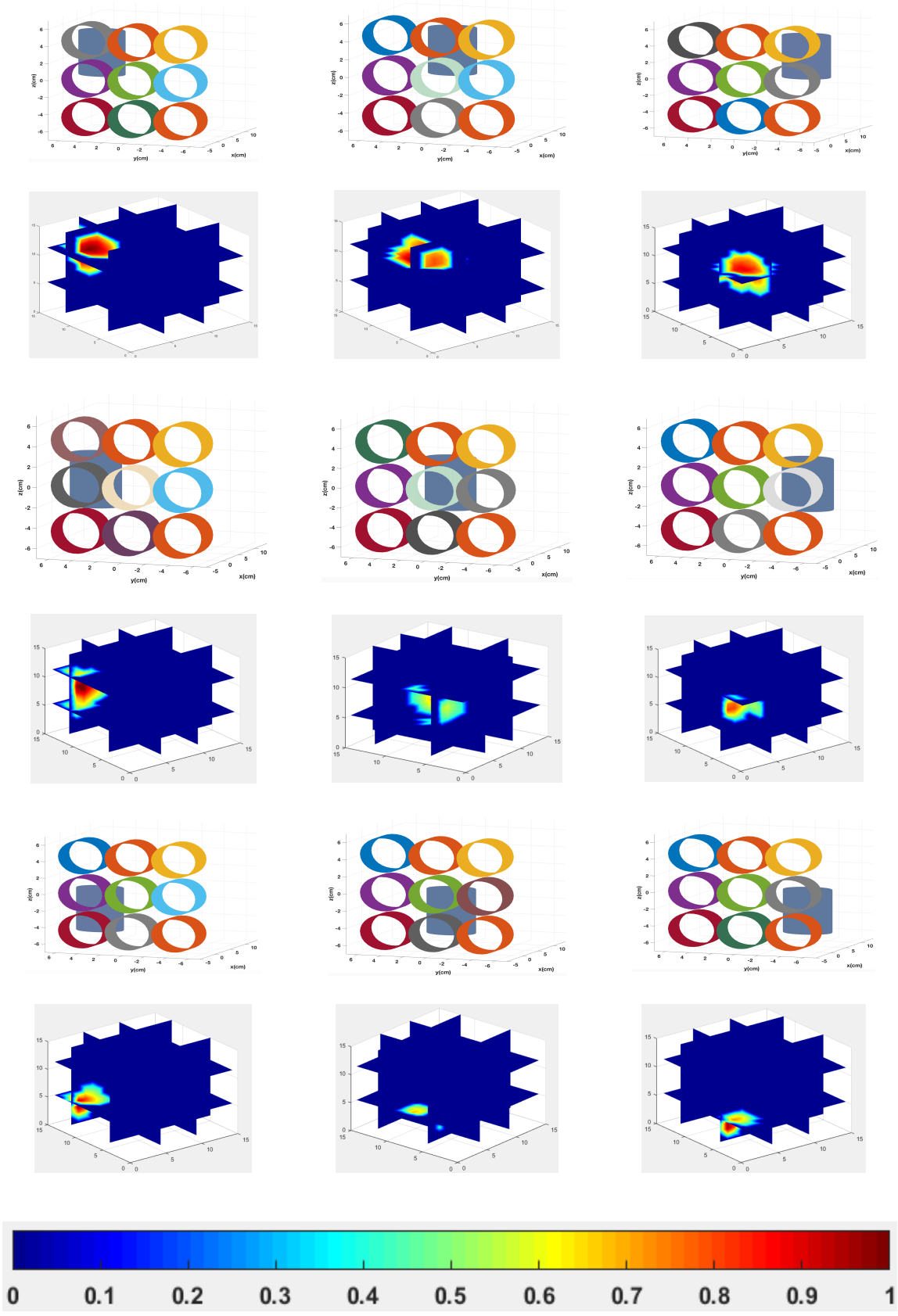

Figure 6.5 Position detection of planar MIT using experimental data (single rod) obtained by TV algorithm

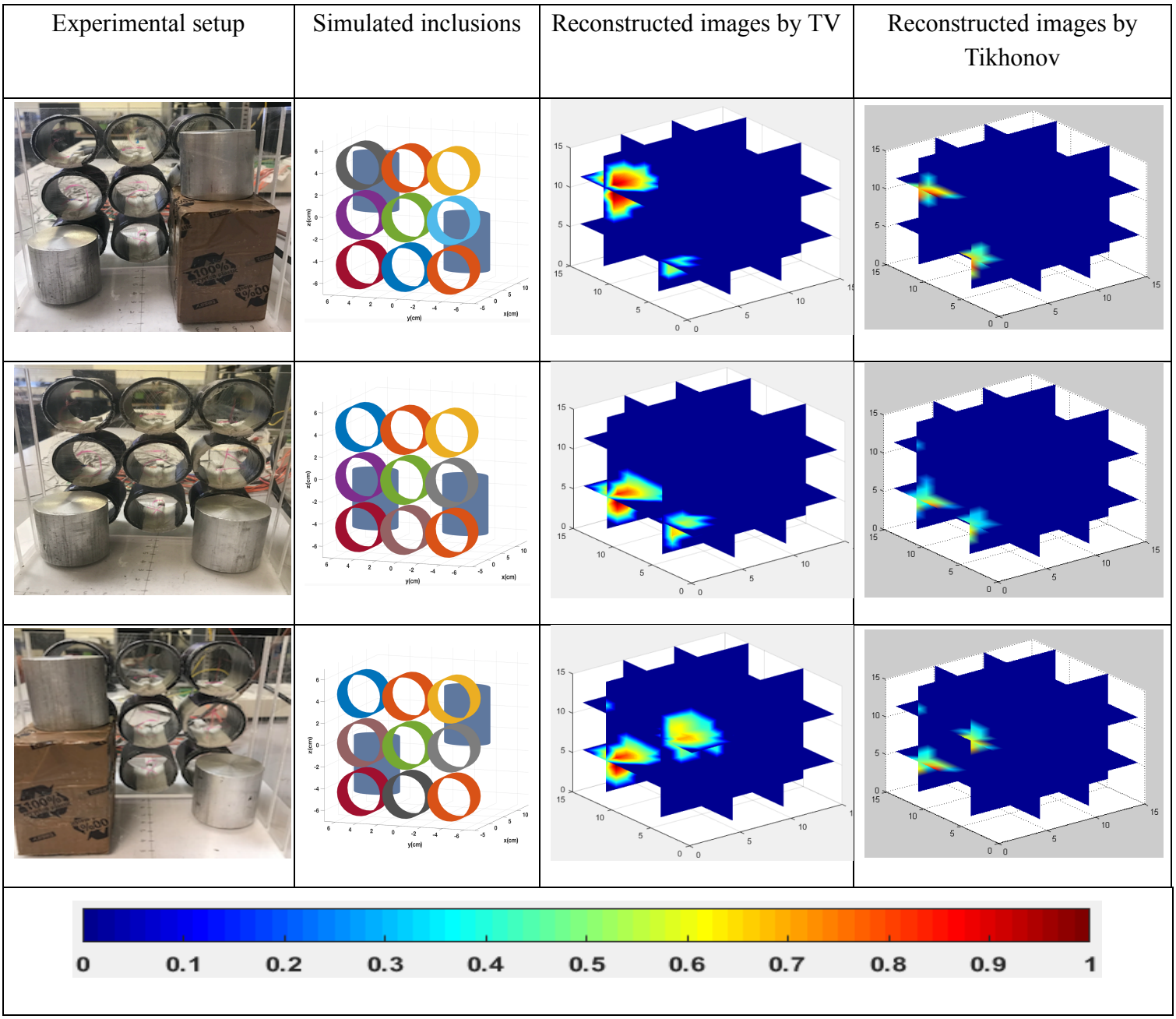

Figure 6.6 Position detection of planar MIT system using experimental data (multiple rods) obtained by Isotropic TV and Tikhonov regularization method

6.2.3 Depth analysis based on Isotropic TV, Anisotropic TV and Tikhonov regularization

It has been shown in the previous section that planar array MIT system can detect the objects when they are very close to the sensors. However, to assess the suitability of planar MIT for

subsurface imaging we must assess how deep it can detect an object. Therefore, planar MIT with TV regularization is evaluated on different depth detections compared to Tikhonov regularization. The tested sample is the same as the one used in the previous section. The reconstructed images below are obtained by isotropic TV, anisotropic TV and Tikhonov regularization method. An example of experimental setup and simulated image of inclusion are displayed in Figure 6.7 and Figure 6.8, respectively.

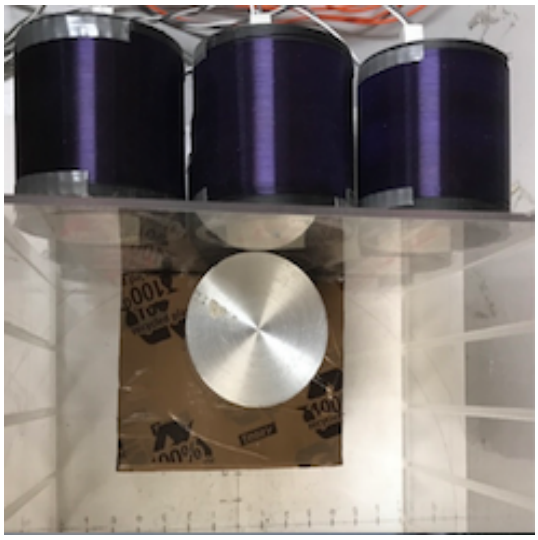

Figure 6.7 Experimental setup (D=1cm)

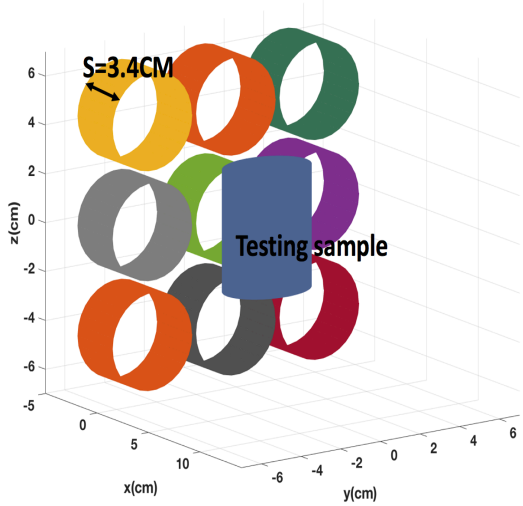

Figure 6.8 Simulated image of inclusion (D=1cm)

Figure 6.9 indicates the true experimental setup and reconstructed images using one aluminum rod moving from $D = 1\ cm$ to $D = 5\ cm$. The results include both reconstructed images obtained by isotropic TV, anisotropic TV and Tikhonov regularization methods. The voxel size is $1cm \times 1cm \times 1cm$. Results show that TV regularization is sensitive to the depths of sample in accordance with real experimental setup and demonstrate a limit detectability distance of $5\ cm$. On the contrary, the true depth information cannot be extracted from the reconstructed images obtained using Tikhonov regularization. Isotropic and anisotropic TV methods produced similar results, even reconstructed images obtained by anisotropic TV seem slightly better. This might be because a coarse mesh has been used.

Simulated inclusions	Anisotropic TV	Isotropic TV	Tikhonov regularization
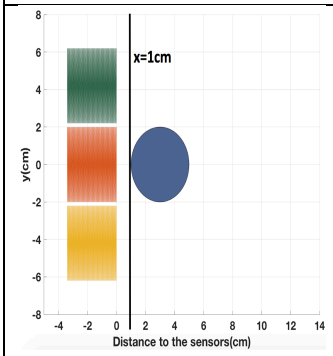	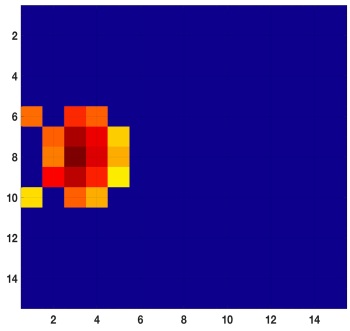 $D_{Reconstructed} = 1.5cm$	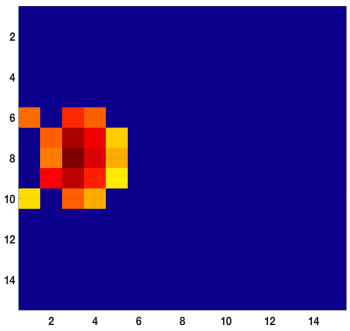 $D_{Reconstructed} = 1.5cm$	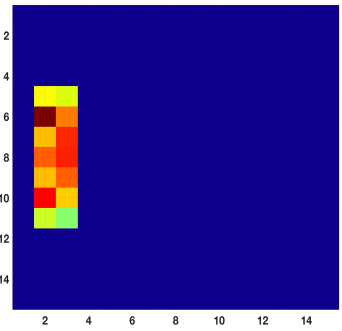 $D_{Reconstructed} = 1.5cm$
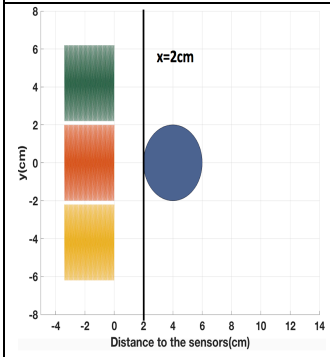	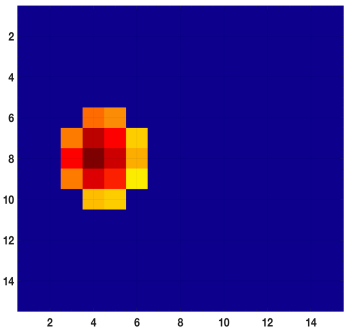 $D_{Reconstructed} = 2.5cm$	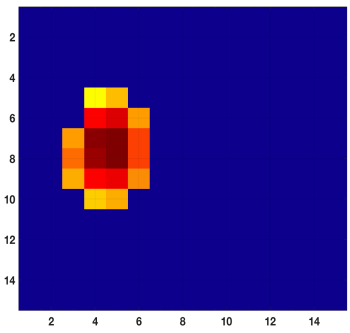 $D_{Reconstructed} = 2.5cm$	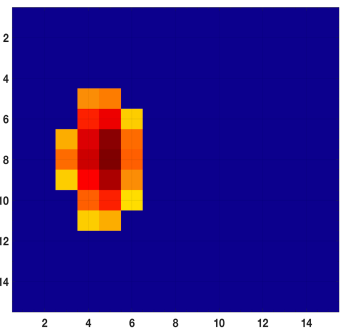 $D_{Reconstructed} = 2.5cm$
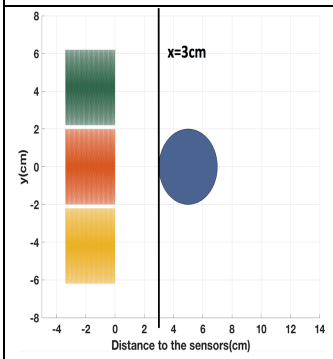	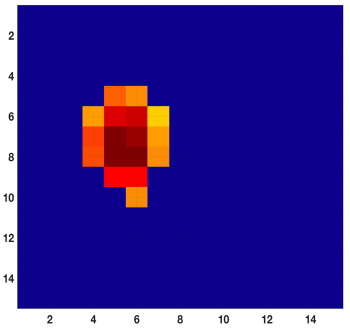 $D_{Reconstructed} = 3.5cm$	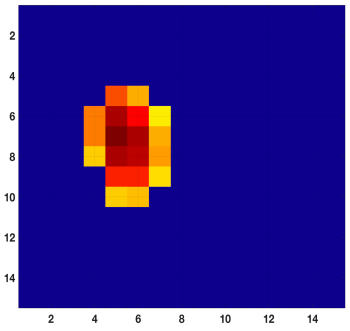 $D_{Reconstructed} = 3.5cm$	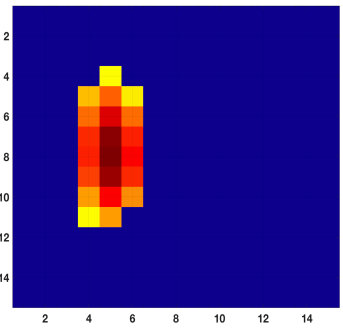 $D_{Reconstructed} = 3.5cm$
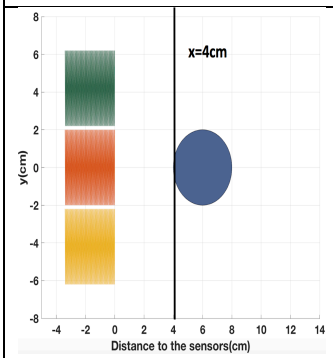	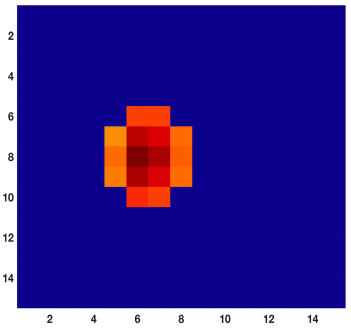	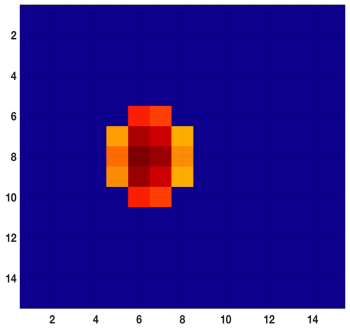	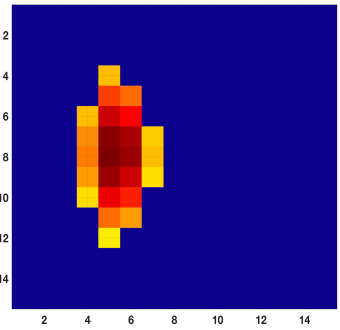

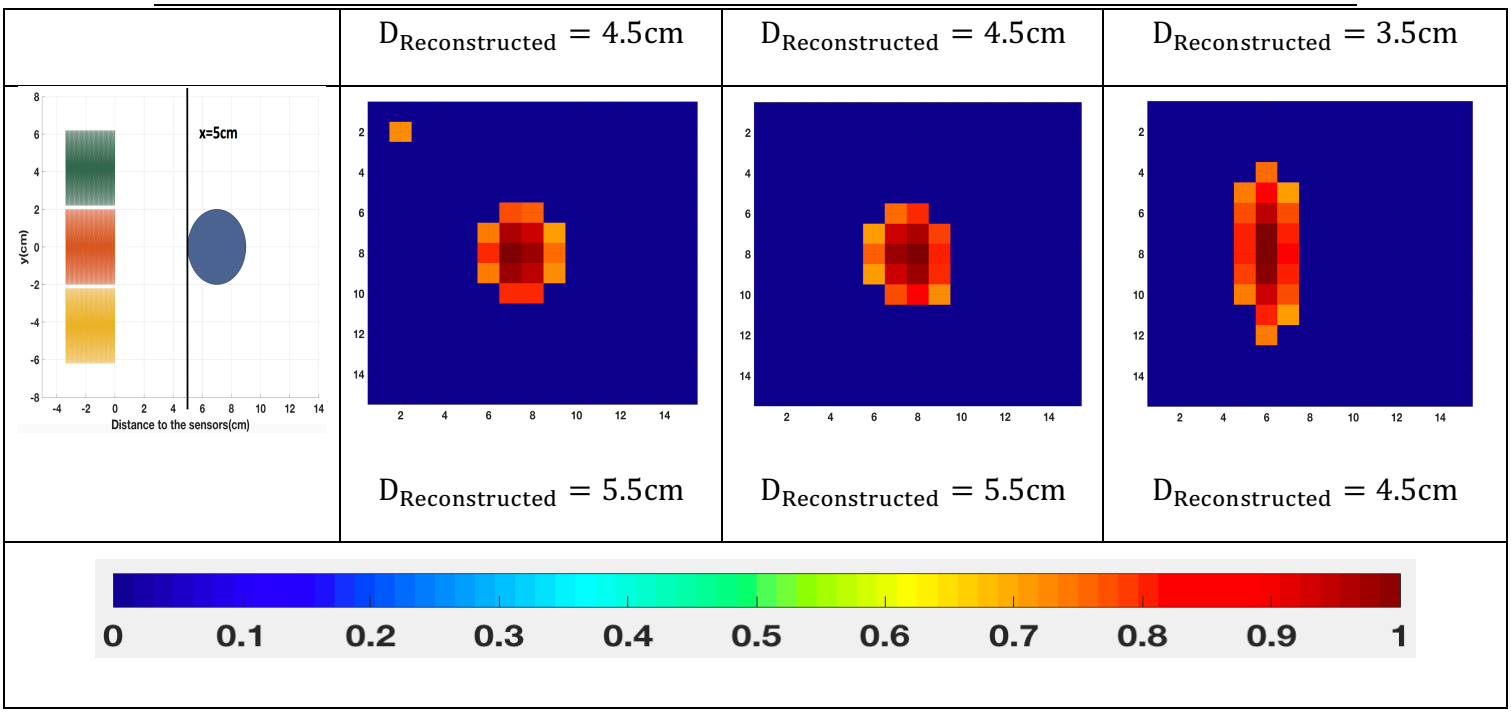

Figure 6.9 Depth detection of planar array MIT system using the experimental data (one rod) obtained by isotropic TV, anisotropic TV and Tikhonov regularization methods

6.3 Results analysis and discussion

Here we introduced the percentage depth sensitivity (PDS) to indicate the performance of planar MIT system for depth detection:

$$PDS = \frac{(maximum\ detectable\ depth)}{(side\ length\ of\ non-conductive\ square\ board)} \times 100\%$$

The surface area of the square board can be assumed to represent the area of planar array sensors arranged for MIT system. A previous work on planar MIT system [77], which introduced a 16-channels planar MIT with a $18 \times 18cm^2$ square board, could detect a maximum depth of $4cm$, and presented PDS that can be estimated as ${}^{4}/_{18} \times 100\% = 22.2\%$. In our experimental study, the maximum depth that could be detected is $5cm$, which corresponds to PDS of ${}^{5}/_{14} \times 100\% = 35.7\%$. This verifies that our framework has a better depth detectability than previous methods.

.

It can be observed from the experimental results in Figure 6.5 and Figure 6.6 that planar array MIT system can detect the positions of single and multiple conductive samples with the aid of total variation regularization algorithm. Figure 6.9 shows that TV helps to provide more precise images than Tikhonov regularization, enhancing depth detectability of planar MIT. To demonstrate these, three groups of analysis works are conducted below.

The absolute value of the difference between experimental and background induced voltage can be used to determine the sensitivity of the system and so to analyze the depth detection of planar MIT system. Also, this norm of difference is divided by the norm of background data. The system becomes less sensitive as the norm value decreases. Figure 6.10 shows norm values of 6 experimental measurements conducted in depth detection part. As it shown in Figure 6.10, a significant decline in norm value of experimental data can be observed. But the norm value will increase when the distance exceeds the limit depth of $5cm$ due to the noises or the less sensitive of system. Obviously, the sensitivity and accuracy of the system degrades as the depth increases.

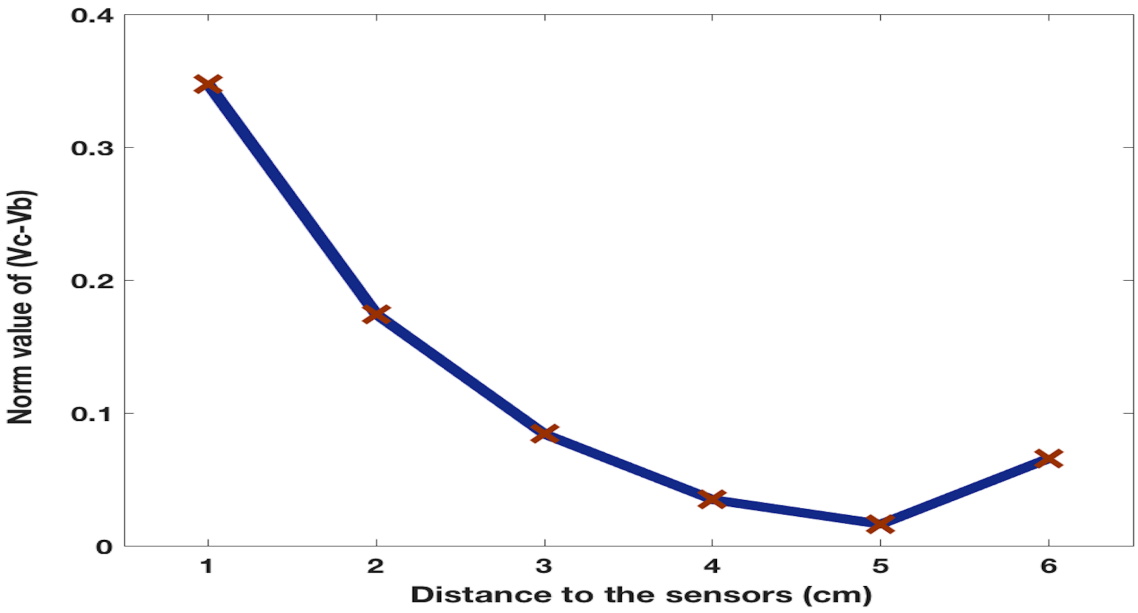

Figure 6.10 The norm value of the difference between experimental and background induced voltage

As it can be obtained from results in depth detection, reconstructed images produced by TV regularization have higher image qualities than Tikhonov regularization. Figure 6.1 indicates that the experimental distance can be obtained from the distance shown in reconstructed image as following: $D = D_{Reconstructed} - 0.5$. Then, $D_{Reconstructed}$ can be read from the reconstructed images and the voxel size is $1cm \times 1cm \times 1cm$. Therefore, the distance between the object and the planar sensors can be concisely and explicitly calculated from the reconstructed images in Figure 6.9. Figure 6.11 shows the graph of experimental distances of isotropic TV, anisotropic TV and Tikhonov versus real distances. Moreover, Table 6.4 explicitly lists the numerical values of experimental distance and the accuracy of depth acknowledged by isotropic TV, anisotropic TV and Tikhonov. Evidentially, the accuracy of the system for depth detection is slightly better with isotropic TV and anisotropic TV than with Tikhonov.

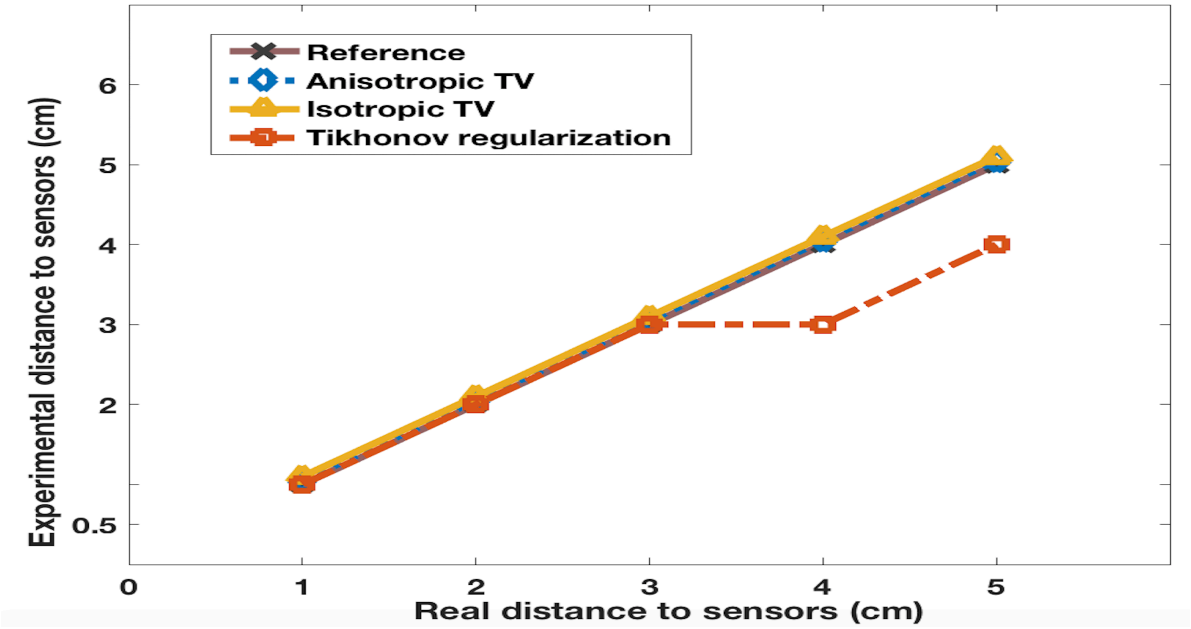

Figure 6.11 Experimental distance against real distance

Table 6.4 The accuracies of depth acknowledged by inverse problem solvers

Reconstructed Distance / Real Distance	Anisotropic TV (cm)	Isotropic TV (cm)	Tikhonov (cm)
1cm	1	1	1
2cm	2	2	2
3cm	3	3	3
4cm	4	4	3
5cm	5	5	4
Average accuracy	100%	100%	91%

Moreover, we present an indicator VR (volume of reconstructed object) to assess the shape of reconstructed objects using planar array MIT system in depth detection. As mentioned before, reconstructed images displayed in this paper are all obtained by applying thresholding. Calculating the number of pixels remaining in the final thresholding images can be treated as a hypothetical method for indicating the volume of reconstructed object. Figure 6.12, which shows the number of voxels remaining in final reconstructed images versus depth, indicates that the volume of samples being reconstructed by isotropic and anisotropic TV are approximately unaffected by increasing depth. Moreover, the reconstructed volume and cross-section size of the sample and can be approximately estimated from the reconstructed images shown in Figure 6.9. Table 6.5 and Table 6.6 explicitly list the estimated volume/ cross-section size of the object and the accuracy of volume/shape reconstruction.

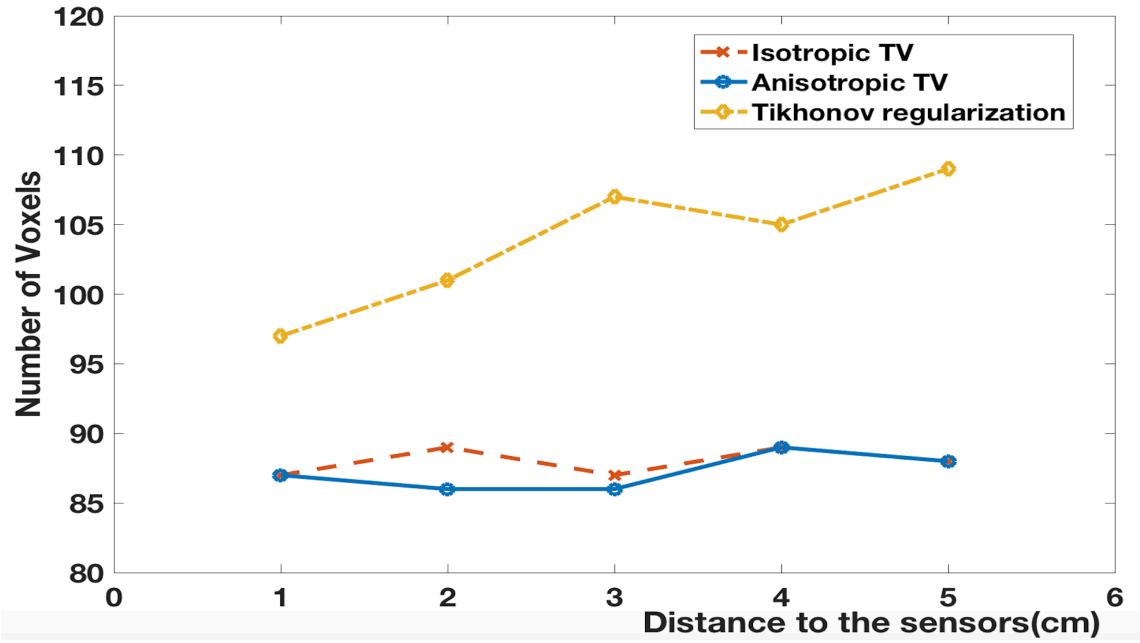

Figure 6.12 Volume of reconstructed objects against depth

Table 6.5 Estimated experimental volume of the samples and volume reconstruction accuracies

Depth (cm)	Estimated Volume	Isotropic TV (cm^3)	Anisotropic TV (cm^3)	Tikhonov (cm^3)
1	Actual Volume $62.85cm^3$	87	87	97
2		89	86	101
3		87	86	107
4		89	89	105
5		88	88	109
Average accuracy		59.7%	61.3%	23.9%

Table 6.6 Estimated experimental cross-section size of the samples and shape reconstruction accuracies

Depth (cm)	Estimated Size	Isotropic TV (cm^2)	Anisotropic TV (cm^2)	Tikhonov (cm^2)
1	Actual Size $12.57cm^2$	16	16	14
2		19	16	22
3		19	17	21
4		16	16	22
5		17	16	20
Average accuracy		61.6%	71.1%	42.5%

Overall, isotropic TV and anisotropic TV can provide better volume and shape reconstruction performance than Tikhonov regularization in depth detection. However, isotropic and anisotropic TV presented similar performance, which may be explained by the fact that isotropic TV performed well for these data. While anisotropic TV can regularize differently along the depth direction, maybe a stronger prior may be needed to recover the loss of sensitivity with depth. In future work, we may consider machine learning, which has been recently proposed for learning inverse problems and seems to be a good candidate to model and correct for depth in planar MIT.

6.4 Conclusions

The capability of planar sensor array MIT system has been investigated using experimental data. Reconstructed images obtained by isotropic and anisotropic TV indicates the position and shape of the samples precisely, which certifies the capability of planar sensor array MIT system for depth detection and verifies that isotropic and anisotropic TV algorithm can produce higher

quality reconstructed images compared to Tikhonov regularization. Even if detectability works only for limited depth, it validated the potential application of planar MIT system for subsurface imaging. The results of enhanced depth detection shown in this study opens up further new applications for planar array MIT in landmine detection.

CHAPTER 7 PLANAR MIT FOR PLASTIC LANDMINE DETECTION

7.1 Introduction

As explosive devices, landmines are designed to protect the countries and peoples during the world wars. These devices are basically planted in or just below the surface of the ground. Landmines can be treated as the most terrifying marks left behind the wars since it not harmed the enemies but turned out to be a treat to the innocent people. According to OneWorld International[12], there are more than 100 million landmines located in 70 countries around the world nowadays. Even worse, landmines can trigger 15,000 to 20,000 casualties every year and most of the damage is unrecoverable, according to the International Campaign to Ban Landmines (ICBC)[12]. Therefore, a global effort should be contributed to the clearance of existing landmines as well as the prevention of further landmines use. This chapter focused on the detection of plastic landmines. The existing techniques working on landmines detection are reviewed in this chapter. The particular interest in this chapter is the planar ECT-MIT technique for plastic landmine detection. This method is illustrated with the aid of methodology and simulation works but focused on planar MIT assisting ECT for plastic landmine detection.

7.2 Existing Landmine locating technology

Even there are more than 350 variations of landmines, they can be divided into two basic categories[78]: Anti-personnel (AP) mines and Anti-tank (AT) mines, designed to disable people or vehicle and Tanks respectively. Besides, according to the material of landmines, they can be divide into metallic landmines, plastic landmines and metal/plastic landmines.

Locating and clearing away landmines is an extremely dangerous and time-consuming procedure, as planted landmines may remain active and most minefields are unmarked. While detection technology is improving, the existing conventional techniques still unable to work efficiently and precisely by its own. Some of the existing techniques are briefly presented as below[12]. Table 7.1 presents the advantages and limitations of each techniques.

Electrical impedance tomography (EIT), an inexpensive and simple system, uses electrical current to conductive medium under investigation and then generate reconstructed images that can indicate its conductivity distributions directly. The presence of metallic or plastic objects in the conductive medium will induce an influence on the conductivity distribution. Since the ground is poorly conductive to a certain degree, EIT is suitable for detecting both metallic and plastic buried landmines. But his technique can only detect the shallowly buried landmines because a sensor-medium contact is required[79].

Metal detectors, working on the principle of electromagnetic induction, can be treated as a feasible solution for Landmine detection. The sensor coils in metal detectors measures the disturbance of an electromagnetic field induced by the metallic targets and then feedback its presence. Therefore, this technique only works efficiently for the metallic landmines[78].

Ground penetration radar (GPR) is the latest technology working on the Microwave principle. After radiating the microwave of low and high frequencies simultaneously into the ground, the return signals reflected by the waves at the boundary of electrical properties discontinuity can be analysed to indicate the presence of the buried metallic and plastic objects. However, this technique works inefficiently in wet soil.

Acoustic sensors are used for landmine detection by projecting acoustic wave into the ground and then the return signals reflected by the waves at the boundary of different acoustical properties of the materials can be obtained. The location of the landmines can be identified by analysing the return signals. According to the previous study of acoustic sensors, it is only suitable for landmines buried in wet soil like clay.

Table 7.1 The comparison of existing techniques for landmine detection

Technique	Advantages	Limitations
EIT	Metallic/Plastic landmines Wet soil	Dry soil Deeply buried landmines
Metal detectors	Metallic landmines	Plastic landmines
GPR	Metallic/Plastic landmines	Wet soil
Acoustic sensors	Wet soil	Sandy soil

7.3 Planar MIT assists ECT for plastic Landmine detection

Electrical capacitance tomography is a non-invasive imaging technique aiming at visualizing the distribution of permittivity by measuring capacitance between electrodes. Theoretically, the samples as well as the medium in sensing area should be non-conductive to avoid the inaccuracy reconstructed images caused by the conductivity[80, 81].

As mentioned in Chapter 1, magnetic inductance tomography (MIT) is also a non-invasive tomography technique designed for imaging the distribution of conductivity by measuring inductance between sensor coils. Since MIT is sensitive to conductivity, plastic or non-conductive medium which can introduce the detectable conductivity contrast between background can disturb the conductivity distribution.

Apparently, MIT itself is incapable of detecting the plastic landmines because of the low conductivity contrast while ECT can work efficiently for detecting the plastic landmines buried in non-conductive or negligibly low conductivity ground. But in the case of the plastic landmines were planted in ground whose conductivity are non-negligible, ECT requires the assistance provided by planar MIT. Figure 7.1 presents a simplified schematic diagram of plastic landmines buried under ground.

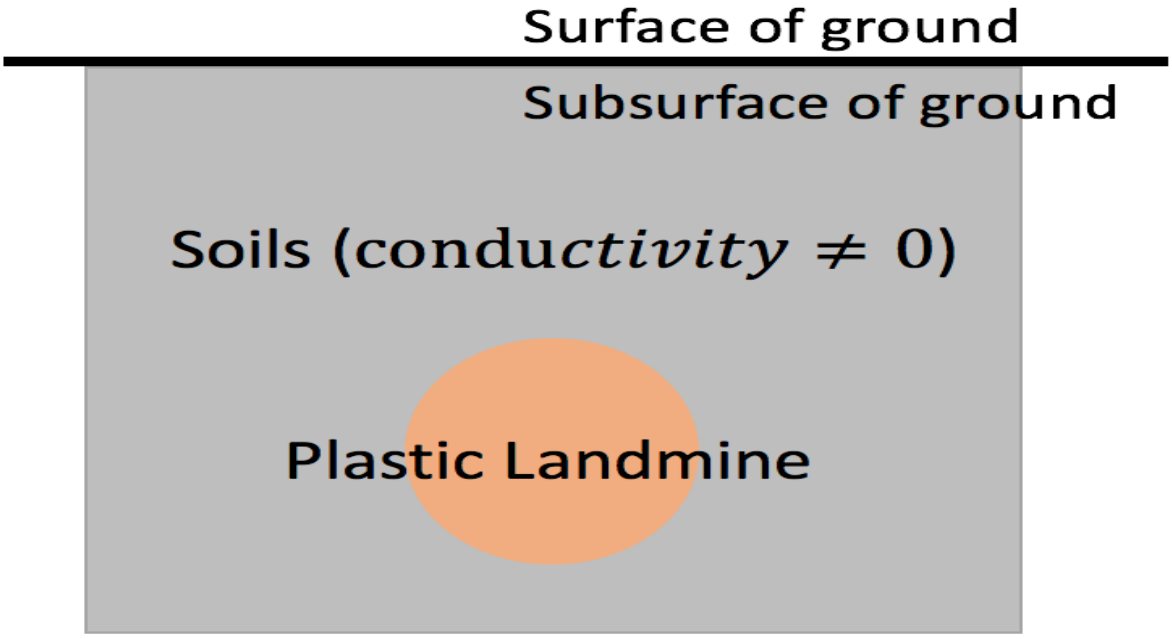

Figure 7.1 The comparison of existing techniques for landmine detection

In order to obtain the reconstructed images indicating the permittivity distribution by ECT, forward and inverse problems must be solved.

The normalized form of inverse problem of ECT can be expressed as[82]:

$$J\Delta\varepsilon = \Delta C \tag{7.1}$$

Where $\Delta\varepsilon$ is the vector of permittivity distribution change ($\Delta\varepsilon \in R^n$) and Δv is the vector of time difference measurement of capacitance ($\Delta C \in R^m$), J is the Jacobian matrix ($J \in R^{m\times n}$)[83, 84]. Then the key point of solving the inverse problem is the calculation of J. The Jacobian matrix J is the capacitance change with respect to the permittivity that can be obtained from the forward problem of ECT[30].

According to [85], the relationship between electrical potential $u(x)$, conductivity distribution $\sigma(x)$ and permittivity distribution $\varepsilon(x)$ can be expressed as:

$$\nabla[\varepsilon(x) + \frac{\sigma(x)}{i\omega}]\nabla u(x) = 0 \tag{7.2}$$

And the electric charges of the p-th electrode is as below:

$$Q_p = -\int_{\Omega_p}[\varepsilon(x) + \frac{\sigma(x)}{i\omega}]\frac{\partial u(x)}{\partial \mathrm{n}} d\,\Omega \tag{7.3}$$

Where n is the norm vector on the electrode. Normally, $\sigma(x)$ assumed to be zero and then equation 7.3 can be simplified to[86]:

$$Q_p = -\int_{\Omega_p} \varepsilon(x)\frac{\partial u(x)}{\partial \mathrm{n}} d\,\Omega \tag{7.4}$$

For ECT used for plastic landmines detection, the Jacobian matrix J can be calculated by equation 7.3 with the known information of permittivity and conductivity distributions, where conductivity distribution can be provided by MIT.

As it has been mentioned before, ECT can be an approach for plastic landmine detection in the case of landmine buried in non-conductive ground, but in the real life, landmines are placed in soils whose conductivity is not equal to zero. MIT can be potentially applied to plastic landmine detection since it can work properly as an imaging technique if conductivity contrast exists. But it's not capable for low conductivity contrast theoretically, i.e., plastic landmine buried in soils whose conductivity is extremely low. Therefore, ECT with the aid of MIT can be a better approach for plastic landmine detection. The working process of planar MIT helps ECT for plastic landmines detection is shown in Figure 7.2.

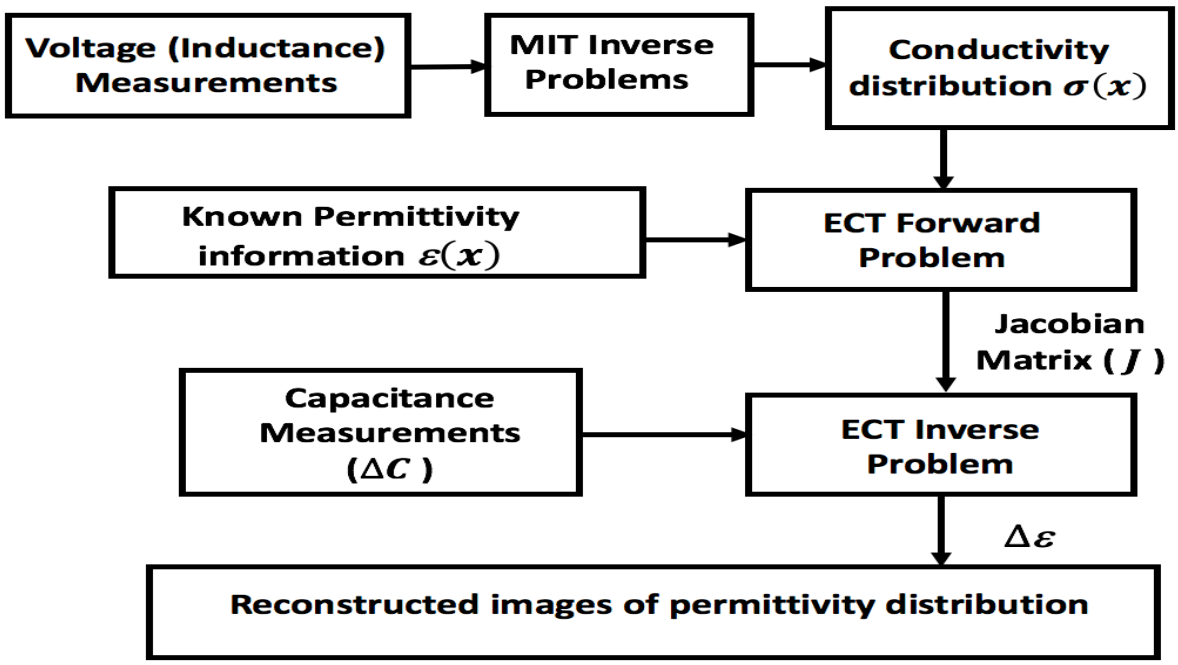

Figure 7.2 Working flow chart of MIT-ECT for plastic landmines detection

This chapter is focus on the process of acquiring the conductivity distributions ($\sigma(x)$) of plastic landmines buried in soils by planar MIT system.

7.4 Simulation results of Planar MIT for plastic Landmine detection

The model of Plastic landmines buried in soils (Figure 7.1) simulated in planar MIT is demonstrated in Figure 7.3. The blue and orange cuboid are simulated to be the conductive soils and plastic landmine respectively. The parameters of the simulated sensors are shown in Table 7.2. In general, the sensor coils used in low conductivity MIT system have less turns than those used in high conductivity system [3, 7, 87]. Too few numbers of turns produce too low inductance, which will cause too weak magnetic flus to induce strong voltage that can be detected by the receiver; but too large number of turns will cause the coil resonance frequency becomes too close to the operation frequency, which will cause system instability[19, 88, 89]. And here the number of turns selected to be 6 according to [7, 21].

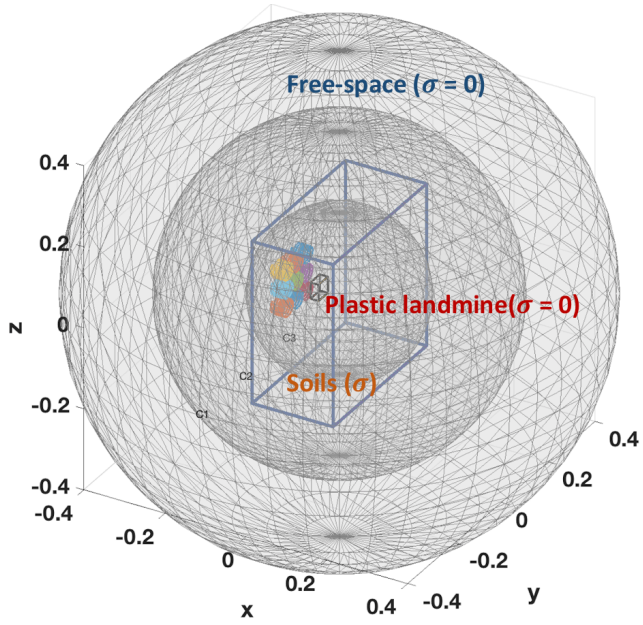

Figure 7.3 Simulation model in planar MIT system

Table 7.2 Parameters of the sensor coils model

Number of coils	9
Number of turns	6
Self-inductance (μH)	380
Coil height (cm) (H)	5
Coil side length (cm) (S)	3.4
Outer diameter (cm)	4.1
Inner diameter (cm)	3.9
Surface area of the board (cm^2)	14×14
Thickness of the board (cm) (T)	0.2

The sensitivity map for selected measurements pairs in proposed MIT system are shown in Figure 7.4. All the sensitivity maps shown below are calculated for the free space scenario, which means there is no conductive or non-conductive sample investigated.

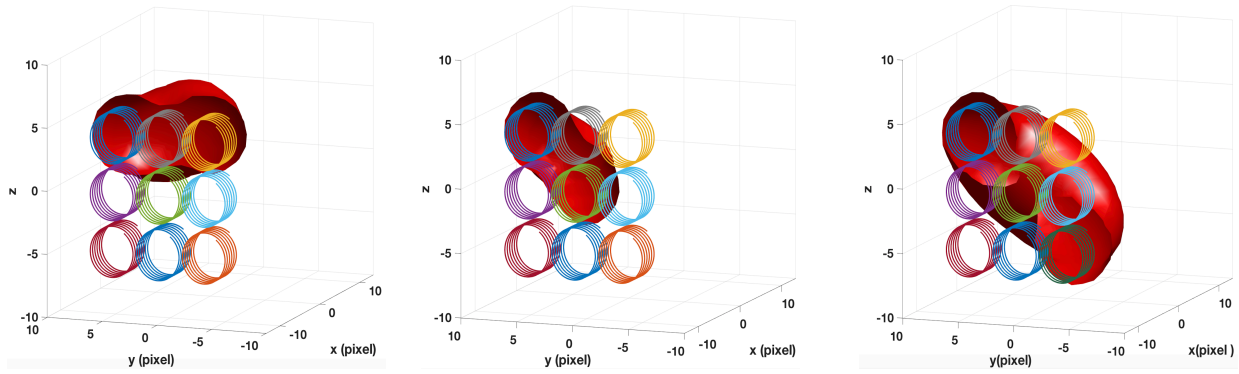

Coil pair 1-3 Coil pair 1-5 Coil pair 1-9

Figure 7.4 Sensitivity maps for measurements pairs

7.4.1 Simulated results of induced voltages

As it has been mentioned in Chapter 4.2 that for low conductivity samples or lower conductivity contrast, the voltage detected in the receiving coils is:

$$v_2 = -M_{12}\frac{v_1}{L_1} + jM_{13}M_{23}\frac{\omega v_1}{L_1 R} \tag{7.5}$$

where L_1 is the self-inductance of the excitation coils, M_{12}, M_{13} and M_{23} are mutual inductances that are related to the coils structure. ω is related to the excitation frequency and R is related to the experimental samples.

It clearly that the induced voltage obtained in plastic landmine detection here includes real part and imaginary part.

The proposed simulation model (procedure) and simulation results are introduced in Table 7.3. The excitation frequency is $10MHz$.

Firstly, a cuboid simulated to be the low conductive soils as reference measurements V_{soils}. And another smaller cuboid simulated to be the plastic landmine that is placed in soils, where a set of voltages measured are the plastic landmine measurements $V_{landmine}$. The plots of each set of 36 voltage measurements are presented in the table as following. The plastic landmine is

placed in the $0.8\,S/m$ soils with a depth of $4cm$ in this case.

Table 7.3 Simulated results of induced voltages

Background: Soils measurements V_{soils}	Samples: Plastic landmine measurements $V_{landmine}$
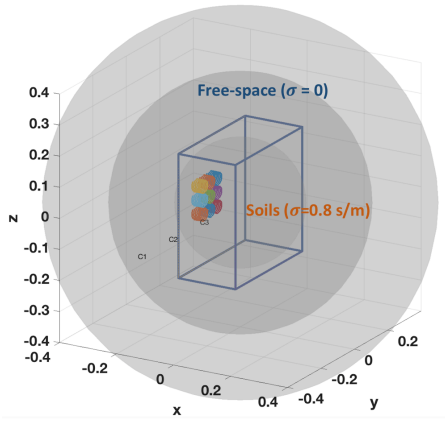	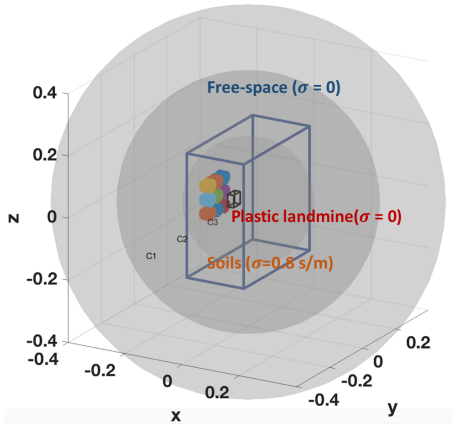
Difference of induced voltage $V_{landmine} - V_{soils}$	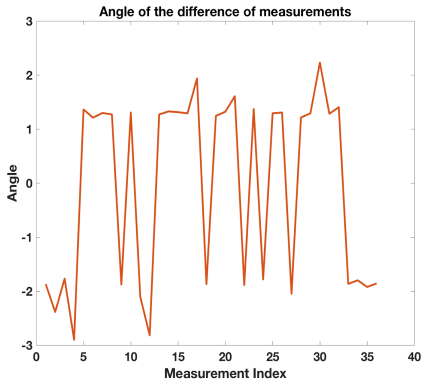 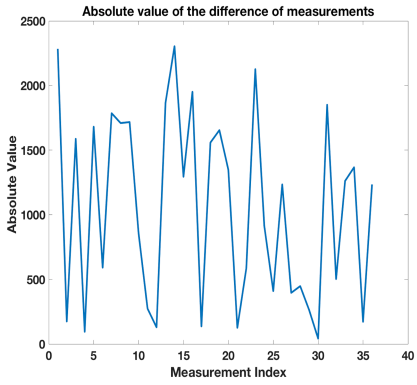

Table 7.4 indicates the conductivity values of four basic types of soils in reality [90].

Table 7.4 The conductivity values of different types soils

Unified Soil Classification	Conductivity σ (S/m)
Salinity	10^{-1} to 10^{0}
Clay	2×10^{-2} to 8×10^{-1}
Silt	5×10^{-3} to 8×10^{-2}
Sand	5×10^{-4} to 2×10^{-2}

Then another set of simulation works are conducted by setting $\sigma_1 = 8 \times 10^{-1}\, S/m$, $\sigma_2 = 8 \times 10^{-2}\, S/m$, $\sigma_3 = 5 \times 10^{-3}\, S/m$. In this research, the maximum value of background conductivity is selected to be $\sigma_1 = 8 \times 10^{-1}\, S/m$, but the soils could be larger than σ_1 in real-life. The distances between plastic landmines and coils are $2cm$, $3cm$ and $5cm$. The simulation results of induced voltages are presented as the angle and absolute value of $V_{landmine} - V_{soils}$ with respect to different conductivity and depth, shown in Table 7.5.

Table 7.5 Simulated induced voltage measurements of different conductivity and depth

Conductivity σ (S/m)	Induced voltage measurements $V_{landmine}$		
Depth	$2cm$	$3cm$	$5cm$
8×10^{-1}	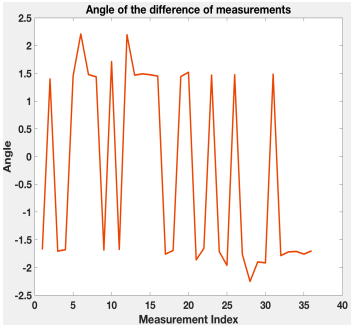 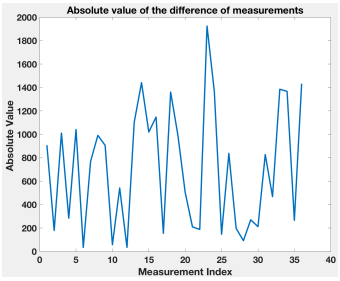	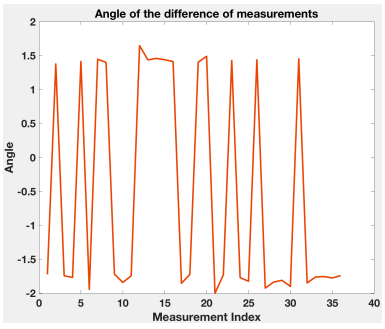 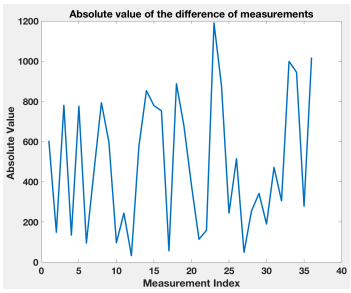	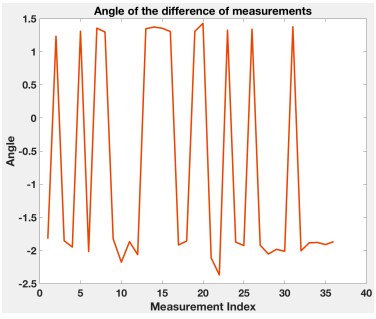 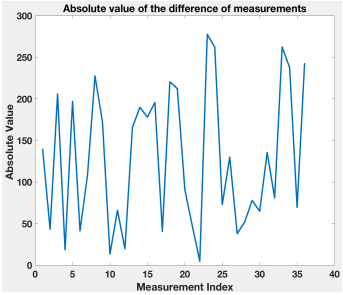

8×10^{-2}	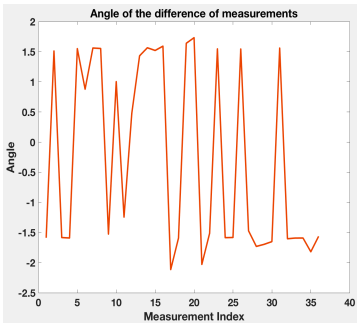 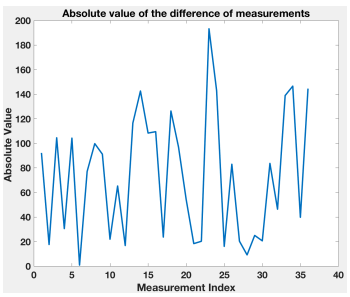	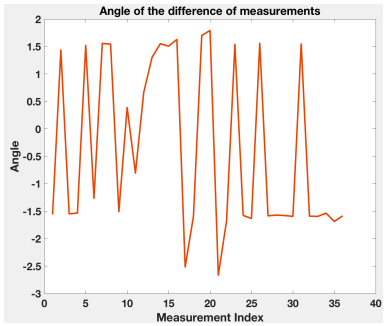 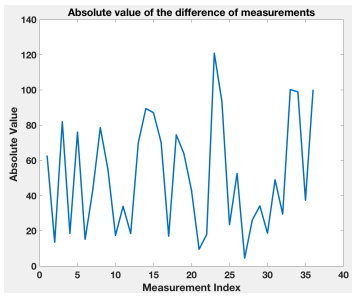	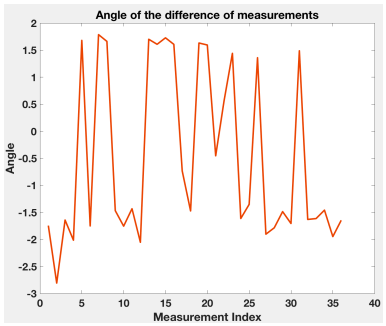 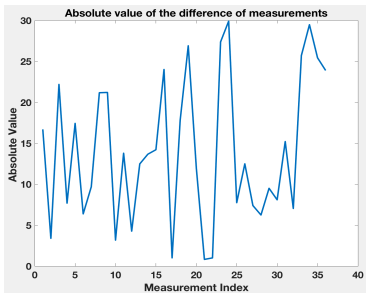
5×10^{-3}	 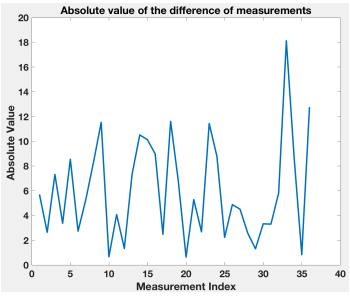	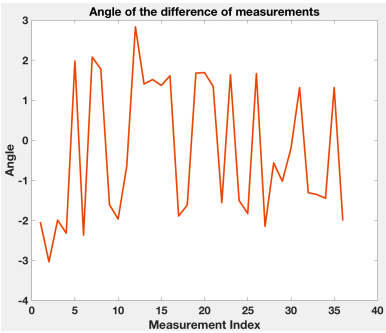 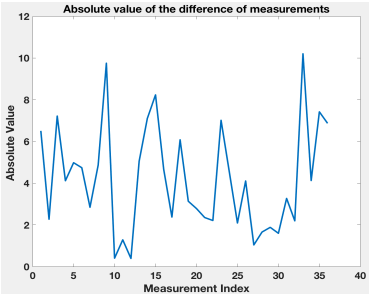	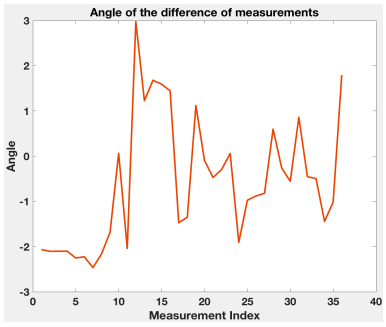 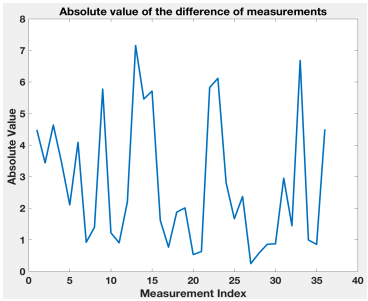

7.4.2 Simulated results of reconstructed images

Moreover, the simulated reconstructed images of landmine detection can be accomplished by solving the inverse problem. The voltage measurements obtained in this simulation work include real part and imaginary part. In theory, the reconstruction images should be

reconstructed through the sum of real and imaginary part, but it is unable to implemented at this stage. Since that, the simulated reconstructed images are produced by real part and imaginary part of induced voltage respectively.

And the inverse problem can be solved with the aid of simulated voltage measurements and isotropic TV regularization algorithm. Two sets of simulation works are expressed in this chapter: data without noise; data with noise.

- Simulated results accomplished by simulated induced voltage without noise

The simplified top view of the simulation work is shown in Figure 7.5.

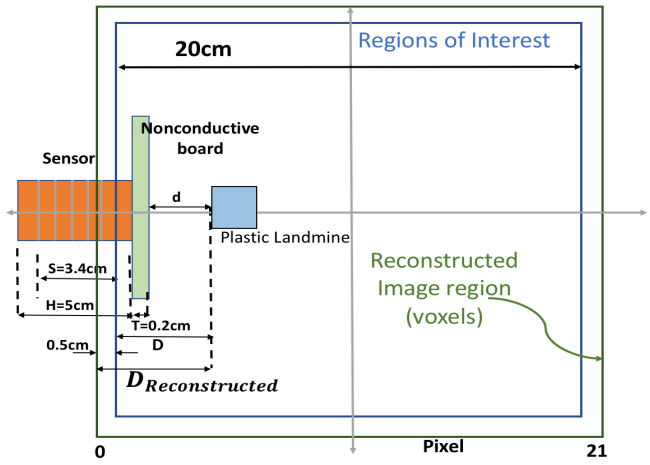

Figure 7.5 Simplified top view of the simulation work

The parameters used to solve the inverse problem of this section are shown in Table 7.6.

Table 7.6 Parameters used to solve the inverse problem

Parameter	$\sigma = 8 \times 10^{-1}$		$\sigma = 8 \times 10^{-2}$		$\sigma = 5 \times 10^{-3}$	
	Imaginary Part	Real Part	Imaginary Part	Real Part	Imaginary Part	Real Part
mu	$5e-1$		$5e-1$		$5e-1$	
lambda	$1e-3$		$1e-4$		$1e-5$	
gamma	$1e-1$		$1e-1$		$1e-1$	
nBreg	200		300		300	

The simulated reconstructed images of landmine detection without noise in data are shown in Table 7.7, which includes results obtained from imaginary and real part of voltage measurements respectively.

Table 7.7 Simulated reconstructed images of landmines detection by isotropic TV (without noise)

Conductivity $\sigma(S/m)$	Reconstructed images obtained by imagine part and real part of isotropic TV respectively		
Depth	$2cm$	$3cm$	$5cm$
8×10^{-1}	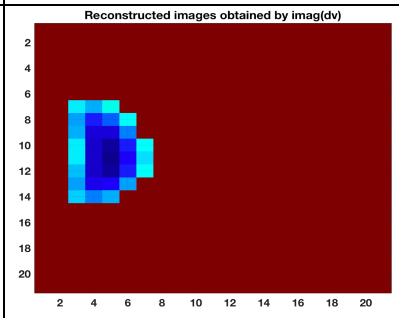	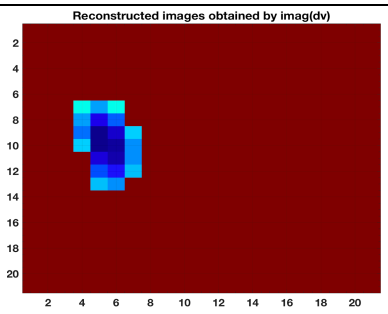	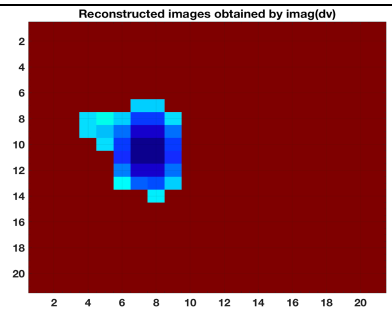
	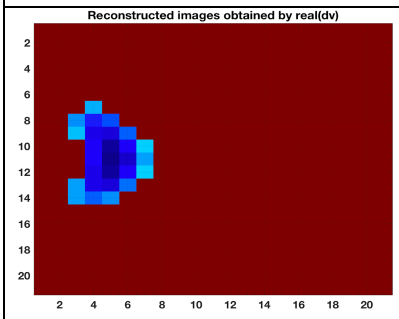	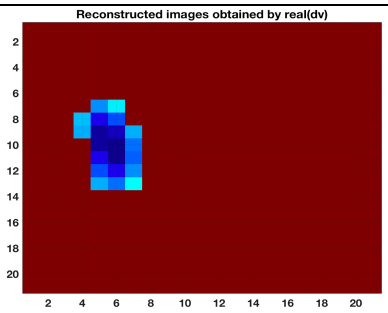	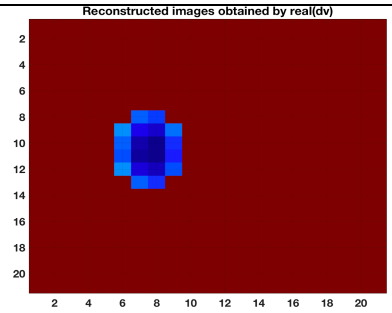
8×10^{-2}	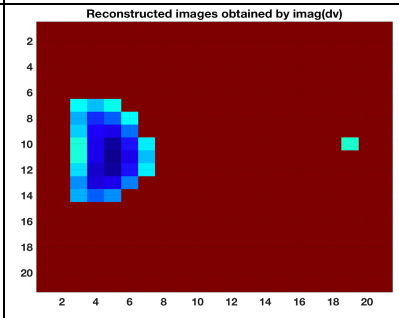	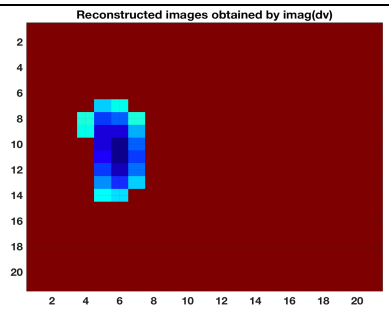	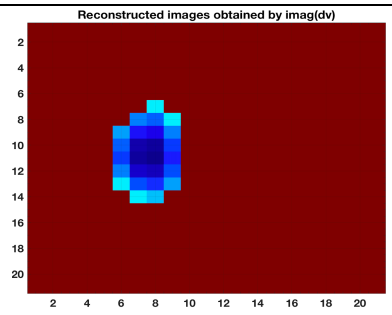
	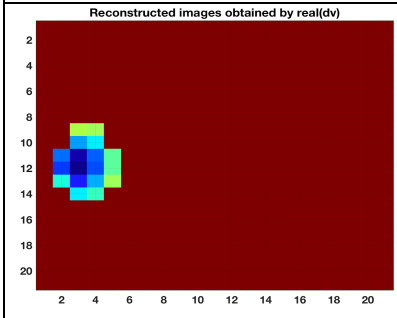	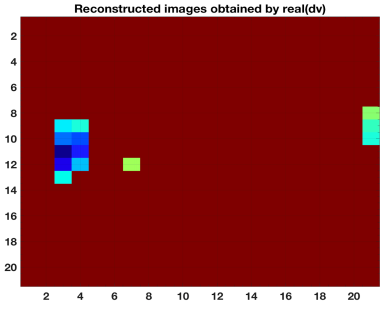	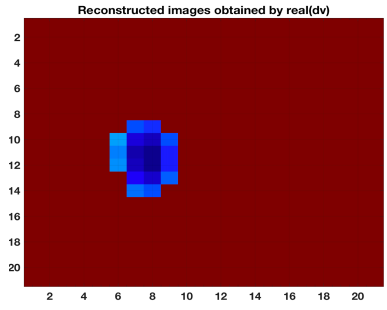

5×10^{-3}	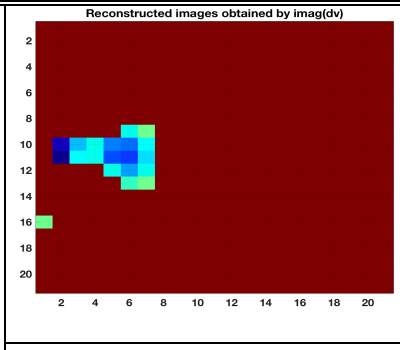	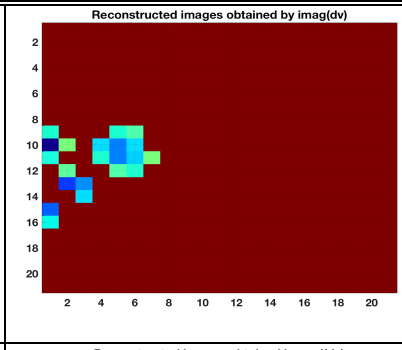	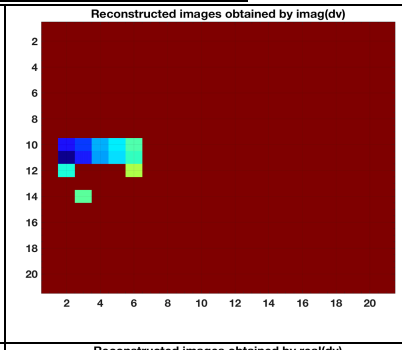
	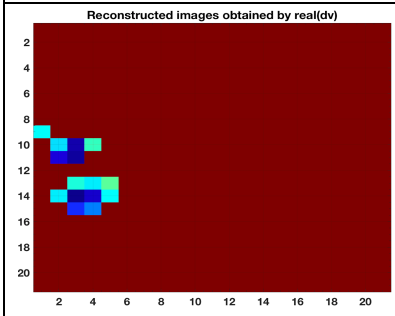	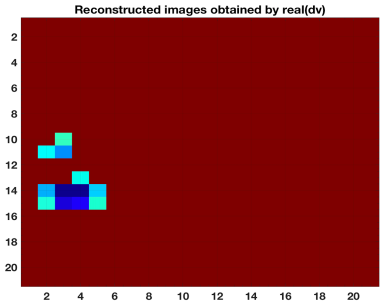	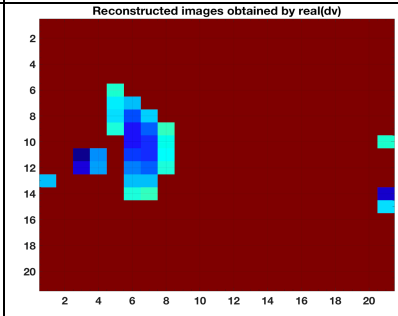

As it has been introduced in Chapter 6.21, Figure 7.5. indicates that the experimental distance can be obtained from the distance shown in reconstructed image as following: $D = D_{Reconstructed} - 0.5$. The voxel number here is selected to be 21. The voxel size is $1cm \times 1cm \times 1cm$. Conclusions can be summarized from the above table as following: 1) imaginary and real part results of $\sigma_1 = 8 \times 10^{-1}\, S/m$ indicate that TV regularization is able to be sensitive to the depths of sample in accordance with real experimental setup; 2) imaginary part results of $\sigma_2 = 8 \times 10^{-2}\, S/m$ show the depth consist with actual depth while real part results are not accurate with all depth. 3) results of $\sigma_3 = 5 \times 10^{-3}\, S/m$ are unable to recover the landmines, which might because of low conductivity contrast.

Table 7.8 indicates the absolute values and phase angle of the simulated differences of measurements against different depths and conductivity contrasts. Table 7.9 demonstrates the percentage changes for both simulated imaginary and real part with respect to different depths and conductivity contrasts.

Table 7.8 Absolute values and phase angle of the difference of measurements

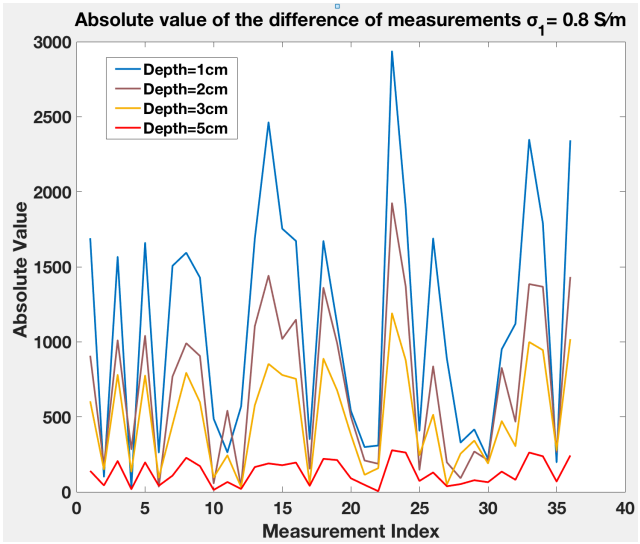

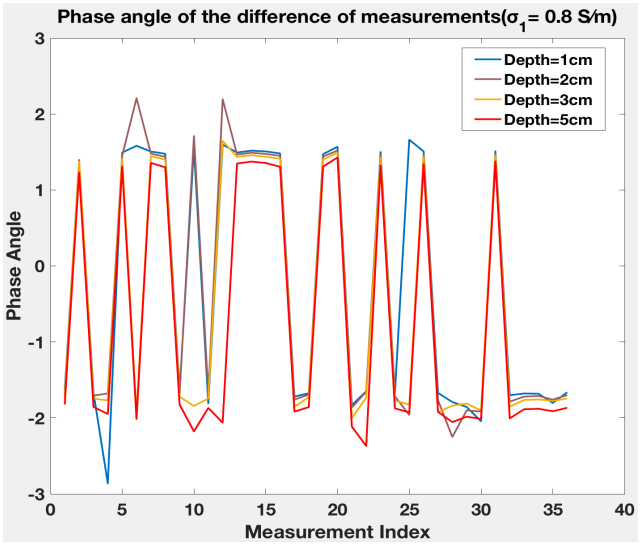

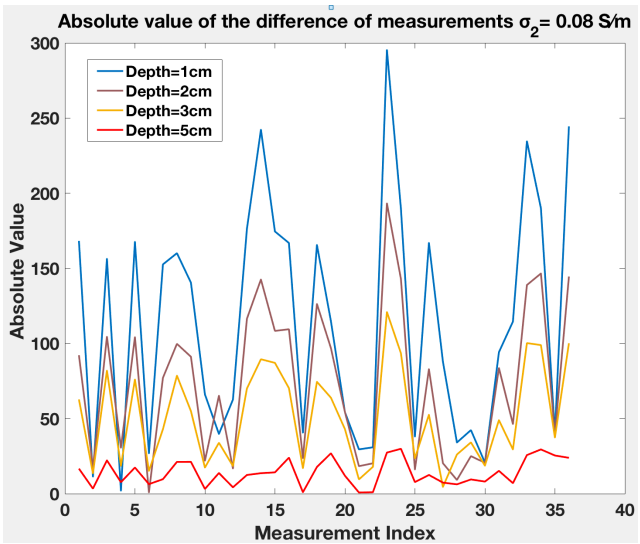

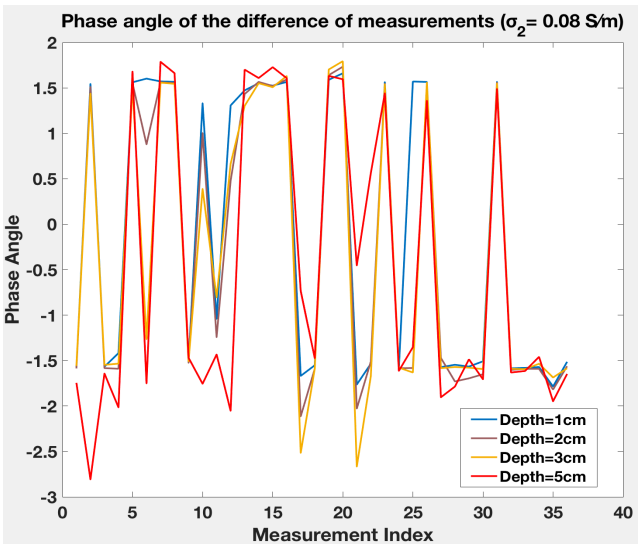

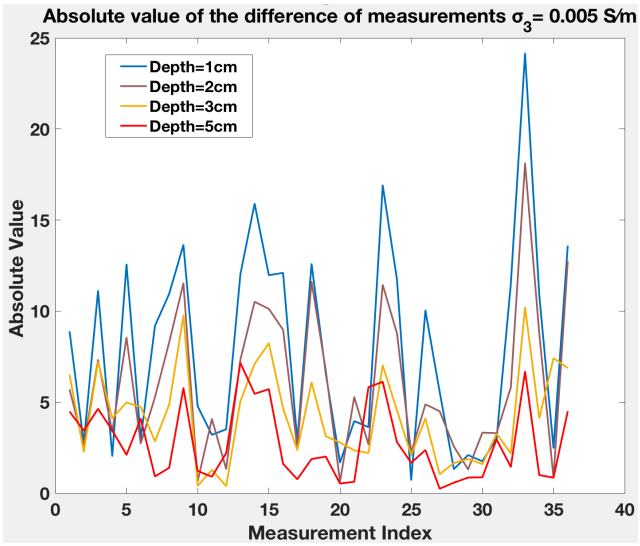

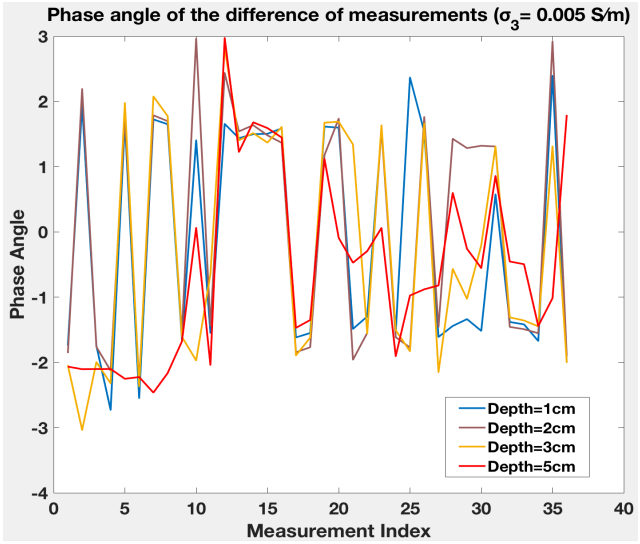

All the reconstructed images shown in Table 7.8 illustrates that with the depth increase, the absolute value and the phase angle are decreasing. And by comparing the images in each column, it can be seen that with the conductivity of the soil decrease, the absolute value and phase angle are decreasing.

Table 7.9 Percentage of changes for both imaginary and real part

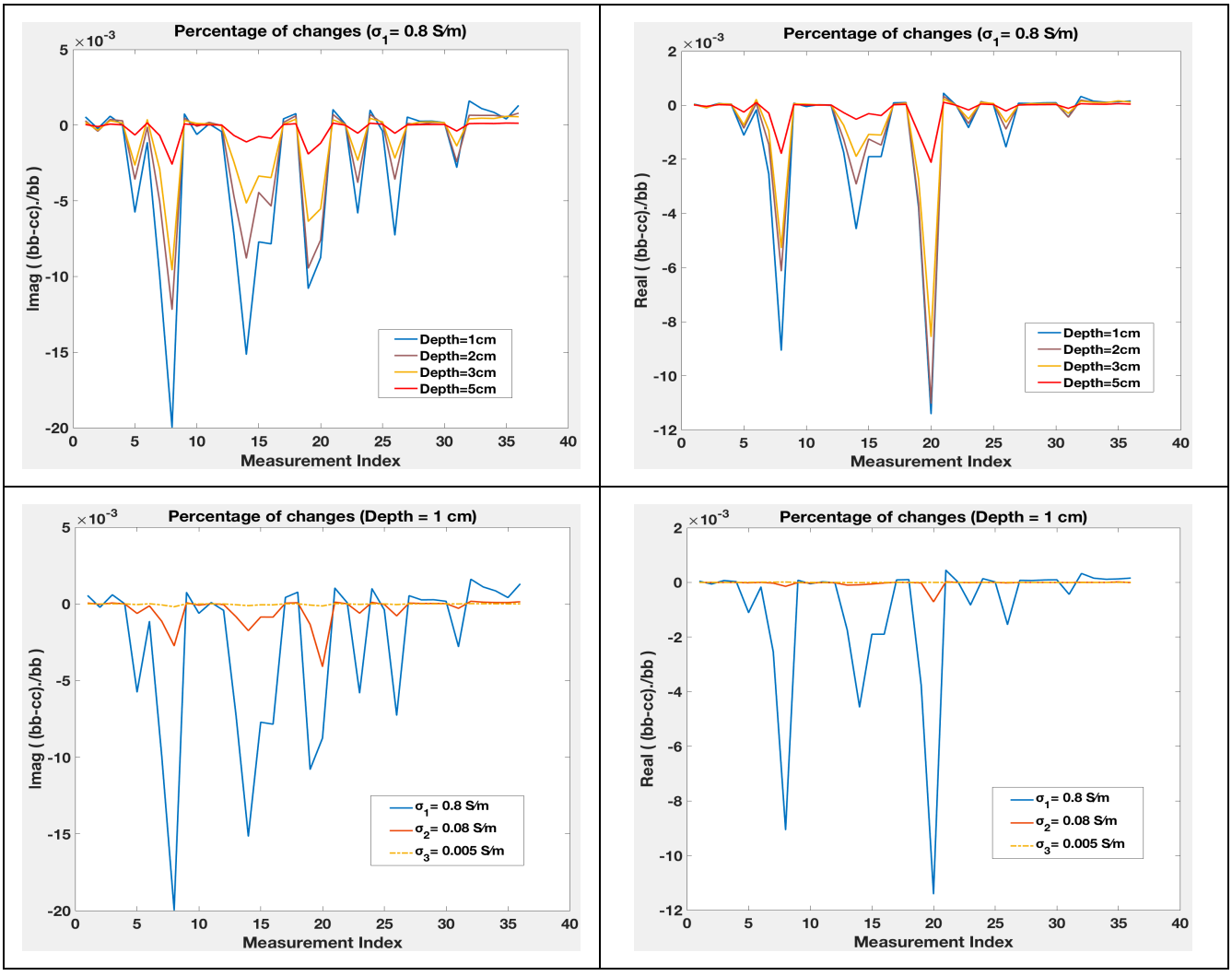

Conclusions can be summarized from Table 7.9 as following: 1) images shown in first row indicates that with the depth increase, changes in both real part and imaginary part are becoming weaker; 2) images displayed in second row that with the conductivity decrease, changes in both real part and imaginary part are becoming weaker as well.

- Simulated results accomplished by simulated induced voltage with noise

To demonstrate the reliability of plastic landmine detection using low conductivity MIT system, noise should be added onto the voltage measurements to simulate the accuracy of the reconstruction. In theory, the magnitude and the phase angle of the complex value of voltage measurements will be affected by different level of noise respectively. According to the impedance analyzer[91], the accuracy of the phase angle measurement normally equals 1% of the one on the magnitude, which means the noise added to phase angle would be much smaller than the one on the magnitude. Since that, the noise added to phase angle is ignored in our MIT case, the noisy induced voltage is expressed as below. Same value of noises is added into both real and imaginary part to make sure noise is just added onto the magnitude of the voltage measurements.

$$\Delta v = \Delta v_{real} + i\Delta v_{imag} \tag{7.1}$$

$$e = E \times mean(abs(\Delta v)) \tag{7.2}$$

$$\Delta v_{noise} = (\Delta v_{real} + rand(M,1) * e) + i(\Delta v_{imag} + rand(M,1) * e) \tag{7.3}$$

Where Δv is the complex induced voltage, Δv_{real} is the real part, Δv_{imag} is the imaginary part, e is the noise, E is the noise level and M is the measurement number ($M = 36$ in this case).

The noise levels are chosen at $E = 2\%$, $E = 8\%$, $E = 80\%$. All the parameters used to solve the inverse problem are shown in Table 7.10.

Table 7.10 Parameters used to solve the inverse problem ($E = 2\%, 8\%, 80\%$)

Parameter	$\sigma_1 = 8 \times 10^{-1}\, S/m$		$\sigma_2 = 2 \times 10^{-1}\, S/m$		$\sigma_3 = 8 \times 10^{-2}\, S/m$	
	Imaginary Part	Real Part	Imaginary Part	Real Part	Imaginary Part	Real Part
mu	0.5		0.5		0.5	
lambda	$1e-3$		$1e-4$		$1e-4$	
gamma	$1e-1$		$1e-1$		$1e-1$	
nBreg	300		400		400	

Table 7.11-7.13 shows the simulated results of landmine placed in different conductivities ground with different noise level and the depth is kept being $2cm$.

Table 7.11 Simulated reconstructed images of landmines detection by isotropic TV (with Noise level = 2%)

Noise level (E)	Conductivity σ (S/m)	Reconstructed images obtained by imagine part and real part of isotropic TV respectively (Depth = $2cm$)	
		Imagine part	Real part
2%	8×10^{-1} 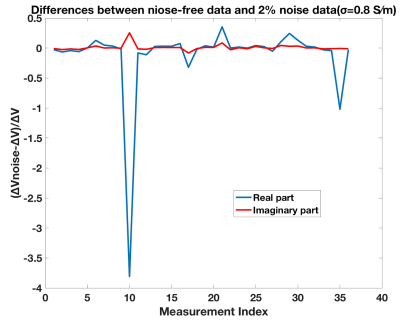	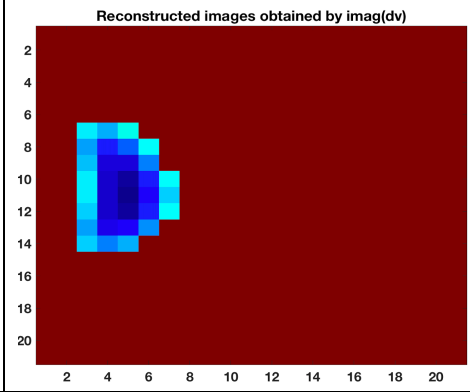	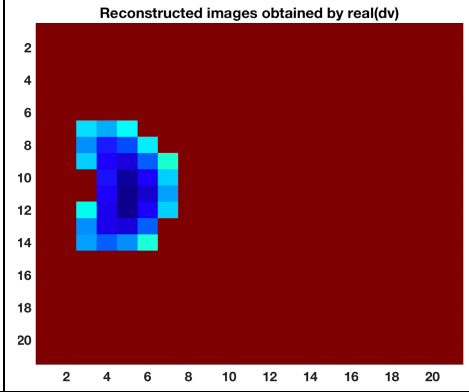
	2×10^{-1} 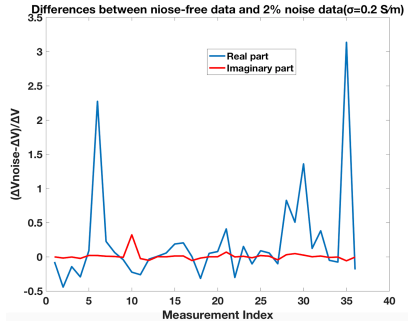	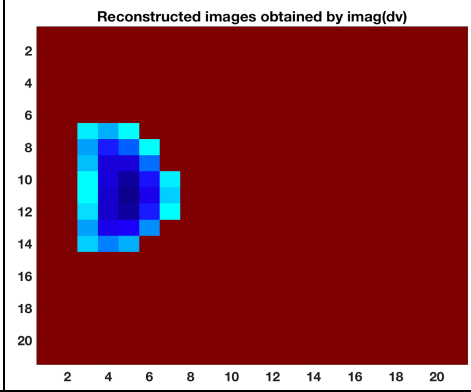	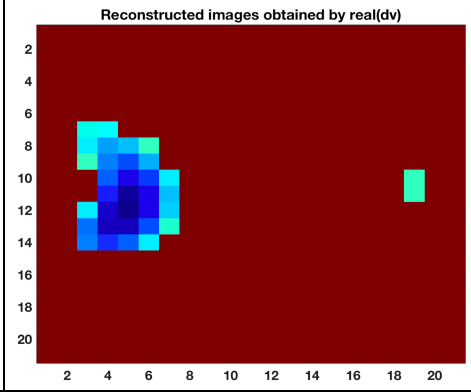
	8×10^{-2} 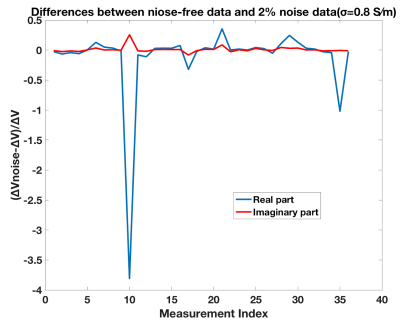	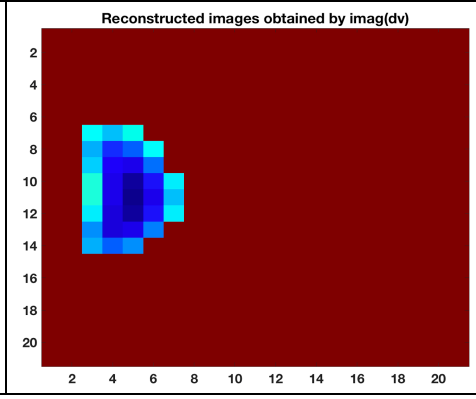	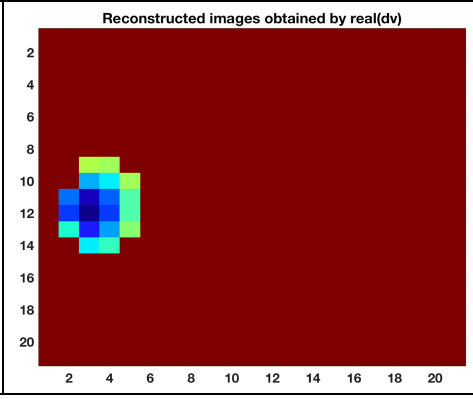

Conclusions can be summarized from the Table 7.11 as following: 1) imaginary and real part results of $\sigma_1 = 8 \times 10^{-1}\, S/m$ and $\sigma_2 = 2 \times 10^{-1}\, S/m$ with $E = 2\%$ indicate that TV regularization is able to be sensitive to the depths of sample in accordance with real

experimental setup; 2) imaginary part results of $\sigma_3 = 8 \times 10^{-2}\, S/m$ with $E = 2\%$ show the depth consist with actual depth while real part results are not accurate. 3) It can be seen from the plots of differences between noise -free data and data with noise in second column that with the reduction of the conductivity contrast, the changes induced by noise are increasing with larger percentages in real part than imaginary part.

Table 7.12 Simulated reconstructed images of landmines detection by isotropic TV (with Noise level = 8%)

Noise level (E)	Conductivity σ (S/m)	Reconstructed images obtained by imagine part and real part of isotropic TV respectively (Depth = $2cm$)	
		Imagine part	Real part
8%	8×10^{-1} 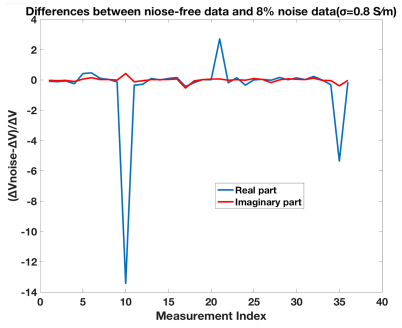	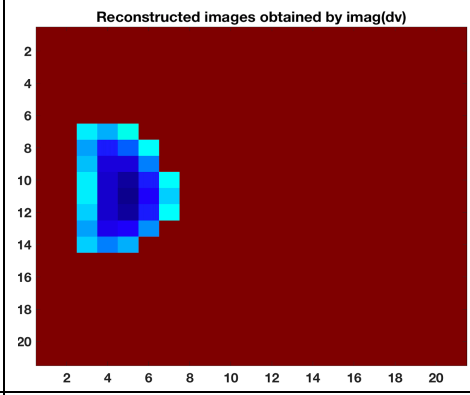	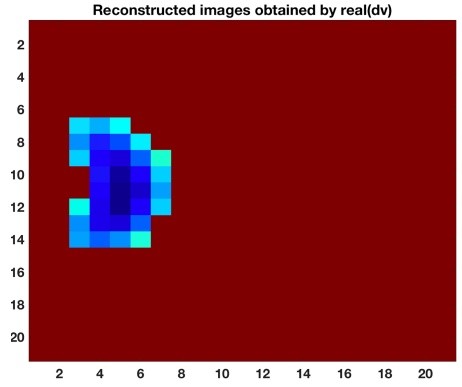
	2×10^{-1} 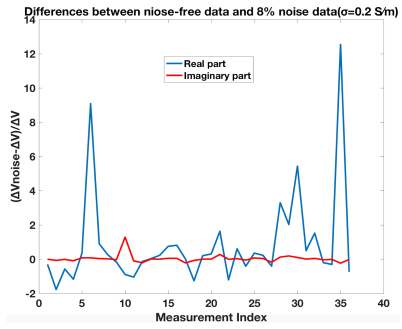	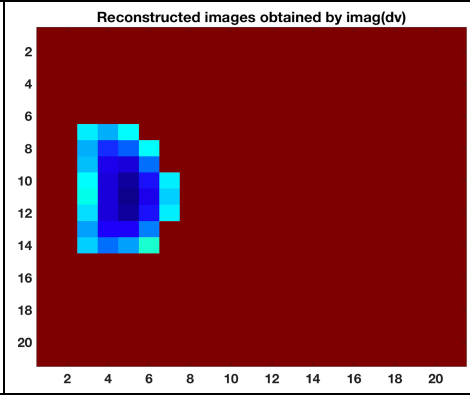	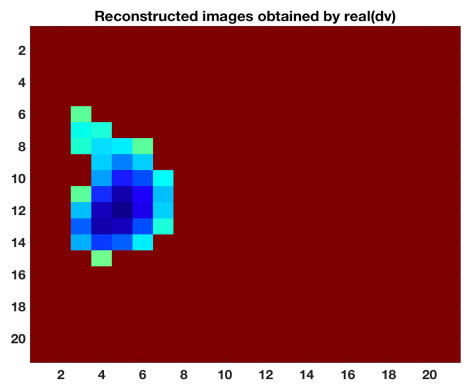
	8×10^{-2} 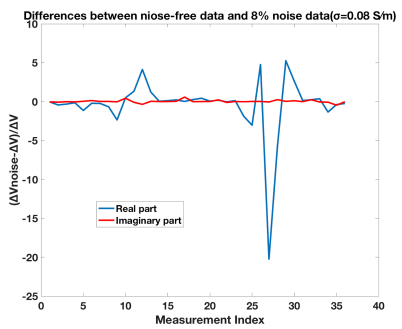	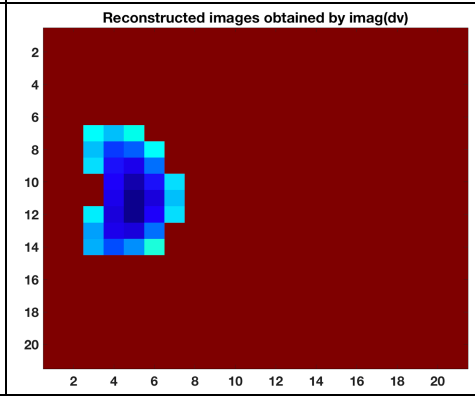	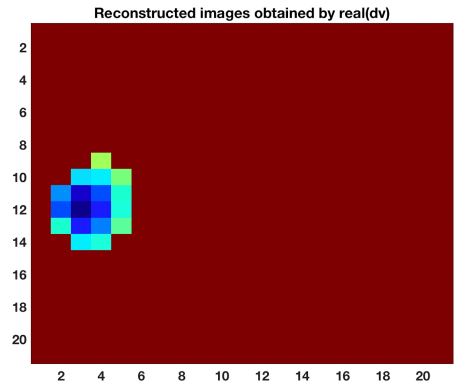

Conclusions can be summarized from the Table 7.12 as following: 1) imaginary and real part results of $\sigma_1 = 8 \times 10^{-1}\, S/m$ with $E = 8\%$ indicate that TV regularization is able to be sensitive to the depths of sample in accordance with real experimental setup; 2) imaginary part results of $\sigma_2 = 2 \times 10^{-1}\, S/m$ with $E = 8\%$ show the depth consist with actual depth while real part results are accurate but with unclear images. 3) imaginary part results of $\sigma_3 = 8 \times 10^{-2}\, S/m$ with $E = 8\%$ show the depth consist with actual depth while real part results are not accurate. 4) It can be seen from the plots of differences between noise -free data and data with noise in second column that with the reduction of the conductivity contrast, the changes induced by noise are increasing with larger percentages in real part than imaginary part.

Table 7.13 Simulated reconstructed images of landmines detection by isotropic TV (with Noise level = 80%)

Noise level (E)	Conductivity σ (S/m)	Reconstructed images obtained by imagine part and real part of isotropic TV respectively (Depth = $2cm$)	
		Imagine part	Real part
80%	8×10^{-1} 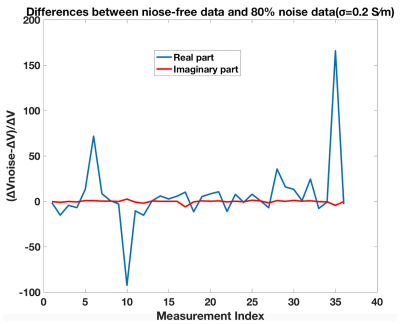	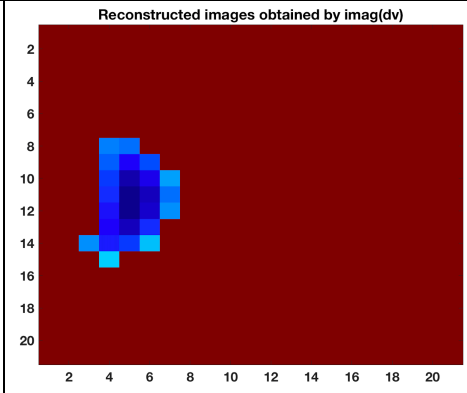	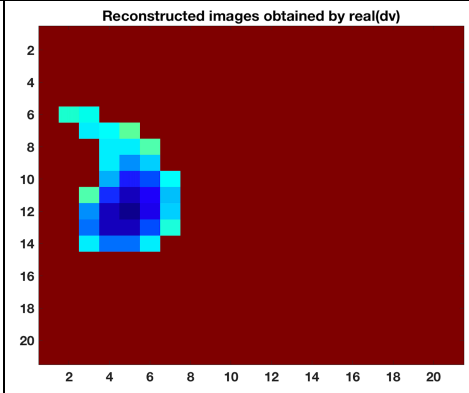
	2×10^{-1} 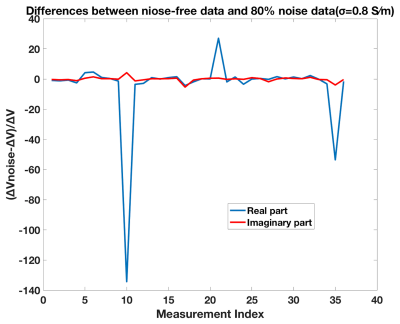	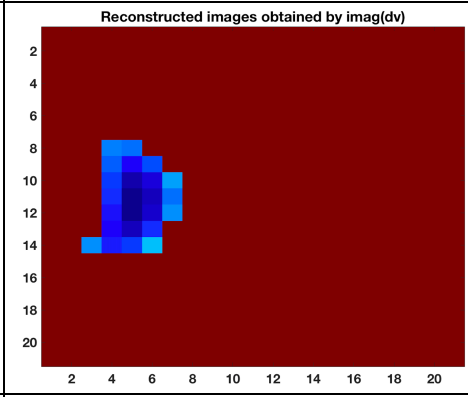	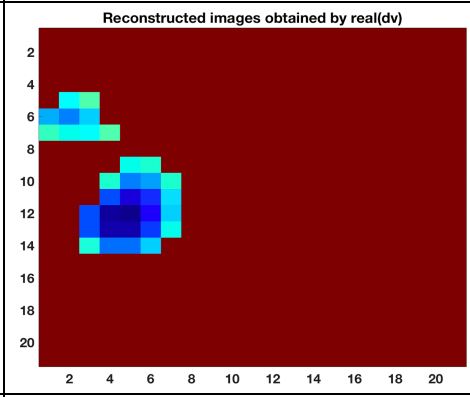
	8×10^{-2} 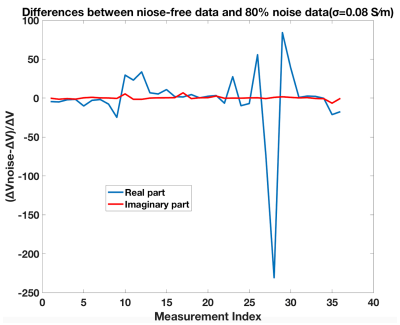	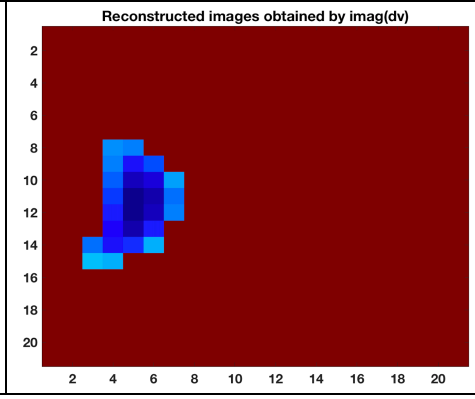	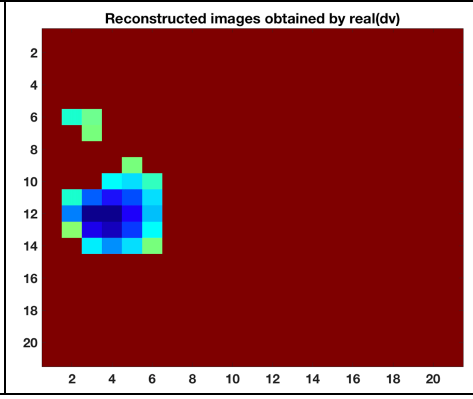

Conclusions can be summarized from the Table 7.13 as following: 1) imaginary and real part results of $\sigma_1 = 8 \times 10^{-1}\, S/m$, $\sigma_2 = 2 \times 10^{-1}\, S/m$ and $\sigma_3 = 8 \times 10^{-2}\, S/m$ with $E = 80\%$ indicate that TV regularization are unable to recover the landmines in the accurate

positions or shapes. 2) with the reduction of the conductivity contrast, the changes induced by noise are increasing with larger percentages in real part than imaginary part.

Therefore, images shown in Table 7.11-7.13 indicates that the changes induced by noise are increasing with different percentages in real and imaginary parts; the reduction of the conductivity contrast will make the noise level that can disturb the system decreasing as well.

7.5 Conclusions

High frequency MIT is proposed for landmine detection with conductive ground. It is shown than presence of plastic landmine few centimeters under conductive ground can be sensed by means of MIT phase detection. Data from simulation study demonstrate in a sufficiently conductive ground of around 0.5 S/m a plastic landmine can be detected. The measured data was then combined with noise so that a more realistic scenario could be modelled, which again shows the robustness of the proposed method.

CHAPTER 8 CONCLUSIONS AND FUTURE WORK

8.1 Conclusions

As it has been mentioned in aims and objectives of this research work in Chapter 1.3, the main subject of this thesis is improving the quality of images reconstructed by MIT system through modifying forward modeling and analyzing inverse algorithms. Each chapter raises a specific problem and presents the investigation procedure that have been conducted, the methodologies that haven been applied, the experimental or simulation results obtained, the in-depth discussions and the valuable novel findings or conclusions.

The forward problem and inverse problem are the important subjects of this dissertation.

The forward problem for MIT, based on the eddy current problem and Maxwell's equations, normally solved by edge FEM techniques, which need to mesh the coil structure into forward modeling. In this thesis, Biot-Savart law are adopted to replace meshing the coil structure in both circular sensor array and planar sensor array MIT, which is defined as a potential calculation method for increasing the flexibility of the forward model. The simulation processes of circular sensor array and planar sensor array modeling are also discussed in this chapter, which proved that Biot-Savart law is an important element of the software design of MIT. Moreover, in order to improve the resolution of the reconstructed images, the forward models have been modified and validated, which are also illustrated in this chapter.

The inverse problem chapter presents two algorithms applied in solving inverse problem, which includes the commonly used Tikhonov regularization method and the advanced algorithms named Split Bregman based total variation regularization. Total variation regularization algorithm was selected to be the optimal inverse problem solvers in this thesis. At the later stage of this research, this inverse solver was implemented into different MIT

scenario and applications, i.e., circular sensor array MIT, planar sensor array MIT and plastic landmine detection.

The applications of adopting total variation regularization to solve the inverse problem of MIT are the other key subjects of this thesis.

Chapter 5 presents the how total variation regularization could be an optimal inverse problem solver for circular sensor array MIT, which is an application of TV never before attempt. A journal paper is demonstrated particularly for this research with the aid of experimental data and quantitative analysis. Quantitative image quality analysis conducted in this chapter shows significant improvement of image qualities by using proposed TV algorithm, making TV algorithm a suitable candidate for image reconstruction in both high conductivity and low conductivity MIT imaging. It is anticipated that the high-quality images that can be obtained using TV algorithm and its robustness against image reconstruction parameters, can help stimulate new applications for MIT in both industrial tomography and medical imaging. Moreover, this is also making TV becomes a candidate for solving the inverse problem of planar sensor array MIT system.

Chapter 6 investigate the capability of planar sensor array MIT system using experimental data. Another novel is developed particularly for this problem. The capability of planar sensor array MIT system for depth detection are certified by the images reconstructed by isotropic and anisotropic TV that indicate the position and shape of the samples precisely. Even if detectability works only for limited depth, it validated the potential application of planar MIT system for subsurface imaging. And also, the experimental results verify that isotropic and anisotropic TV algorithm can produce higher quality reconstructed images compared to Tikhonov regularization. All the results of improved depth detection shown in this study opens up further new applications for planar array MIT in landmine detection.

Chapter 7 further expands the MIT applications in imaging tomography for plastic landmine detection. All the investigations are conducted only by simulation works of MIT system.

Theoretically, MIT and ECT itself are incapable of detecting the plastic landmines were planted in ground whose conductivity are non-negligible, ECT requires the assistance provided by planar MIT. Even simulation results presented in this chapter indicates the feasibility of MIT system for landmine detection, further classification experimental research should be conducted in both MIT and ECT to validate this finding.

8.2 Future work

This thesis clarified the fundamental principles of MIT, the existing software image reconstruction algorithms and also presented the achieved approaches of MIT system for proposed specific problems. Based on those findings as well as the limitations, many potential future researches could be launched.

8.2.1 MIT system hardware development

All the experimental work displayed in this dissertation were conducted in the existing MIT system: high conductivity MIT system and low conductivity MIT system. Even the systems are working well for proposed researched now, updated system has to be invented to decrease the reconstructing time or increase the stability of MIT system. Besides, the geometry of the sensor array used in this thesis are circular and planar sensor array only, analyzing the effect of a variation number of coil configurations through sequence, size and position should be an interesting and valuable subject.

8.2.2 Non-linear inverse problem

All the modeling works described in this thesis are assumed to be linear problem and all the reconstructed images accomplished are comparative images. However, the MIT inverse problem in real-life is not linear based. A non-linear inverse solver needs to be implemented to obtain absolute conductivity value and actual images.

8.2.3 Improve the image resolution or quality

As it has been mentioned in objectives of this dissertation, improving image resolution and quality can be achieved through analyzing algorithms used in inverse problem and modifying forward problem. Apparently, the accuracy of the MIT model can be explored by comparing simulation signals and the experimental results, which shown in validation of forward problem in Chapter 3.4. The results accomplished by simulation and experiment are not perfect match, which indicates that the forward model implemented is not perfect. Further investigation on MIT forward model are needed to accomplish the sensitivity map precisely and correctly.

8.2.4 MIT and ECT complex system

ECT itself is capable for detecting the plastic landmines buried in non-conductive or negligibly low conductivity ground while MIT itself is unable to work efficiently for detecting the plastic landmines in conductive ground because of the low conductivity contrast. In real life the plastic landmines were planted in ground whose conductivity are non-negligible, ECT requires the assistance provided by planar MIT. In this research thesis, even the conductivity distribution of plastic landmine in low conductive ground can be acquired by MIT simulation work, the procedure of feeding the conductivity information to ECT system are not implemented. Further investigation on sequential dual-system of MIT and ECT could be conducted through the following two aspects:

- Modifying Jacobian matrix of ECT in dual-system

A more accurate Jacobian matrix or sensitivity map of ECT system can be achieved by considering conductivity distribution information supplied by MIT system.

- Updating reference or background measurement of ECT in dual-system

Normally, the conductive material will induce an impact on electrical capacitance

measurement. So, updating reference measurement of ECT by priori information provided by MIT system will increase the accuracy of this dual-system.

8.2.5 Plastic landmine detection using experimental data

Plastic landmine detection investigated in chapter 8 are during the simulation stage, further experimental researches might be worth investigating in a propose sequential MIT-ECT dual system.

APPENDIX A OTHER REGULARIZATION ALGORITHMS FOR MIT INVERSE PROBLEM

A.1 Non-iterative algorithms

A.1.1 Linear back-projection (LBP)

In a linearized MIT inverse model [44],

$$J\Delta\sigma = \Delta v \tag{A.1}$$

Where J is the Jacobian or sensitivity matrix ($J \in R^{m\times n}$), $\Delta\sigma$ and Δv are complex vectors, $\Delta\sigma$ is the conductivity change distribution ($\Delta\sigma \in R^n$) and Δv is the time difference measurement of induced voltage ($\Delta v \in R^m$).

If J is considered as a linear mapping from the conductivity vector space to the mutual inductance vector space, J^T can be considered to be a related mapping from the mutual inductance vector space to the conductivity vector space, which can give an approximated solution.

$$\widehat{\Delta\sigma} = J^T\Delta v \tag{A.2}$$

A standardized form of equation A.2 can be expressed as following, and it is only an approximate solution.

$$\widehat{\Delta\sigma} = \frac{J^T\Delta v}{J^T u} \qquad u = [1,1,\dots,1] \tag{A.3}$$

Where u is an identity vector. The division of two vectors means each numerator component been divided by the corresponding denominator component [92].

If the conductivity of the test material changed, the normalized change in mutual inductance must be u and the corresponding change in conductivity is $J^T u$. Assuming the normalized measured mutual inductance is Δv, equation A.3 gives the corresponding change in conductivity. Even though LBP produces poor-quality images and can only indicate quantitative information, it is still commonly used since its simplicity. There are other reconstruction algorithms been used to obtain improved image.

A.1.2 Singular value decomposition (SVD)

The singular value decomposition is the generalization to non-square matrices of orthogonal diagonalization of symmetric matrices. SVD provides a means to obtain the solution of equation A.1.

For a matrix $J \in C^{m \times n}$ and J can be decomposed as

$$J = U\Sigma V^T = \sum_{i=1}^{n} u_i \delta_i {v_i}^T \tag{A.4}$$

Where U is a $m \times m$ orthogonal matrix and V is a $n \times n$ orthogonal matrix.

$$U = [u_1, u_2, u_3 \ldots., u_m]$$

$$V = [v_1, v_2, v_3 \ldots., v_n]$$

$$\Sigma = diag[\delta_1, \delta_2, \delta_3 \ldots., \delta_{n-1}, \delta_n] \tag{A.5}$$

Σ is an $m \times n$ matrix with all components zero except the diagonal components $\delta_1, \delta_2, \delta_3 \ldots., \delta_{n-1}, \delta_n$ are singular values of J and note that $\delta_1 > \delta_2 > \delta_3 \ldots. > \delta_{n-1} > \delta_n > 0$.

The solution of equation A.1 can now be written as

$$\Delta\sigma = V\Sigma^{-1}U^T\Delta v = \sum_{i=1}^{n} \frac{v_i}{\delta_i} {u_i}^T \Delta v \tag{A.6}$$

And Σ^{-1} is given by

$$\Sigma^{-1} = diag\left[\frac{1}{\delta_1}, \frac{1}{\delta_2}, \frac{1}{\delta_3} \ldots, \frac{1}{\delta_{n-1}}, \frac{1}{\delta_n}\right] \tag{A.7}$$

Compared to Tikhonov regularization, SVD avoid the calculation of $J^T J$, which means for large matrices it decreases the time costing and reduce the demand of computational resources. But noting that the diagonal components $\delta_1, \delta_2, \delta_3 \ldots, \delta_{n-1}, \delta_n$ are in decreasing order, which means δ_n will be really small and $\frac{1}{\delta_n}$ will be pretty large that will increase the demand of computational resources [93]. So, some methods should be taken to suppress those small singular values, which is introduced in following named truncated singular values decomposition.

A.1.3 Truncated singular value decomposition (TSVD)

Truncated singular value decomposition (TSVD) can be used to explicitly remove those smaller singular values [94] . And TSVD is introduced to solve an ill-posed problem by ignoring $n - r$ number of small singular values, where the rank of J is r, and then the equation A.6 can be converted to as following

$$\Delta\sigma = \sum_{i=1}^{r} \frac{v_i}{\delta_i} {u_i}^T \Delta v \tag{A.8}$$

In most cases, $m < n$ and the rank of J is equal to m ($r = m$).

Where V changed to a $n \times m$ matrix, J changed to a $m \times m$ matrix.

A.2 Iterative algorithms

A.2.1 Landweber's method

Landweber's method is a variation of the steepest gradient descent method. To minimize $\|J\Delta\sigma - \Delta v\|^2$, we should find $\Delta\sigma$ to make the following function minimal [95, 96].

$$f(\Delta\sigma) = (J\Delta\sigma - \Delta v)^T(J\Delta\sigma - \Delta v) = \Delta\sigma^T J^T J\Delta\sigma - 2(J\Delta\sigma)^T\Delta v + \Delta v^T\Delta v \quad (A.9)$$

The gradient of $f(\Delta\sigma)$ can be calculated as

$$\nabla f(\Delta\sigma) = J^T J\Delta\sigma - J^T\Delta v = J^T(J\Delta\sigma - \Delta v) \quad (A.10)$$

The steepest gradient descent method is choosing the direction that makes $f(\Delta\sigma)$ decreases most quickly for the next iteration. The iteration procedure is therefore

$$\Delta\sigma_{n+1} = \Delta\sigma_n - \tau\nabla f(\Delta\sigma_n) = \Delta\sigma_n - \tau J^T(J\Delta\sigma_n - \Delta v) \quad (A.11)$$

Where n is the number of iterations; $\Delta\sigma_n$ is the reconstructed conductivity in the n-th iteration; τ is the relaxation parameter and should be positive.

We can analyze convergence by assuming the system as linear difference equation and then

$$\Delta\sigma_{n+1} = (I - \tau J^T J)\Delta\sigma_n + \tau J^T\Delta v \quad (A.12)$$

$$\Delta\sigma_{n+1} = B\Delta\sigma_n + C\Delta v \quad (A.13)$$

Where $B = (I - \tau J^T J)$ and $C = \tau J^T\Delta v$

$$\Delta\sigma_{n+1} = B^n\Delta\sigma_0 + (I - B^n)(I - B)^{-1}C \quad (A.14)$$

$$\Delta\sigma_{n+1} = (I - \tau J^T J)^n\Delta\sigma_0 + (I - (I - \tau J^T J)^n)(J^T J)^{-1}J^T\Delta v \quad (A.15)$$

Besides, we see that $\|I - \tau J^T J\| < 1$ is the condition for convergence, so the necessary condition for convergence of the Landweber scheme:

$$0 < \tau < \frac{2}{\|J^T J\|_2} \tag{A.16}$$

So, the relaxation parameter τ should be selected to satisfy the convergence condition.

Landweber algorithm is generally used in a linear matrix system. One advantage of this method is during the iteration process, not only is the cost function minimized, but also the condition of inverse problem is regularized since a greater number of iterations can build a smoother solution [97]. Besides, this method could avoid $J^T J$ multiplication, which means it will reduce the demand of computational resources, especially in case of a large Jacobian matrix. But drawback of Landweber method is that it is difficult to choose the optimal number of iterations.

A.2.2 More general regularization

The following method, named maximum a-posterior estimate (MAP), mainly used when the inverse problem is casted into a probabilistic or statistical framework. And it will be presented by introducing the Bayes theorem, semi-norms and a little probability theory.

- **Bayes theorem**

Bayes theorem [42] is relative to the probability density functions of random variables. The probability of a random variable x with the given value of b is

$$P(x|b) = \frac{P(b|x)P(x)}{P(b)} \tag{A.17}$$

Where $P(b|x)$ is the probability of b with the given x, $P(x)$ and $P(b)$ are the probability density functions of random variable x and b.

- **Semi-norms**

The Tikhonov regularization using the standard 2-norm has been introduced in Chapter 4.2.

The term $\|x\|$ does not enforce smoothness even though it deletes the extreme values[42]. Actually, there are some more interesting norms can be used such as semi-norm. The following is the definition of semi-norm.

A real-valued function $p\,(x)$ on a linear space X can be defined as a semi-norm on X if these three conditions are satisfied[98] [99]:

$$p\,(x+y) \leq p(x) + p(y)\ \ (triangle\ equality) \tag{A.18}$$

$$p(\alpha x) = |\alpha| p(x) \tag{A.19}$$

$$p(x) \geq 0\ \ (non-negative) \tag{A.20}$$

Besides, the function $\|x\|$ is a norm if it satisfies the additional condition: $\|x\| \geq 0\ and\ \|x\| = 0 \Leftrightarrow x = 0$

We can select a positive matrix $P \in C^{n\times n}$ (loose no generality, Hermitian) and the norm $\|x\|_P^2 = x^T P x$. Such matrices all have the square operator L and $P = L^T L$, then it can be obtained:

$$\|x\|_P^2 = x^T P x = x^T L^T L x = \|Lx\|^2 \tag{A.21}$$

- **A little probability theory**

Every random variable has a probability density function [42].

Let x be a random variable then P_x is a function, showing the probability of x being between a and b

$$P(a \leq x \leq b) = \int_a^b P_x\ (x)\, dx \tag{A.22}$$

If a variable x with mean μ and variance σ^2 is normally distributed (also called Gaussian distribution), its probability density function (p.d.f) is

$$P(x) = \frac{1}{\sigma\sqrt{2\pi}} e^{-\frac{(x-\mu)^2}{2\sigma^2}} \tag{A.23}$$

And the expected value (mean) of a random variable

$$E\,[X] = \int_{-\infty}^{\infty} x\, P_x(x)\, dx \tag{A.24}$$

$$The\ variance\ \ V\,[X] = \mathrm{E}\,[(\mathrm{X} - E\,[X])^2] = \mathrm{E}\,[X^2] - (E\,[X])^2 \tag{A.25}$$

If the random variable is definite vector, the probability density function is [83]

$$P\,(x) = \frac{1}{(\sigma\sqrt{2\pi})^{\frac{n}{2}}} \prod_{i=1}^{n} e^{-(x_i-\mu_i)^2/2\sigma^2} = \frac{1}{(\sigma\sqrt{2\pi})^{\frac{n}{2}}} e^{-\frac{\|x-\mu\|^2}{2\sigma^2}} \tag{A.26}$$

Generally, if we set the $convariance\ matrix = C$, which is invertible and symmetric as well as P, $P = C^{-1}$ and $|C| = |P|$, $E\,[X] = \mu$, we can obtain

$$P\,(x) = \frac{1}{(2\pi)^{\frac{n}{2}}\sqrt{|C|}} e^{-\frac{1}{2}(x-\mu)^{\mathrm{T}} P (x-\mu)} = \frac{1}{(2\pi)^{\frac{n}{2}}\sqrt{|P|}} e^{-\frac{1}{2}\|x-\mu\|_P^2} \tag{A.27}$$

The linearized inverse problem can be also described by

$$Ax = b + e \tag{A.28}$$

Where e is the error in the system (the difference between the real solution and computable solution, $e = b - Ax$. Then we can make some assumptions:

$$E\,[e] = 0, so\ E\,[b + e] = b \tag{A.29}$$

$$Cov\,[b] = Cov\,[e] \tag{A.30}$$

$$Cov\,[e]^{-1} = Q \tag{A.31}$$

$and\ Q\ has\ square\ root\ Q^{1/2}$, besides, Q is a diagonal matrix [100,101].

So that e has mean zero and $Cov\,[e] = Q^{-1}$ and from equation A.27, we can obtain

$$P_{\,e}(e|x) = \frac{1}{(2\pi)^{\frac{m}{2}}\sqrt{|Q|}} e^{-\frac{1}{2}\|e\|_Q^2} \tag{A.32}$$

It can be known from equation A.28 that $P_{\,b}(b|x) = P_{\,e}(Ax - b|x)$

$$So\;\; P_{\,b}(b|x) = \frac{1}{(2\pi)^{\frac{m}{2}}\sqrt{|Q|}} e^{-\frac{1}{2}\|Ax - b\|_Q^2} \tag{A.33}$$

Then it is more convenient to get the p.d.f of x by assuming x has mean x_0 and $Cov\,[x] = P^{-1}$.

$$Similarly\; P\,(x) = \frac{1}{(2\pi)^{\frac{n}{2}}\sqrt{|P|}} e^{-\frac{1}{2}\|x - x_0\|_P^2} \tag{A.34}$$

When we go back to Bayes theorem, it can be obtained that

$$P(x|b) = \frac{e^{-\frac{1}{2}[\|x-x_0\|_P^2 + \|Ax-b\|_Q^2]}}{(2\pi)^{(n+m)/2}\sqrt{|P||Q|}P(b)} \tag{A.35}$$

- **Maximum A-Posterior estimate (MAP)**

After obtaining the probability density function of x with given b, the next step is to get the most likely x, which means to maximize the posterior $P(x|b)$. This is so called maximum a-posteriori (MAP) estimate. According to equation A.35 $P(x|b)$ can be maximized by minimizing $\|x - x_0\|_P^2 + \|Ax - b\|_Q^2$. Therefore, the problem can be stated as

$$\hat{x} = argmin\|x - x_0\|_P^2 + \|Ax - b\|_Q^2 \tag{A.36}$$

The method of solving equation A.36 is same to solving equation 4.5 in Chapter 4.2.

The function to be minimized can be expanded as following.

$$\hat{x} = argmin_x\,[(Ax - b)^{\mathrm{T}} Q(Ax - b) + (x - x_0)^{\mathrm{T}} P(x - x_0)] \tag{A.37}$$

To get the solution of equation A.37, we should make its differential equal to zero. According to the differential rule, we can obtain

$$2(Ax-b)^{\mathrm{T}}Q\frac{\partial}{\partial x}(Ax-b)+2(x-x_0)^{\mathrm{T}}P$$

$$=2(Ax-b)^{\mathrm{T}}QA+2(x-x_0)^{\mathrm{T}}P$$

$$=2x^TA^TQA-2b^TQA+2x^TP-2{x_0}^TP=0 \quad (A.38)$$

By transposing both sides of the equation A.38 and simplified, we get

$$A^TQ^TAx-A^TQ^Tb+P^Tx-P^Tx_0=0$$

$$(A^TQ^TA+P^T)x=P^Tx_0+A^TQ^Tb \quad (A.39)$$

Then we can find the solution for the minimum

$$x=(A^TQ^TA+P^T)^{-1}(P^Tx_0+A^TQ^Tb) \quad (A.40)$$

Besides, it has been mentioned before that we choose Q to be diagonal matrix and P is symmetric matrix, which means $Q^T=Q$ and $P^T=P$, then we can get

$$x=(A^TQA+P)^{-1}(Px_0+A^TQb) \quad (A.41)$$

A.3 Advantages and disadvantages

The following Table A.1 indicates the advantages and disadvantages of part of algorithms.

APPENDIX A

Table A.1 The advantages and disadvantages of inverse problem algorithms

Types		Advantages	Disadvantages
Non- Iterative method	LBP	Simplicity	Produce poor-quality images
	Tikhnov regularization	Increase image quality (more information can be obtained)	Hard to choose the optimal regularization parameter, show blurred edges and boundaries between materials
	SVD	Avoid the calculation of $J^T J$ and decrease the time costing	Increase the demand of computational resources
	TSVD	Remove those smaller singular values	Increase the demand of computational resources
Iterative method	Total variation	Produce almost optimal reconstructed images; displace sharp edges and boundaries between materials	Need tuning the parameter; increase the reconstruction time
	Landweber's method	Avoid multiplication of $J^T J$, reduce the demand of computational resources	Difficult to choose the optimal number of iterations

REFERENCES

[1] H.-Y. Wei, "Magnetic Induction Tomography for Medical and Industrial Imaging : Hardware and Software Development," Doctor of Philosophy, Electric & Electrical Engineering, University of Bath, 2012.

[2] H. Griffiths, "Magnetic induction tomography," *Measurement science and technology,* vol. 12, no. 8, p. 1126, 2001.

[3] A. Korjenevsky, V. Cherepenin, and S. Sapetsky, "Magnetic induction tomography: experimental realization," *Physiological measurement,* vol. 21, no. 1, p. 89, 2000.

[4] D. S. Holder, *Electrical impedance tomography: methods, history and applications*. CRC Press, 2004.

[5] M. Soleimani, "Image and shape reconstruction methods in magnetic induction tomography and electrical impedance tomography," Doctor of Philosophy, Electronic & Electrical Engineering, University of Manchester, 2005.

[6] M. Zhang, L. Ma, and M. Soleimani, "Magnetic induction tomography guided electrical capacitance tomography imaging with grounded conductors," *Measurement,* vol. 53, pp. 171-181, 2014.

[7] H.-Y. Wei and M. Soleimani, "A magnetic induction tomography system for prospective industrial processing applications," *Chinese Journal of Chemical Engineering,* vol. 20, no. 2, pp. 406-410, 2012.

[8] G. S. Park and D. S. Kim, "Development of a magnetic inductance tomography system," *IEEE transactions on magnetics,* vol. 41, no. 5, pp. 1932-1935, 2005.

[9] A. Borges, J. De Oliveira, J. Velez, C. Tavares, F. Linhares, and A. Peyton, "Development of electromagnetic tomography (EMT) for industrial applications. Part 2: Image reconstruction and software framework," in *Proc. 1st World Congr. Industrial Process Tomography*, 1999, pp. 219-225.

[10] X. Ma, A. J. Peyton, R. Binns, and S. R. Higson, "Electromagnetic techniques for imaging the cross-section distribution of molten steel flow in the continuous casting nozzle," *IEEE Sensors Journal,* vol. 5, no. 2, pp. 224-232, 2005.

[11] B. J. Darrer, J. C. Watson, P. Bartlett, and F. Renzoni, "Magnetic imaging: a new tool for UK national nuclear security," *Scientific reports,* vol. 5, p. 7944, 2015.

[12] P. C. Bhope and A. S. Bhalchandra, "Various Landmine Detection Techniques: A Review," *International Journal of Innovative Research in Science, Engineering and Technology,* vol. 4, 2015.

[13] D. Goss, R. Mackin, E. Crescenzo, H. Tapp, and A. Peyton, "Development of electromagnetic inductance tomography (EMT) hardware for determining human body composition," 2003.

[14] L. Ma, "Magnetic Induction Tomography for Non-Destructive Evaluation and Process Tomography," Doctor of Philosophy, Electronic & Electrical

Engineering, University of Bath, 2014.

[15] H.-Y. Wei and M. Soleimani, "Hardware and software design for a National Instrument-based magnetic induction tomography system for prospective biomedical applications," *Physiological Measurement,* vol. 33, no. 5, p. 863, 2012.

[16] W. Yang, "Design of electrical capacitance tomography sensors," *Measurement Science and Technology,* vol. 21, no. 4, p. 042001, 2010.

[17] R. Binns, A. R. Lyons, A. Peyton, and W. Pritchard, "Imaging molten steel flow profiles," *Measurement Science and Technology,* vol. 12, no. 8, p. 1132, 2001.

[18] S. Watson, C. Igney, O. Dössel, R. Williams, and H. Griffiths, "A comparison of sensors for minimizing the primary signal in planar-array magnetic induction tomography," *Physiological measurement,* vol. 26, no. 2, p. S319, 2005.

[19] J. Rosell-Ferrer, R. Merwa, P. Brunner, and H. Scharfetter, "A multifrequency magnetic induction tomography system using planar gradiometers: data collection and calibration," *Physiological Measurement,* vol. 27, no. 5, p. S271, 2006.

[20] A. Peyton *et al.*, "An overview of electromagnetic inductance tomography: description of three different systems," *Measurement Science and Technology,* vol. 7, no. 3, p. 261, 1996.

[21] H.-Y. Wei and A. J. Wilkinson, "Design of a sensor coil and measurement electronics for magnetic induction tomography," *IEEE Transactions on Instrumentation and Measurement,* vol. 60, no. 12, pp. 3853-3859, 2011.

[22] S. Ramli and A. Peyton, "Feasibility study of planar-array electromagnetic inductance tomography (EMT)," in *1st World Congress on Industrial Process Tomography*, 1999, pp. 14-17.

[23] J. M. Caeiros and R. C. Martins, "An optimized forward problem solver for the complete characterization of the electromagnetic properties of biological tissues in magnetic induction tomography," *IEEE Transactions on Magnetics,* vol. 48, no. 12, pp. 4707-4712, 2012.

[24] D. J. Griffiths and M. A. Heald, "Time‐dependent generalizations of the Biot‐Savart and Coulomb laws," *American Journal of Physics,* vol. 59, no. 2, pp. 111-117, 1991.

[25] N. A. Spaldin, *Magnetic materials: fundamentals and applications*. Cambridge University Press, 2010.

[26] O. Biro and K. Preis, "An edge finite element eddy current formulation using a reduced magnetic and a current vector potential," *IEEE Transactions on Magnetics,* vol. 36, no. 5, pp. 3128-3130, 2000.

[27] Y. Li and M. Soleimani, "Imaging conductive materials with high frequency electrical capacitance tomography," *Measurement,* vol. 46, no. 9, pp. 3355-3361, 2013.

[28] J. Coveney, M. Pham, A. Kyllo, and N. Gray, "Comparison of modelling approaches for the eddy current problem as applied to the geometry of a taphole," *Measurement Science and Technology,* vol. 17, no. 2, p. 340, 2006.

[29] R. D. Cook, *Concepts and applications of finite element analysis*. John Wiley

& Sons, 2007.

[30] M. Soleimani, "Computational aspects of low frequency electrical and electromagnetic tomography: A review study," *Int. J. Numer. Anal. Model,* vol. 5, no. 3, pp. 407-440, 2008.

[31] G. F. Carey, J. T. Oden, and E. B. Becker, *Finite elements. 1. An introduction*. Prentice-Hall, 1981.

[32] R. Wang and N. Demerdash, "On the effects of grid ill-conditioning in three dimensional finite element vector potential magnetostatic field computations," *IEEE Transactions on Magnetics,* vol. 26, no. 5, pp. 2190-2192, 1990.

[33] M. H. Pham, Y. Hua, and N. B. Gray, "Eddy current tomography for metal solidification imaging," in *1st World Congress on Industrial Process Tomography, Buxton*, 1999, pp. 451-458.

[34] D. J. Sadler and C. H. Ahn, "On-chip eddy current sensor for proximity sensing and crack detection," *Sensors and Actuators A: Physical,* vol. 91, no. 3, pp. 340-345, 2001.

[35] O. Biro and K. Preis, "On the use of the magnetic vector potential in the finite-element analysis of three-dimensional eddy currents," *IEEE Transactions on magnetics,* vol. 25, no. 4, pp. 3145-3159, 1989.

[36] R. Merwa, K. Hollaus, B. Brandstätter, and H. Scharfetter, "Numerical solution of the general 3D eddy current problem for magnetic induction tomography (spectroscopy)," *Physiological measurement,* vol. 24, no. 2, p. 545, 2003.

[37] O. Bíró, "Edge element formulations of eddy current problems," *Computer methods in applied mechanics and engineering,* vol. 169, no. 3-4, pp. 391-405, 1999.

[38] M. Soleimani, W. R. Lionheart, A. J. Peyton, X. Ma, and S. R. Higson, "A three-dimensional inverse finite-element method applied to experimental eddy-current imaging data," *IEEE Transactions on Magnetics,* vol. 42, no. 5, pp. 1560-1567, 2006.

[39] M. N. Tek and N. G. Gençer, "A new 3D FEM formulation for the solution of potential fields in magnetic induction problems," in *Engineering in Medicine and Biology Society, 1997. Proceedings of the 19th Annual International Conference of the IEEE*, 1997, vol. 6, pp. 2470-2473: IEEE.

[40] M. Vauhkonen, M. Hamsch, and C. Igney, "A measurement system and image reconstruction in magnetic induction tomography," *Physiological measurement,* vol. 29, no. 6, p. S445, 2008.

[41] R. Merwa, P. Brunner, A. Missner, K. Hollaus, and H. Scharfetter, "Solution of the inverse problem of magnetic induction tomography (MIT) with multiple objects: analysis of detectability and statistical properties with respect to the reconstructed conducting region," *Physiological measurement,* vol. 27, no. 5, p. S249, 2006.

[42] J. P. Kaipio, V. Kolehmainen, E. Somersalo, and M. Vauhkonen, "Statistical inversion and Monte Carlo sampling methods in electrical impedance tomography," *Inverse problems,* vol. 16, no. 5, p. 1487, 2000.

[43] C. R. Vogel, *Computational methods for inverse problems*. SIAM, 2002.

[44] H.-Y. Wei and M. Soleimani, "Three-dimensional magnetic induction tomography imaging using a matrix free Krylov subspace inversion algorithm," *Progress In Electromagnetics Research,* vol. 122, pp. 29-45, 2012.

[45] D. Isaacson and M. Cheney, "Current problems in impedance imaging," *Inverse problems in partial differential equations,* pp. 141-149, 1990.

[46] A. P. Calderón, "On an inverse boundary value problem," *Computational & Applied Mathematics,* vol. 25, no. 2-3, pp. 133-138, 2006.

[47] R. Merwa, K. Hollaus, P. Brunner, and H. Scharfetter, "Solution of the inverse problem of magnetic induction tomography (MIT)," *Physiological Measurement,* vol. 26, no. 2, p. S241, 2005.

[48] K. Atkinson and W. Han, *Theoretical numerical analysis* (Chapter1). Springer, 2005.

[49] K. Yosida, "Functional analysis. Reprint of the sixth (1980) edition. Classics in Mathematics," *Springer-Verlag, Berlin,* vol. 11, p. 14, 1995.

[50] M. Cheney, D. Isaacson, and E. L. Isaacson, "Exact solutions to a linearized inverse boundary value problem," *Inverse Problems,* vol. 6, no. 6, p. 923, 1990.

[51] L. Ma, A. Hunt, and M. Soleimani, "Experimental evaluation of conductive flow imaging using magnetic induction tomography," *International Journal of Multiphase Flow,* vol. 72, pp. 198-209, 2015.

[52] T. Goldstein and S. Osher, "The split Bregman method for L1-regularized problems," *SIAM journal on imaging sciences,* vol. 2, no. 2, pp. 323-343, 2009.

[53] S. Osher, M. Burger, D. Goldfarb, J. Xu, and W. Yin, "An iterative regularization method for total variation-based image restoration," *Multiscale Modeling & Simulation,* vol. 4, no. 2, pp. 460-489, 2005.

[54] W. Yin, G. Chen, L. Chen, and B. Wang, "The design of a digital magnetic induction tomography (MIT) system for metallic object imaging based on half cycle demodulation," *IEEE Sensors Journal,* vol. 11, no. 10, pp. 2233-2240, 2011.

[55] J. J. Abascal *et al.*, "Fluorescence diffuse optical tomography using the split Bregman method," *Medical physics,* vol. 38, no. 11, pp. 6275-6284, 2011.

[56] Y. Li, R. Liu, and X. Dong, "A Magnetic Induction Tomography System Using Fully Synchronous Phase Detection," in *Bioinformatics and Biomedical Engineering, 2009. ICBBE 2009. 3rd International Conference on*, 2009, pp. 1-4: IEEE.

[57] D. Dyck, D. Lowther, and E. Freeman, "A method of computing the sensitivity of electromagnetic quantities to changes in materials and sources," *IEEE Transactions on Magnetics,* vol. 30, no. 5, pp. 3415-3418, 1994.

[58] F. Li, "Condition monitoring in power cables using an integrated inductive capacitive sensing imaging method," MSc, Electronic & Electrical Engineering, University of Bath, 2014.

[59] S. Puwal and B. J. Roth, "Fourier analysis in magnetic induction tomography: Mapping of anisotropic, inhomogeneous resistivity," *Measurement Science and Technology,* vol. 22, no. 8, p. 085802, 2011.

[60] M. Burger and S. Osher, "A guide to the TV zoo," in *Level Set and PDE Based*

Reconstruction Methods in Imaging: Springer, 2013, pp. 1-70.

[61] A. Sawatzky, C. Brune, T. Kösters, F. Wuebbeling, and M. Burger, "EM-TV methods for inverse problems with Poisson noise," in *Level set and PDE based reconstruction methods in imaging*: Springer, 2013, pp. 71-142.

[62] J. Wang, J. Ma, B. Han, and Q. Li, "Split Bregman iterative algorithm for sparse reconstruction of electrical impedance tomography," *Signal Processing,* vol. 92, no. 12, pp. 2952-2961, 2012.

[63] A. Adler *et al.*, "GREIT: a unified approach to 2D linear EIT reconstruction of lung images," *Physiological measurement,* vol. 30, no. 6, p. S35, 2009.

[64] M. Burger, A. C. Mennucci, S. Osher, and M. Rumpf, *Level Set and PDE Based Reconstruction Methods in Imaging: Cetraro, Italy 2008, Editors: Martin Burger, Stanley Osher*. Springer, 2013.

[65] J. F. Abascal, M. Abella, E. Marinetto, J. Pascau, and M. Desco, "A Novel Prior- and Motion-Based Compressed Sensing Method for Small-Animal Respiratory Gated CT," *PloS one,* vol. 11, no. 3, p. e0149841, 2016.

[66] F. Li, J. F. Abascal, M. Desco, and M. Soleimani, "Total variation regularization with split Bregman-based method in magnetic induction tomography using experimental data," *IEEE Sensors Journal,* vol. 17, no. 4, pp. 976-985, 2017.

[67] L. I. Rudin, S. Osher, and E. Fatemi, "Nonlinear total variation based noise removal algorithms," *Physica D: Nonlinear Phenomena,* vol. 60, no. 1-4, pp. 259-268, 1992.

[68] Z. Chen, X. Jin, L. Li, and G. Wang, "A limited-angle CT reconstruction method based on anisotropic TV minimization," *Physics in medicine and biology,* vol. 58, no. 7, p. 2119, 2013.

[69] M. Werlberger, W. Trobin, T. Pock, A. Wedel, D. Cremers, and H. Bischof, "Anisotropic Huber-L1 Optical Flow," in *BMVC*, 2009, vol. 1, no. 2, p. 3.

[70] Z. Chen, X. Jin, L. Li, and G. Wang, "A limited-angle CT reconstruction method based on anisotropic TV minimization," *Physics in Medicine & Biology,* vol. 58, no. 7, p. 2119, 2013.

[71] T. Correia *et al.*, "Split operator method for fluorescence diffuse optical tomography using anisotropic diffusion regularisation with prior anatomical information," *Biomedical optics express,* vol. 2, no. 9, pp. 2632-2648, 2011.

[72] S. Esedoḡlu and S. J. Osher, "Decomposition of images by the anisotropic Rudin ‐ Osher ‐ Fatemi model," *Communications on pure and applied mathematics,* vol. 57, no. 12, pp. 1609-1626, 2004.

[73] Y. Lou, T. Zeng, S. Osher, and J. Xin, "A weighted difference of anisotropic and isotropic total variation model for image processing," *SIAM Journal on Imaging Sciences,* vol. 8, no. 3, pp. 1798-1823, 2015.

[74] N. Goldfine, "Near surface material property profiling for determination of SCC susceptibility," in *4th EPRI Balance-of-Plant Heat Exchanger NDE Symposium, WY, June 10-12, 1996*, 1996.

[75] S. Mukhopadhyay, S. Yamada, and M. Iwahara, "Inspection of electroplated materials--performance comparison with planar meander and mesh type magnetic sensor," *International Journal of Applied Electromagnetics and*

Mechanics, vol. 15, no. 1-4, pp. 323-329, 2001.

[76] W. Yin and A. Peyton, "A planar EMT system for the detection of faults on thin metallic plates," *Measurement Science and Technology,* vol. 17, no. 8, p. 2130, 2006.

[77] L. Ma, H.-Y. Wei, and M. Soleimani, "Planar magnetic induction tomography for 3D near subsurface imaging," *Progress In Electromagnetics Research,* vol. 138, pp. 65-82, 2013.

[78] C. Gooneratne, S. Mukhopahyay, and G. S. Gupta, "A review of sensing technologies for landmine detection: Unmanned vehicle based approach," in *2nd International Conference on Autonomous Robots and Agents*, 2004, pp. 401-407.

[79] P. M. Church, P. M. Wort, S. Gagnon, and J. E. McFee, "Performance assessment of an electrical impedance tomography detector for minelike objects," in *Aerospace/Defense Sensing, Simulation, and Controls*, 2001, pp. 120-131: International Society for Optics and Photonics.

[80] S. Huang, R. Green, A. Plaskowski, and M. Beck, "Conductivity effects on capacitance measurements of two-component fluids using the charge transfer method," *Journal of Physics E: Scientific Instruments,* vol. 21, no. 6, p. 539, 1988.

[81] A. Stott, R. Green, and K. Seraji, "Comparison of the use of internal and external electrodes for the measurement of the capacitance and conductance of fluids in pipes," *Journal of Physics E: Scientific Instruments,* vol. 18, no. 7, p. 587, 1985.

[82] C. Xie *et al.*, "Electrical capacitance tomography for flow imaging: system model for development of image reconstruction algorithms and design of primary sensors," *IEE Proceedings G (Circuits, Devices and Systems),* vol. 139, no. 1, pp. 89-98, 1992.

[83] M. Soleimani and W. R. Lionheart, "Nonlinear image reconstruction for electrical capacitance tomography using experimental data," *Measurement Science and Technology,* vol. 16, no. 10, p. 1987, 2005.

[84] W. Yang, "Calibration of capacitance tomography systems: a new method for setting system measurement range," *Measurement Science and Technology,* vol. 7, no. 6, p. L863, 1996.

[85] M. Zhang, L. Ma, and M. Soleimani, "Dual modality ECT–MIT multi-phase flow imaging," *Flow Measurement and Instrumentation,* vol. 46, pp. 240-254, 2015.

[86] R. Banasiak, R. Wajman, and M. Soleimani, "An efficient nodal Jacobian method for 3D electrical capacitance tomography image reconstruction," *Insight-Non-Destructive Testing and Condition Monitoring,* vol. 51, no. 1, pp. 36-38, 2009.

[87] A. Korjenevsky, V. Cherepenin, and S. Sapetsky, "Magnetic induction tomography-new imaging method in biomedicine," *Proc. 2nd World Congr. Industrial Process Tomography (Hannover),* pp. 240-246, 2001.

[88] H. Scharfetter, R. Merwa, and K. Pilz, "A new type of gradiometer for the receiving circuit of magnetic induction tomography (MIT)," *Physiological*

measurement, vol. 26, no. 2, p. S307, 2005.

[89] H. Griffiths, W. Gough, S. Watson, and R. Williams, "Residual capacitive coupling and the measurement of permittivity in magnetic induction tomography," *Physiological Measurement,* vol. 28, no. 7, p. S301, 2007.

[90] R. D. Grisso, M. M. Alley, D. L. Holshouser, and W. E. Thomason, "Precision Farming Tools. Soil Electrical Conductivity," 2005.

[91] M. Zhang and M. Soleimani, "Simultaneous reconstruction of permittivity and conductivity using multi-frequency admittance measurement in electrical capacitance tomography," *Measurement Science and Technology,* vol. 27, no. 2, p. 025405, 2016.

[92] P. C. Hansen, *Rank-deficient and discrete ill-posed problems: numerical aspects of linear inversion*. SIAM, 1998.

[93] A. Kameari, "Regularization on ill-posed source terms in FEM computation using two magnetic vector potentials," *IEEE transactions on magnetics,* vol. 40, no. 2, pp. 1310-1313, 2004.

[94] R. Blue, "A real-time three-dimensional linearized reconstruction algorithm generalized for multiple planes of electrodes," *Rensselaer Polytechnic Institute Ph. D. Thesis,* 1997.

[95] W. Yang, D. Spink, T. York, and H. McCann, "An image-reconstruction algorithm based on Landweber's iteration method for electrical-capacitance tomography," *Measurement Science and Technology,* vol. 10, no. 11, p. 1065, 1999.

[96] M. Ziolkowski, S. Gratkowski, and R. Palka, "Solution of three dimensional inverse problem of magnetic induction tomography using Tikhonov regularization method," *International Journal of Applied Electromagnetics and Mechanics,* vol. 30, no. 3, 4, pp. 245-253, 2009.

[97] M. Soleimani, W. Lionheart, A. Peyton, and X. Ma, "A 3D inverse finite element technique applied to experimental magnetic induction tomography data," in *4th World Congress on Industrial Process Tomography*, 2005.

[98] J. Kaipio, A. Seppänen, E. Somersalo, and H. Haario, "Posterior covariance related optimal current patterns in electrical impedance tomography," *Inverse Problems,* vol. 20, no. 3, p. 919, 2004.

[99] S. Liu, L. Fu, and W. Yang, "Optimization of an iterative image reconstruction algorithm for electrical capacitance tomography," *Measurement Science and Technology,* vol. 10, no. 7, p. L37, 1999.

[100] W. Yang and L. Peng, "Image reconstruction algorithms for electrical capacitance tomography," *Measurement science and technology,* vol. 14, no. 1, p. R1, 2002.

[101] M. Cheney, D. Isaacson, J. C. Newell, S. Simske, and J. Goble, "NOSER: An algorithm for solving the inverse conductivity problem," *International Journal of Imaging Systems and Technology,* vol. 2, no. 2, pp. 66-75, 1990.